

The SOFIA Massive (SOMA) Star Formation Survey. V. Clustered Protostars

ZOIE TELKAMP,¹ RUBÉN FEDRIANI,² JONATHAN C. TAN,^{1,3} CHI-YAN LAW,⁴ YICHEN ZHANG,⁵ ADELE PLUNKETT,⁶
SAMUEL CROWE,¹ YAO-LUN YANG,⁷ JAMES M. DE BUIZER,⁸ MARIA T. BELTRAN,⁹ MÉLISSE BONFAND,¹ RYAN BOYDEN,¹
GIULIANA COSENTINO,¹⁰ PRASANTA GORAI,¹¹ MENGYAO LIU,¹ VIVIANA ROSERO,¹² KOTOMI TANIGUCHI,¹³ AND
KEI E. I. TANAKA¹³

¹*Dept. of Astronomy, University of Virginia, Charlottesville, Virginia 22904, USA*

²*Instituto de Astrofísica de Andalucía, CSIC, Glorieta de la Astronomía s/n, E-18008 Granada, Spain*

³*Dept. of Space, Earth & Environment, Chalmers University of Technology, 412 93 Gothenburg, Sweden*

⁴*Osservatorio Astrofisico di Arcetri, Largo Enrico Fermi, 5, 50125 Firenze FI, Italy*

⁵*Department of Astronomy, Shanghai Jiao Tong University, 800 Dongchuan Rd., Minhang, Shanghai 200240, China*

⁶*National Radio Astronomy Observatory, 520 Edgemont Road, Charlottesville, VA 22903, USA*

⁷*Star and Planet Formation Laboratory, RIKEN Cluster for Pioneering Research, Wako, Saitama 351-0198, Japan*

⁸*Carl Sagan Center for Research, SETI Institute, Mountain View, CA, USA*

⁹*INAF-Osservatorio Astrofisico di Arcetri, Largo E. Fermi 5, 50125 Firenze, Italy*

¹⁰*European Southern Observatory, Karl-Schwarzschild-Strasse 2, D-85748 Garching, Germany*

¹¹*Roseland Centre for Solar Physics, Institute of Theoretical Astrophysics, Sem Salands vei 13, 0371 Oslo, Norway*

¹²*Division of Physics, Mathematics, and Astronomy, California Institute of Technology, Pasadena, CA 91125, USA*

¹³*National Astronomical Observatory of Japan, National Institutes of Natural Sciences, 2-21-1 Osawa, Mitaka, Tokyo 181-8588, Japan*

ABSTRACT

We present $\sim 8 - 40 \mu\text{m}$ SOFIA-FORCAST images of seven regions of “clustered” star formation as part of the SOFIA Massive (SOMA) Star Formation Survey. We identify a total of 34 protostar candidates and build their spectral energy distributions (SEDs). We fit these SEDs with a grid of radiative transfer models based on the Turbulent Core Accretion (TCA) theory to derive key protostellar properties, including initial core mass, M_c , clump environment mass surface density, Σ_{cl} , and current protostellar mass, m_* . We also carry out empirical graybody (GB) estimation of Σ_{cl} , which allows a case of restricted SED fitting within the TCA model grid. We also release version 2.0 of the open-source Python package *sedcreator*, designed to automate the aperture photometry and SED building and fitting process for sources in clustered environments, where flux contamination from close neighbors typically complicates the process. Using these updated methods, SED fitting yields values of $M_c \sim 30 - 200 M_\odot$, $\Sigma_{\text{cl,SED}} \sim 0.1 - 3 \text{ g cm}^{-2}$, and $m_* \sim 4 - 50 M_\odot$. The graybody fitting yields smaller values of $\Sigma_{\text{cl,GB}} \lesssim 1 \text{ g cm}^{-2}$. From these results, we do not find evidence for a critical Σ_{cl} needed to form massive ($\gtrsim 8 M_\odot$) stars. However, we do find tentative evidence for a dearth of the most massive ($m_* \gtrsim 30 M_\odot$) protostars in the clustered regions suggesting a potential impact of environment on the stellar initial mass function.

Keywords: ISM: jets and outflows — dust — stars: formation — stars: winds, outflows — stars: early-type — infrared radiation

1. INTRODUCTION

Due to their enormous luminosities, massive stars impact a vast range of scales and processes, from the reionization of the universe, to galaxy evolution, to the formation of star clusters and planets. Despite their importance, no consensus has been reached on the forma-

Corresponding author: Zoie Telkamp
zrt7qc@virginia.edu

Corresponding author: Rubén Fedriani
fedriani@iaa.es

tion mechanisms of massive stars. Theories range from extensions of the standard core accretion model that describes low-mass star formation, e.g., the Turbulent Core Accretion (TCA) model (McKee & Tan 2002, 2003), to competitive accretion models that form massive stars in the centers of crowded protoclusters of low-mass protostars (e.g., Bonnell et al. 1998; Wang et al. 2010; Grudić et al. 2022).

The SOFIA Massive (SOMA) Star Formation Survey (PI: Tan) aims to test theoretical models of massive star formation by characterizing a sample of $\gtrsim 50$ high- and intermediate-mass protostars spanning a range of environments and evolutionary stages. These objects have been observed with the SOFIA-Faint Object infraRed CAmera for the SOFIA Telescope (FORCAST) instrument (Herter et al. 2018) from ~ 10 to $40 \mu\text{m}$. Paper I of the survey (De Buizer et al. 2017) presented the first 8 sources, most of which are massive protostars. Paper II (Liu et al. 2019) presented 7 especially luminous sources, which are some of the most massive protostars in the survey. Paper III (Liu et al. 2020) presented 14 intermediate-mass sources. Paper IV (Fedriani et al. 2023) analyzed 11 sources that are characterized as relatively “isolated” based on their $37 \mu\text{m}$ images and presented `sedcreator`, a Python package designed to automate the aperture photometry and SED fitting process for protostars. Paper IV also re-analyzed the sources from Papers I-III using this package to produce a sample of 40 uniformly analyzed massive protostars. The results placed constraints on the environmental conditions needed for massive star formation. However, while the SOMA I-IV samples explored sources across a wide range of masses, they excluded sources in highly clustered environments.

Here, in SOMA Paper V, we present 7 regions of “clustered” protostars, defined as MIR sources exhibiting radio emission and surrounded by several other MIR sources within $\sim 60''$. Altogether, we detect and analyze 34 sources within these crowded regions, significantly increasing the size of the SOMA sample. With these new results, we examine whether the trends observed in SOMA I-IV continue to hold in these new regions and discuss the constraints this places on massive star formation theories. This is a critical step in understanding how environment shapes the massive star formation process.

As in SOMA Papers I-IV, we measure fluxes from infrared (IR) images obtained with Spitzer, SOFIA, and Herschel facilities to construct the spectral energy distribution (SED) of each protostar. We fit these SEDs with the Zhang & Tan (2018, hereafter ZT18) radiative transfer (RT) models to constrain the properties of

the protostars. Due to the difficulty in separating the fluxes of sources in these clustered regions, new methods are needed to independently analyze the sources within them. Thus, we also present version 2.0 of `sedcreator`, which includes new and updated tools to explore massive star formation in these environments. This updated package enables the simultaneous analysis of multiple sources in a star-forming region, yielding an individual SED for each source while taking into account nearby sources.

In §2 of this paper, we describe the observations and data we use for our analysis. In §3, we discuss the source detection process we have developed based off of the `Astrodendro` Python package (Robitaille et al. 2019), along with the changes made to the flux calculation and SED fitting methods in `sedcreator` to enable analysis of multiple sources in a region. In §4, we present the MIR to FIR images and results of the SED fitting. In §5, we discuss these results and examine trends in massive star forming environments, and in §6, we provide a summary of the results from the entire SOMA survey to date.

2. OBSERVATIONS

We carried out observations of the seven massive star-forming regions using the Stratospheric Observatory for Infrared Astronomy (SOFIA¹) and the Faint Object infraRed CAmera for the SOFIA Telescope (FORCAST Herter et al. 2018) instrument. We used four filters, centered on 7.7, 19.7, 31.5, and $37.1 \mu\text{m}$. We estimate these 7 regions to possess 34 protostars, using the `Astrodendro` Python package (Robitaille et al. 2019) to identify a list of peaks that we condense using methods described in §3.

We followed the methods of Papers I, II, III, and IV to perform the photometric and astrometric calibrations. We estimate the calibration error of the SOFIA observations to be between $\sim 3\% - 7\%$. The astrometric precision for the SOFIA $7 \mu\text{m}$ image is about $0''.1$, while the value for longer wavelength SOFIA images is about $0''.4$ (see Paper I for further details). We used pipeline-reduced and calibrated data from the SOFIA archive. When available, we supplemented the SOFIA observations with publicly-available images of Spitzer/IRAC (Werner et al. 2004; Fazio et al. 2004) at 3.6, 4.5, 5.8, and $8.0 \mu\text{m}$ from the Spitzer Heritage Archive, and Herschel/PACS and SPIRE (Griffin et al. 2010) at 70, 160,

¹ SOFIA is jointly operated by the Universities Space Research Association, Inc. (USRA), under NASA contract NAS2-97001, and the Deutsches SOFIA Institute (DSI) under DLR contract 50 OK 0901 to the University of Stuttgart.

250, 350, and 500 μm from the ESA Herschel Science Archive.

3. METHODS

Here we describe the new and updated methods we use to identify sources, measure fluxes, and build and fit SEDs in each of the 7 regions in our sample.

3.1. Source Detection

In Papers I-IV of the SOMA survey, source positions were generally derived from radio continuum peaks. However, while visual inspection of each of the SOMA V regions reveals multiple sources, many have not yet been identified in radio continuum data. In addition, given the crowded nature of these regions, flux contamination from neighbors complicates the process of identifying individual sources in the IR images. To address this, we define a method of automatically generating source lists for these clustered regions. We perform this method using the SOFIA 37.1 μm images, with this emission expected to trace hot dust in the inner regions of protostellar envelopes (e.g., Zhang & Tan 2018). We selected this wavelength because SOFIA’s higher angular resolution compared to Herschel 70 μm images aids in distinguishing the sources from one another. Also, using the longest FORCAST wavelength allows us to pierce deeper into the thick gas and dust of star-forming regions. The process works as follows.

First, we apply a median filter with a kernel of 20'' to the 37.1 μm image. We then subtract the resulting median-filtered image from the original image. This makes the sources stand out more sharply against the local background. Next, we run the *Astrodendro* Python package (Robitaille et al. 2019) (see Rosolowsky et al. 2008, for a description of the original dendrogram algorithm) on the resulting image to identify structures above a given brightness threshold and size. We set the minimum size of a source to 3 times that of the beam and the minimum peak height to 6 times the noise. We selected these values after testing multiple combinations and seeing which combination consistently produced reasonable source guesses (determined by eye) for all 7 regions. Since the noise can vary significantly across a single SOFIA image, determining the value from one patch would not be representative of the entire image. To account for this, we cover the image in circular apertures of radius 3.5'', chosen to be comparable to the beam size of the 37.1 μm images, and calculate their enclosed fluxes. Next, we take the median absolute deviation (MAD) of these values and use this as the noise

estimate. We take the MAD instead of the standard deviation to minimize the impact of source flux on the calculation.

After obtaining the source candidates from *Astrodendro*, we perform a down-selection step. The minimum aperture size we use in the SOMA survey is 5'', based on the beam size of the Herschel 70 μm images. As such, we do not allow sources to be closer than 10'' to one another, acknowledging that this could lead to some sources being ignored in highly clustered regions. To ensure that this condition is met, we iterate through the source list and build up a new “down-selected” catalog of sources that fulfill this requirement. We start by adding the brightest source to the new catalog. We then move on to the second brightest source in the original list and add it to the new catalog if it is at least 10'' from the brightest source. We continue to iterate through the remaining original sources, only adding a source to the new catalog if it is farther than 10'' from each of the sources already in the new catalog. After this step is complete, we have our final source catalog and can begin the SED analysis process.

3.2. Sedcreator Version 2.0

To analyze SEDs of sources in crowded regions, we present *sedcreator* version 2.0, an updated version of the open-source Python package presented in Fedriani et al. (2023) and hosted in both GitHub² and PyPi³ (the documentation can be accessed at this URL <https://sedcreator.readthedocs.io/>). The main functionalities of *sedcreator* are partitioned into SedFluxer and SedFitter. SedFluxer provides tools to measure fluxes and build SEDs from an image, using a number of functions from Bradley et al. (2020). It also presents an algorithm to automatically determine the aperture radius for a source. SedFitter fits an SED using a massive star formation radiative transfer model grid by Zhang & Tan (2018). Version 2.0 presents new and updated methods for SedFluxer to analyze protostars in crowded regions. Instead of analyzing each source in isolation, version 2.0 takes in a list of source coordinates in a given region and performs the aperture selection process and flux calculations for each source while considering positions and flux contributions from its neighbors. In the following sections, we describe the updated methods introduced in *sedcreator* version 2.0.

3.2.1. Optimal Aperture Algorithm

² <https://github.com/fedriani/sedcreator>

³ <https://pypi.org/project/sedcreator/>

Table 1. SOFIA FORCAST Observations: Observation Dates & Exposure Times (seconds)

Source	R.A.(J2000)	Decl.(J2000)	d (kpc)	Obs. Date	$7.7 \mu\text{m}$	$19.7 \mu\text{m}$	$31.5 \mu\text{m}$	$37.1 \mu\text{m}$
AFGL 5180	$06^{\text{h}}08^{\text{m}}53^{\text{s}}.3$	$+21^{\circ}38'28''.7$	1.76	2015 Jan 29	268	270
G018.67+00.03	$18^{\text{h}}24^{\text{m}}53^{\text{s}}.8$	$-12^{\circ}39'18''.7$	10.8	2018 Aug 22	346	810	509	1263
G28.37+00.07	$18^{\text{h}}42^{\text{m}}53^{\text{s}}.2$	$-04^{\circ}00'08''.0$	5.00	2018 Sep 06	283	...	1338	773
G030.76+00.20	$18^{\text{h}}46^{\text{m}}44^{\text{s}}.6$	$-01^{\circ}50'29''.8$	6.4	2018 Sep 10	329	911	597	1062
G058.77+00.65	$19^{\text{h}}38^{\text{m}}48^{\text{s}}.8$	$+23^{\circ}09'39''.3$	3.30	2018 Aug 29	1235
IRAS 20343+4129	$20^{\text{h}}36^{\text{m}}07^{\text{s}}.2$	$+41^{\circ}39'51''.3$	1.40	2018 Aug 22	303	852	812	1387
W3 IRS5	$02^{\text{h}}25^{\text{m}}40^{\text{s}}.7$	$+62^{\circ}05'52''.6$	1.83	2015 May 30	116	113	121	113

NOTE— The source positions listed here are the same as the positions of the primary source for each region in Figs. 2, 3, 4, 5, 6, 7, 8. Source distances are from the literature, discussed below (see Sect. 4.2).

Paper IV presents an “optimal aperture algorithm” to determine the aperture size of an isolated extended source in an unbiased and reproducible way. The goal of this algorithm is to find a radius that encompasses most of the source’s flux in an image, while minimizing the background contribution. To achieve this, it estimates the point at which the gradient of the background-subtracted flux as a function of aperture radius drops below a certain value (see Paper IV for details and illustrative plots). If used in a crowded region, this algorithm would overestimate aperture sizes due to flux contributions from neighboring sources. Here, we present an updated version of the algorithm designed to work in crowded regions. In the case where only one source is present, the algorithm works as before. In the case where multiple source positions are inputted, the new algorithm determines each radius while considering all neighboring sources in an iterative process until a solution is converged upon for each one.

This process works as follows. The algorithm takes in an image and a list of source coordinates. Each source is assigned an initial aperture radius of $5''$, the smallest aperture size used in the SOMA survey. Starting with the primary source, the algorithm increases each source’s aperture until the gradient of its enclosed background-subtracted flux reaches a defined threshold (as described in SOMA IV). An aperture’s growth is stopped early if it reaches the central coordinate of another source in the list, regardless of whether the gradient threshold condition has been met. When two or more apertures overlap with one another, each pixel in the region of overlap is assigned to the closest source and excluded from the flux calculations for all other sources. After each source’s aperture has been updated, the algorithm repeats this process, starting at the primary source and cycling through the list again. At the end of each iteration, the algorithm calculates how much each

source’s aperture changed from the previous iteration. As soon as none of the apertures are changing by more than 1%, the algorithm stops iterating and returns the final apertures, along with maps specifying which source each pixel has been assigned to. In the situation where convergence is not reached after a user-defined number of iterations, the algorithm outputs the apertures corresponding to the iteration with the lowest average percent change.

3.2.2. Flux Measurements

Following the fiducial “Fixed Aperture” method described in Papers I-IV, we determine the aperture radius of a given source using its Herschel $70 \mu\text{m}$ image, which is near the peak of the SED, and apply this radius at all wavelengths. The source flux at each wavelength is then obtained through aperture photometry using `sedcreator`’s SedFluxer tool (see Paper IV for details), with several updates. First, the assignment map that the optimal aperture algorithm outputs is used to determine which pixels are assigned to other sources and are thus excluded from this source’s flux measurement. In addition, version 2.0 modifies the error estimation process. The previous method and updates are summarized below.

As in Paper IV, for wavelengths $\lambda > 100 \mu\text{m}$, which are expected to be potentially impacted by confusion with the cold clump environment, we use the background intensity itself as the measure of the error estimate. At shorter wavelengths, Paper IV introduced a method of error estimation via measurement of the fluctuations of the flux within a region of the annulus with an equivalent area to the main aperture. As such, an annulus around the aperture (extending to 2 times the aperture radius) is split into three sectors, and the standard deviation of their fluxes (after aliasing to avoid bias; see Paper IV) is taken as the fluctuation estimate. In crowded re-

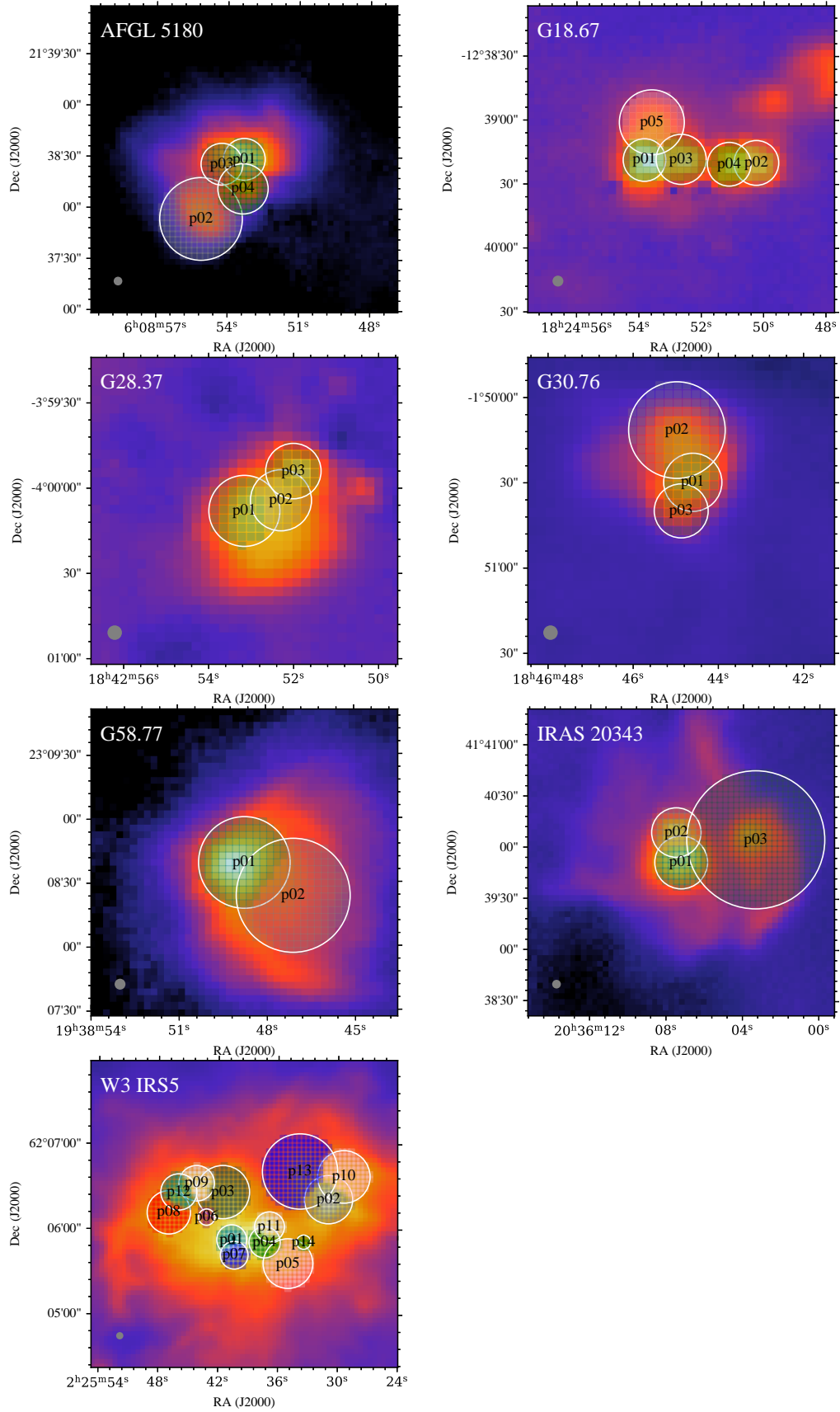


Figure 1. Herschel 70 μm images for each SOMA V region. The color map for each image is normalized by the peak flux in that image. The white circles denote the apertures used for the fiducial photometry. Pixels are colored to show which aperture each pixel is assigned to. Gray circles in the lower left show the resolution of each image. The black crosses in all panels denote the positions of the sources as described in Section 3.

gions, any pixels that belong to a neighboring source’s aperture will be excluded from this calculation. In particularly crowded regions, this could lead to most of the pixels of a given annulus sector being masked out. To address this issue, if any sector of the annulus has 80% or more of its area masked out, we do not include this sector in the fluctuation calculations. If this is true for two or more sectors, we return to the background error estimation method used at long wavelengths. i.e., taking the median of the entire annulus (other than those that are masked out). In addition, if 50% or more of the total annulus is masked out, we default to this background estimation method. Finally, as in SOMA I-IV, an additional assumed flux calibration error of 10% of the background-subtracted flux is added in quadrature to yield a total flux error estimate.

3.2.3. SED Fitting

After constructing the SEDs for each source, we fit them with a grid of radiative transfer models from ZT18, based on the TCA model of massive star formation. In this model, the initial conditions of massive star formation are gravitationally bound prestellar “cores” embedded in a larger-scale “clump” of ambient gas. This core is internally supported by pressure from both turbulence and magnetic fields. When the core collapses, it is assumed to form a single rotationally-supported disk that yields a single star or small N multiple via disk fragmentation. However, in the ZT18 grid of RT models, only the case of single star formation from a core is considered, i.e., the limiting case where a single star dominates the luminosity. The ZT18 grid is constructed from two primary initial condition variables that determine the evolutionary history of the protostar: the initial mass of the core (M_c) and the mass surface density of the clump in which the core is embedded (Σ_{cl}). The current protostellar mass (m_*) indicates where the protostar is in its evolutionary timeline. Together, M_c , Σ_{cl} , and m_* are the main intrinsic properties that define the model grid. In total there are 432 different physical models with different values of these three parameters. Two secondary properties are the inclination angle of the outflow axis to the line of sight (θ_{view}), which is sampled with 20 different values, and the level of foreground extinction (A_V), which is explored up to a maximum value of $A_V = 1000$ mag. To complete the fitting, we use `sedcreator`’s `SedFitter` tool, which fits the ZT grid of $432 \times 20 = 8640$ models to the data, minimizing each model’s χ^2 function over A_V to make the process more efficient. This returns the model parameters and corresponding χ^2 values, in order of “best” to “worst” fit according to its corresponding χ^2 value.

In analysis of the SOMA V regions we find that there are relatively faint, noisy sources being fit with the SED models. Primarily from considering these sources, we make the following updates to the definition of “good” model fits compared to SOMA IV. First, when carrying out the normalization of the reduced χ^2 by the total number of data points, N , we do not count a data point if it is only used as an upper limit to a given model. This mainly applies to the short wavelength data, i.e., $\lambda < 8 \mu\text{m}$, which are treated as being upper limits on the models, since the models do not include contributions from transiently heated small dust grains or from PAH emission features. However, note that if a given RT model predicts a flux that is greater than an upper limit data point, then its χ^2 contribution is counted and the data point is counted in the sum of N . As in SOMA I-IV, we only consider models that satisfy $R_{core} < 2R_{aper}$, where R_{core} is the core radius of the RT model and R_{aper} is the aperture radius found in the images using the above methods. This ensures that only physically consistent core radius are considered.

Then, there are three cases we consider to define a set of “good” models, depending on the value of the minimum value of χ^2 , i.e., χ_{min}^2 :

(i) If $\chi_{min}^2 < 1$, we average over all models with $\chi^2 < 2$ (this is similar to the method of SOMA IV).

(ii) If $1 \leq \chi_{min}^2 \leq 2$, then we average over all models with $\chi^2 < 2$, but also require that at least 10 physical models, i.e., with different combinations of M_c , Σ_{cl} , and m_* . This is designed to make sure there is a reasonable level of sampling over these parameters.

(iii) If $\chi_{min}^2 > 2$, we average over the 10 best physical models, i.e., with different combinations of M_c , Σ_{cl} , and m_* , with the worst of these defining a limiting value χ_{lim}^2 . Then for these models, all viewing angles that yield $\chi^2 < \chi_{lim}^2$ are included.

3.3. Empirical Derivation of Σ_{cl}

To further constrain the parameters derived from the SED fitting process, we empirically calculate the local Σ_{cl} value around each source using the Herschel 70, 160, 250, 350, and 500 μm images. The background fluxes are measured as described in Section 3.2.2, using an annular region around each source that excludes flux from other source apertures. We fit the resulting background SED for each source at these wavelengths with a single-temperature graybody distribution represented by the following equation:

$$I_\nu \simeq B_\nu(1 - e^{-\tau_\nu}) = B_\nu(1 - e^{-\Sigma_{cl}\kappa_\nu}), \quad (1)$$

where I_ν is the intensity observed at a given frequency, B_ν is the Planck function, τ_ν is the dust optical depth, and κ_ν is the dust opacity. For consistency, we use the same opacities as ZT18 used when constructing the grid of RT models. These values come from the opacity law defined by Whitney et al. (2003). We use the `curve_fit` function of the SciPy optimize Python package to perform the graybody fitting. We assign a 10% error to the background flux values. We then use the covariance matrix returned by `curve_fit` to obtain uncertainties on the resulting Σ_{cl} values.

4. RESULTS

We first (in §4.1) describe some general results of the SED fitting of the SOMA V sources and then (in §4.2) present summaries of individual regions. Then, in the following section, §5, we describe the results of analysis of the overall SOMA I-V sample.

4.1. Source Images and SEDs

Overall, in the seven regions of clustered massive star formation, we have identified and characterized a total of 34 sources. The algorithmically-obtained apertures and pixel assignment maps for these sources are shown on top of the Herschel 70 μm images in Figure 1.

Multi-wavelength SOFIA-FORCAST images from 7.7 to 37 μm and archival Spitzer-IRAC 8 μm and Herschel-PACS 70 μm images (when available) for each region, including identified sources and their apertures, are presented in Figures 2 to 8. The aperture radii and fluxes obtained for each source are listed in Table B1.

To build the SED for each source, we consider fluxes, when available, from Spitzer-IRAC images at 3.6, 4.5, 5.8, and 8.0 μm , SOFIA-FORCAST images at 7.7, 19.1, 31.5, and 37.1 μm , and Herschel-PACS/SPIRE 70, 160, 250, 350, and 500 μm . As described in Section 3, the fluxes are obtained through aperture photometry using the `SedFluxer` functionality of `sedcreator` version 2.0, where we have updated the package to enable usage in crowded regions.

Figure A2 shows the measured SEDs for each source in this sample, with the good model fits overlaid. For 24 of the 34 SOMA V sources, the best fitting model has $\chi^2 < 1$. Three sources have a best fit with $1 < \chi^2 < 2$. The following seven sources have relatively poor fits for their best models: G30.76 p01 ($\chi_{\text{min}}^2 = 3.1$); IRAS20343 p01 ($\chi_{\text{min}}^2 = 5.9$); W3 p01 ($\chi_{\text{min}}^2 = 20.98$); W3 p06 ($\chi_{\text{min}}^2 = 2.3$); W3 p09 ($\chi_{\text{min}}^2 = 3.3$); W3 p11 ($\chi_{\text{min}}^2 = 2.4$); and W3 p12 ($\chi_{\text{min}}^2 = 2.7$). Thus we see that most of the SOMA V SEDs are reasonably well fit with the RT models, suggesting that they are protostars forming in a manner consistent with the Turbulent Core Accretion model.

The three primary physical parameters constrained by the SED fitting process are the initial core mass (M_c), mass surface density of the surrounding clump environment (Σ_{cl}), and current protostellar mass (m_*). Figure A3 shows the good model distributions in the $\Sigma_{\text{cl}}-M_c$, m_*-M_c , and $m_*-\Sigma_{\text{cl}}$ planes for each source. This figure thus displays the degeneracies that arise from deriving protostellar properties via SED fitting alone.

Table B2 lists the properties of the best five models and the average and dispersion of all the good models. When an empirical measure of Σ_{cl} is available via graybody fitting, then the average of only those good models with Σ_{cl} set equal to the nearest (in logarithmic space) value in the model grid to that of $\Sigma_{\text{cl,GB}}$. Averages are calculated as in SOMA IV, where all good models are equally weighted, including models with the same intrinsic physical properties but different viewing angles (however, note that only the best value of A_V is considered for these).

4.2. Region summaries and identified sources

4.2.1. AFGL 5180

AFGL 5180 (also known as G188.95+0.89 or S252) is a massive star-forming region located at a distance of $1.76 \pm 0.11 \text{ kpc}$ (Oh et al. 2010). AFGL 5180 is part of the Gemini OB1 star-forming complex (Zucker et al. 2020) and has been shown to be the source of bright Class II 6.7 GHz methanol maser emission (Menten 1991; Goedhart et al. 2014). Mutie et al. (2021) reported eight 1.3 mm sources in this region. AFGL 5180 also hosts multiple outflows, identified in $^{12}\text{CO}(2-1)$ line emission by Mutie et al. (2021). Crowe et al. (2024) studied this region using high-resolution near-infrared (NIR) imaging data and identified at least three outflows, consistent with multiple driving sources.

Figure 2 shows the multiwavelength data for AFGL 5180. SOFIA 19.7 μm and 31.5 μm data were not available for this region. Four sources were found using the detection algorithm operating on the 37 μm image. We note that there is a relatively faint 37 μm source seen to the north of the main cluster that does not meet the threshold to be identified by the algorithm. While this source is visible at 7.7 μm , it does not stand out at 70 μm .

As described below, the SED fitting results imply that p01, p02 and p03 are massive protostars with $m_* \sim 12 - 16 M_\odot$, while p04 has $\sim 5 M_\odot$. Protostar p01, with $m_* \simeq 12_{-5}^{+8} M_\odot$ is the primary outflow driving source of S4/mm1 discussed in the NIR study by Crowe et al. (2024). Protostar p04 is associated with AFGL 5180 S region discussed by Crowe et al. (2024). Protostars p02 and p03 were not specifically discussed

by Crowe et al. (2024). However, p02 is co-located with a bright NIR star apparent in their HST/WFC3-IR images. It is possible that this star is already formed and locally heating dust of a molecular cloud to give appearance of a protostellar SED. Similarly, we note that p03 coincides with the NIR reflection nebula that is likely tracing the outflow cavity of p01. Thus, even though the source appears quite spatially concentrated at $37 \mu\text{m}$, it is possible that this region is externally heated and masquerading as a protostar. The absence of significant mm emission from this region (see Mutie et al. 2021; Crowe et al. 2024) tends to favor this latter interpretation. These examples in AFGL 5180 highlight the caveats of protostellar source characterization from MIR - FIR imaging and SED fitting. In the particular case of p01, our inferred source luminosity and protostellar mass may be underestimates, i.e., if the fluxes from p03 should be included in this source.

4.2.2. *G18.67+00.03*

G18.67+00.03 is a massive protocluster located at a distance of 10.8 kpc (Cyganowski et al. 2012) and identified using GLIMPSE $4.5 \mu\text{m}$ images from Cyganowski et al. (2008). Cyganowski et al. (2012) detected four compact 1.3 mm continuum sources in this region, three of which are known 44 GHz Class I CH_3OH maser sources (Cyganowski et al. 2009). Two of these sources also correspond to 6.7 GHz Class II CH_3OH masers. Species including SO, DCN, CH_3OH , H_2CO , and CO isotopes have all been detected toward these sources. Each of the three maser sources exhibits both redshifted and blueshifted $^{13}\text{CO}(2-1)$ emission offset from one another and centered on a compact source, implying the presence of bipolar molecular outflows (Cyganowski et al. 2012).

Figure 3 shows multiwavelength data of G18.67+00.03, where five sources are identified. Four of these correspond to the 1.3 mm continuum sources of Cyganowski et al. (2012), and an additional fainter source has been found slightly to the north of these. All five sources are in the Hi-GAL catalog (Molinari et al. 2016).

From our SED fitting results we find that p01 - p03 in this region are protostars with $m_* \sim 20 M_\odot$, while p04 has $\sim 18 M_\odot$ and p05 has $\sim 14 M_\odot$. Thus, all five sources are massive protostars. We note the striking linearity of the apparent spatial distribution of p01 to p04. We also note that given the relatively large distance to this region, the projected separation between the protostars, i.e., $\sim 10''$ corresponds to relatively large scales of about 0.5 pc.

4.2.3. *G28.37+00.07*

G28.37+00.07 (also known as Cp23 in Moser et al. 2020) is located in IRDC G28.37+00.07 (also known as IRDC C in the sample of Butler & Tan 2009, 2012), which is one of the most massive IRDCs in the Galaxy. The source has a kinematic distance of about 5 kpc (Simon et al. 2006). From near-IR (NIR) and MIR extinction maps, the mass of IRDC G28.37+00.07 is estimated to be $68,300 M_\odot$ (Kainulainen & Tan 2013). Lim & Tan (2014) used sub-mm dust emission observed by Herschel to estimate its mass as $72,000 M_\odot$. G28.37+00.07 is one of the most crowded regions in the IRDC, with four sources in the Hi-GAL catalog. In the previous SED analysis of the region by Moser et al. (2020), G28.37+00.07 was unresolved and was modeled as a single source with $m_* = 8 M_\odot$, an initial core mass of $M_c \simeq 300 M_\odot$, and a current core envelope mass of $M_{\text{env}} = 300 M_\odot$.

Figure 4 shows the multiwavelength data for G28.37+00.07. We note that SOFIA $19.7 \mu\text{m}$ data were available, but contained negative flux artifacts and so were not used in the analysis. Three sources were detected for this region, two of which correspond to sources in the Hi-GAL catalog. In Figure 4, we can see a fainter source to the right of the other three, but this source did not meet our detection threshold.

From our new SED fitting results we find that p01 has a mass of $m_* \sim 14 M_\odot$. The source p02 is estimated to have $m_* \sim 5 M_\odot$, while p03 is estimated to have $m_* \sim 8.5 M_\odot$. We note that the uncertainties in these masses are relatively large, so that these estimates are consistent with that of Moser et al. (2020).

4.2.4. *G30.76+00.20*

G030.76+00.20 is a massive star-forming region located at a distance of 6.4 kpc (Veneziani et al. 2013). A FIR source was first reported at this location in the Herschel Hi-GAL catalog (Molinari et al. 2016). Figure 5 shows the multiwavelength data available for this region. Three sources were identified, each with $m_* \sim 10 - 15 M_\odot$.

4.2.5. *G58.77+00.65*

G58.77+00.65 was first reported in the CORNISH survey of ultra-compact H II region candidates (Kalcheva et al. 2018). This region is located at a distance of 3.3 kpc (Mège et al. 2021). Multiwavelength data for G58.77+00.65 are shown in Figure 6. Unfortunately, SOFIA 7.7, 19.7, and $31.5 \mu\text{m}$ data were not available for this region. Four sources were originally detected in this region, three of which were located within a projected circular radius of $\sim 6''$, which may indicate a very high protostellar number density. However, for our SED fitting two of these were removed during the source down

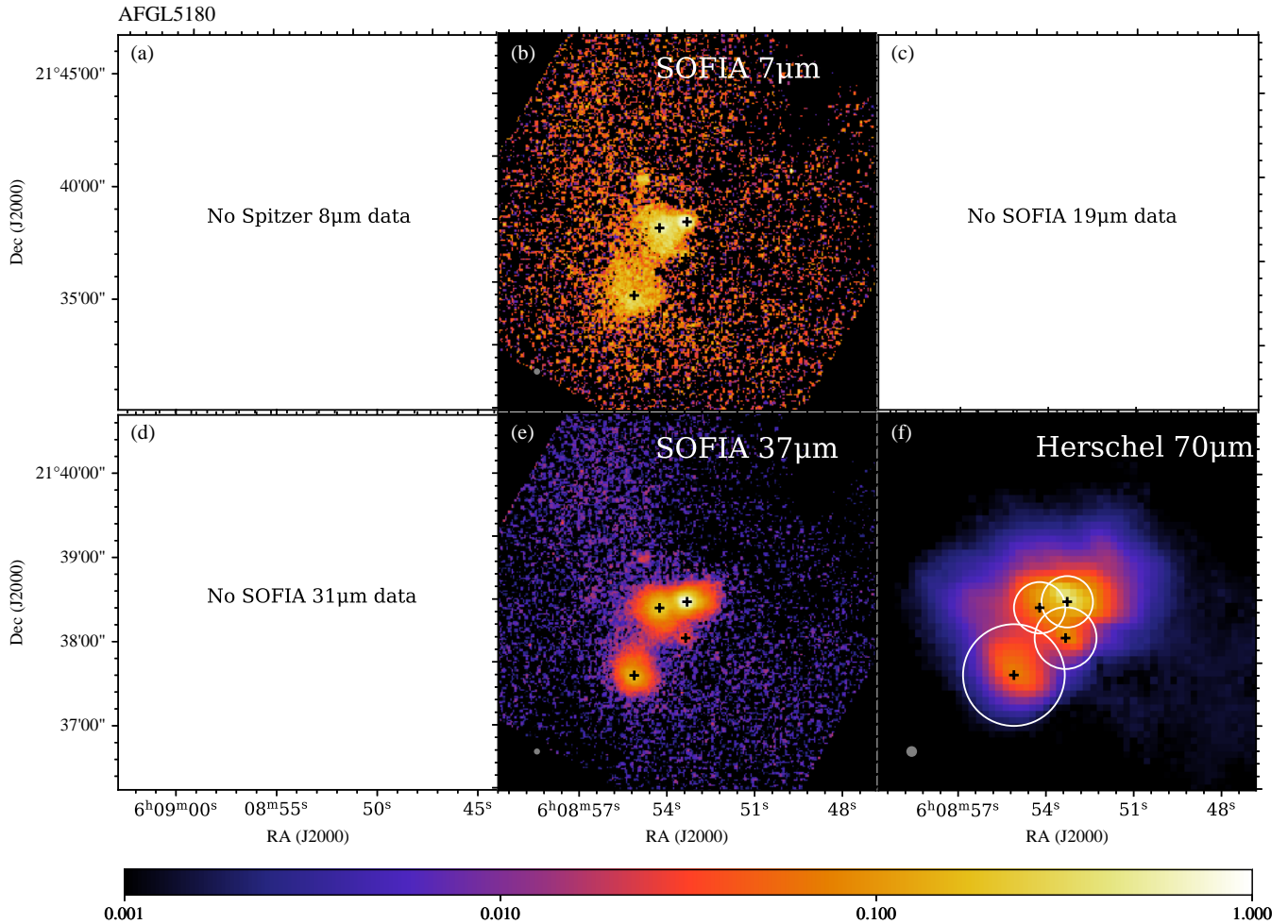


Figure 2. Multiwavelength images of AFGL 5180 with the facility and wavelength given in the upper right of each panel. The color map indicates the relative flux intensity compared to that of the peak flux in each image panel. The white circles shown in (f) denote the apertures used for the fiducial photometry. Gray circles in the lower left show the resolution of each image. The black crosses in all panels denote the positions of the sources as described in Section 3.

selection process, which ensures that no two sources are within $10''$ of one another. The brightest of the remaining sources corresponds with a Hi-GAL-identified source (Molinari et al. 2016). Since this source aperture also contains the removed sources, its flux measurements may be overestimates of the flux from the primary source in the region. With this caveat in mind, our SED fitting of p01 indicates $m_* \sim 13 M_\odot$. The other source that is resolved in the region, i.e., p02, is inferred to have $m_* \sim 11 M_\odot$.

4.2.6. IRAS 20343+4129

IRAS 20343+4129 was first reported in the Sridharan et al. (2002) list of high-mass protostellar candidates, which listed its distance as 1.4 kpc. This region hosts two massive molecular outflows (Beuther et al. 2002) and three K-band continuum YSOs exhibiting circumstellar H_2 emission (Kumar et al. 2002). Campbell et al.

(2008) found two of these sources to have mid-IR counterparts (IRS 1 and IRS 3). The brighter of the two CO outflows is located between these two sources and is oriented north-south, with red and blue lobes that are extended east-west (Campbell et al. 2008). Kumar et al. (2002) suggest that the extended H_2 emission in the east-west direction towards IRS 1 is attributed to a circumstellar disk perpendicular to the outflow axis orientation. Palau et al. (2007) detected a 1.3 mm dust peak and a CO(2-1) peak that coincide with IRS2 and argued that the source is a low- or intermediate-mass YSO.

Figure 7 shows some of the data available for IRAS 20343+4129. Three sources were detected using the methods described in §3. The fainter source seen to the south of p03 did not meet our detection threshold. From SED fitting we find that p01 and p02 can both be fit by protostellar RT models with $m_* \sim 10 M_\odot$. The

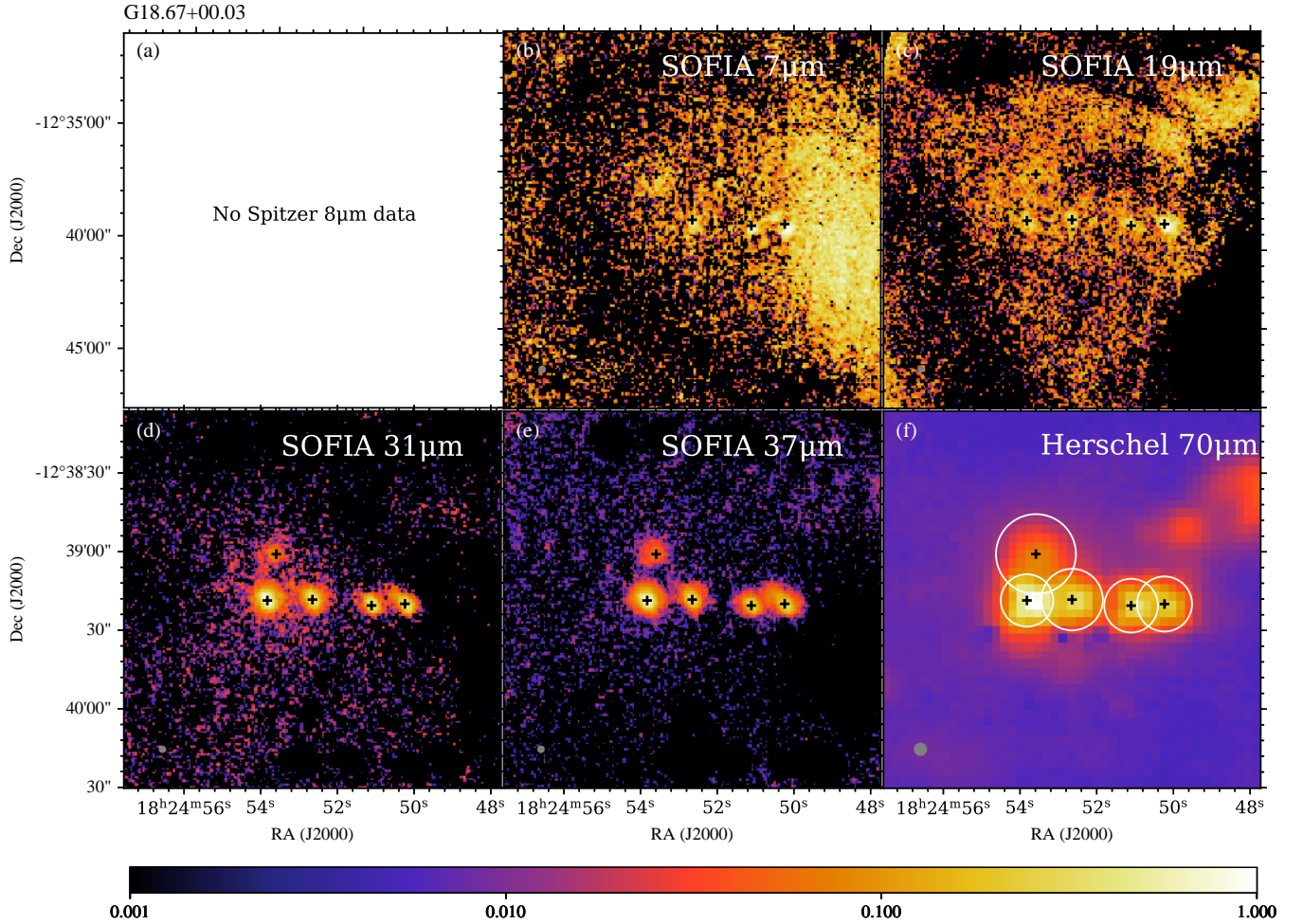


Figure 3. Multiwavelength images of G18.67+0.03, following the format of Figure 2.

third source, p03, which we note has a larger aperture, can be fit with a similarly massive model.

4.2.7. W3 IRS5

W3 IRS5 is a massive star-forming region within the Perseus arm located 1.83 ± 0.14 kpc away (Imai et al. 2000). Campbell et al. (1995) estimated its total luminosity to be $2 \times 10^5 L_{\odot}$. It has a high stellar projected number density of 10^4 pc^{-2} , estimated by Megeath et al. (2008) using near-IR observations. Using 1.4 mm observations with the Plateau de Bure Interferometer (PdBI), Rodón, J. A. et al. (2008) estimated the protostellar number density to be $> 10^6 \text{ pc}^{-3}$. The close and dense nature of W3 IRS5 make it an interesting region in which to study massive star formation in a clustered environment (Wang, K.-S. et al. 2013). From (sub)millimeter observations, W3 IRS5 is also known to have a physically and chemically complex molecular structure (Wang, K.-S. et al. 2013). Bipolar outflows have been detected using CO (e.g., Mitchell et al. 1992; Ridge, N. A. & Moore, T. J. T. 2001) and SiO (e.g., Gibb et al. 2007; Rodón,

J. A. et al. 2008), likely driven by infrared sources NIR1 and NIR2 (Megeath et al. 2005). NIR1 and NIR2 are coincident with two hypercompact H II regions detected by van der Tak, F. F. S. et al. (2005) in the mid-IR.

Figure 8 shows our SOFIA multiwavelength data of W3 IRS5. Fourteen protostar candidates have been identified using our source detection algorithm. The primary source, p01, is located near the center of the region and has an inferred $m_* \sim 10 - 20 M_{\odot}$, depending on whether or not restricted SED fitting is carried out using the empirical estimate of $\Sigma_{\text{cl,GB}}$. However, we note that this is a source for which the best-fit model has a very poor $\chi^2 \sim 15$. From inspection of the fits, this may indicate difficulties in resolving the true FIR fluxes near the peak of the SED. The other 13 sources are generally fit quite well by the RT models. The next three sources, p02 - p04 have $m_* \sim 20 M_{\odot}$. Among the remaining sources, are all good candidates for being massive protostars with estimations of $m_* \gtrsim 8 M_{\odot}$. We caution that not all of these sources show concentrated morphologies

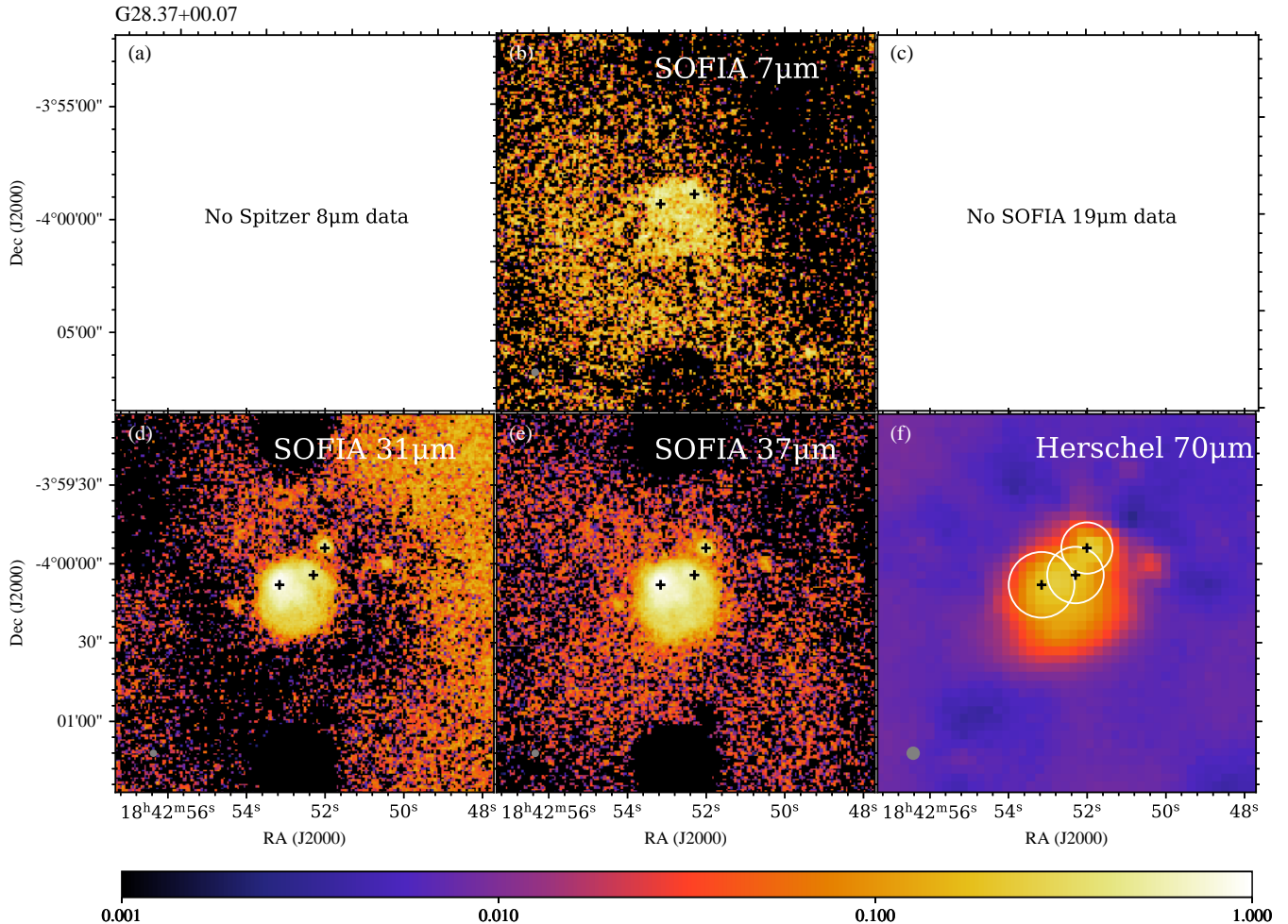


Figure 4. Multiwavelength images of G28.37+00.07, following the format of Figure 2.

in their MIR-FIR emission, so there may be some confusion with externally heated structures. Similarly, there are some relatively faint, but concentrated sources that we see in the SOFIA-FORCAST images, but which do not enter our source list, either because they fail to meet the detection threshold at $37\ \mu\text{m}$ or because they are too close to other sources for resolution of their FIR emission.

5. GLOBAL SOMA SURVEY RESULTS

Here we discuss the results from the 34 protostellar candidate sources identified in the 7 regions presented in this paper, along with the sources presented in Papers I-IV of the SOMA survey, but re-analyzed with the updated definitions of “good” SED model fits described above.

5.1. Graybody-derived Σ_{cl}

Here we examine results of the graybody-derived values of mass surface density, i.e., $\Sigma_{\text{cl,GB}}$. This is a more

direct, empirical measure of the mass surface density of the clump environment compared to that inferred from the SED fitting of the protostellar models, i.e., $\Sigma_{\text{cl,SED}}$. Our goals are thus to see how well these compare, but also to examine results of “restricted SED fitting”, when $\Sigma_{\text{cl,SED}}$ is forced to be the value in the ZT18 model grid that is closest to the observed $\Sigma_{\text{cl,GB}}$.

We first examine the sensitivity of the measurement of $\Sigma_{\text{cl,GB}}$ to whether or not the Herschel $70\ \mu\text{m}$ flux values are included. Figure 9a shows that $\Sigma_{\text{cl,GB}}$ increases by about a factor of two when we remove the $70\ \mu\text{m}$ fluxes from the graybody fitting process. Note, the emission at $70\ \mu\text{m}$ could be dominated by warmer dust that is not well represented by a single temperature graybody model (e.g., see Guzmán et al. 2015). However, from our tests on comparing Σ_{c} measurements of protostellar cores defined by the remaining envelope mass (see Appendix A), we find that more accurate results are obtained by including the $70\ \mu\text{m}$ flux. Thus we retain this method as our fiducial case, but acknowledge that

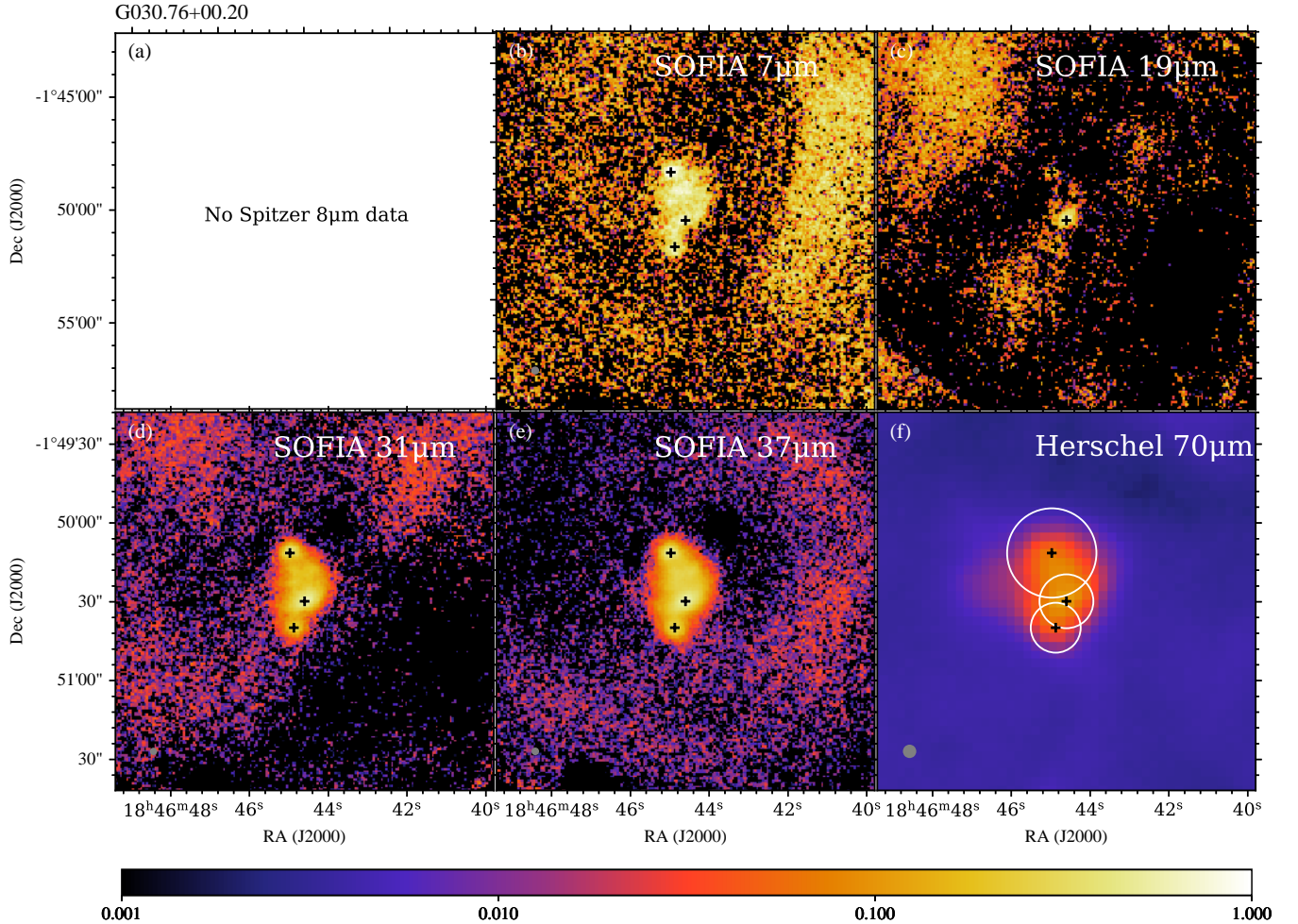


Figure 5. Multiwavelength images of G30.76+00.20, following the format of Figure 2.

systematic uncertainties, perhaps up to a factor of two, result from the approximation of the emitting material as a single temperature graybody.

In addition, it is important to note that the derived $\Sigma_{\text{cl,GB}}$ values depend on the choice of the opacity law. If we instead use the opacity values from [Ossenkopf & Henning \(1994\)](#) for grains with a thin ice mantle (as used by [Lim et al. \(2016\)](#) in the study of cold IRDC environments), we obtain $\Sigma_{\text{cl,GB}}$ values that are factors of about three times smaller for each source. Thus, the choice of dust opacity may be the dominant source of systematic uncertainty in the measurement of $\Sigma_{\text{cl,GB}}$.

Figure 9b compares $\Sigma_{\text{cl,GB}}$ values with those derived from SED fitting, $\Sigma_{\text{cl,SED}}$, i.e., the average of good models. Note, these include all the sources of this paper (SOMA V), but only those sources of SOMA I - IV that have Herschel data allowing the $\Sigma_{\text{cl,GB}}$ measurement. We see that $\Sigma_{\text{cl,SED}}$ values are typically in reasonable agreement with $\Sigma_{\text{cl,GB}}$, but with a tendency to be, on average, modestly larger by within a factor of two.

However, given the potential systematic uncertainties in $\Sigma_{\text{cl,GB}}$, discussed above, and in $\Sigma_{\text{cl,SED}}$, we conclude that their agreement is satisfactory, i.e., within expectations. One can also see from Fig. 9b that the individual uncertainties in $\Sigma_{\text{cl,SED}}$, which are the dispersion of the “good” model fits, are generally larger than the intrinsic uncertainties in $\Sigma_{\text{cl,GB}}$ (i.e., ignoring systematic uncertainties in assumptions of single temperature graybody and choice of dust opacities). This motivates the case of “restricted SED fitting” in which we set $\Sigma_{\text{cl,SED}}$ to be the value in the ZT18 model grid that is closest to $\Sigma_{\text{cl,GB}}$ of a given source.

5.2. The Environmental Conditions for Massive Star Formation

Figure 10(a) shows clump environment mass surface density as derived from SED fitting, $\Sigma_{\text{cl,SED}}$, versus initial core mass, M_c , showing the average of “good” models. The SOMA I-IV and V samples are plotted, as well as samples of protostars identified in infrared dark

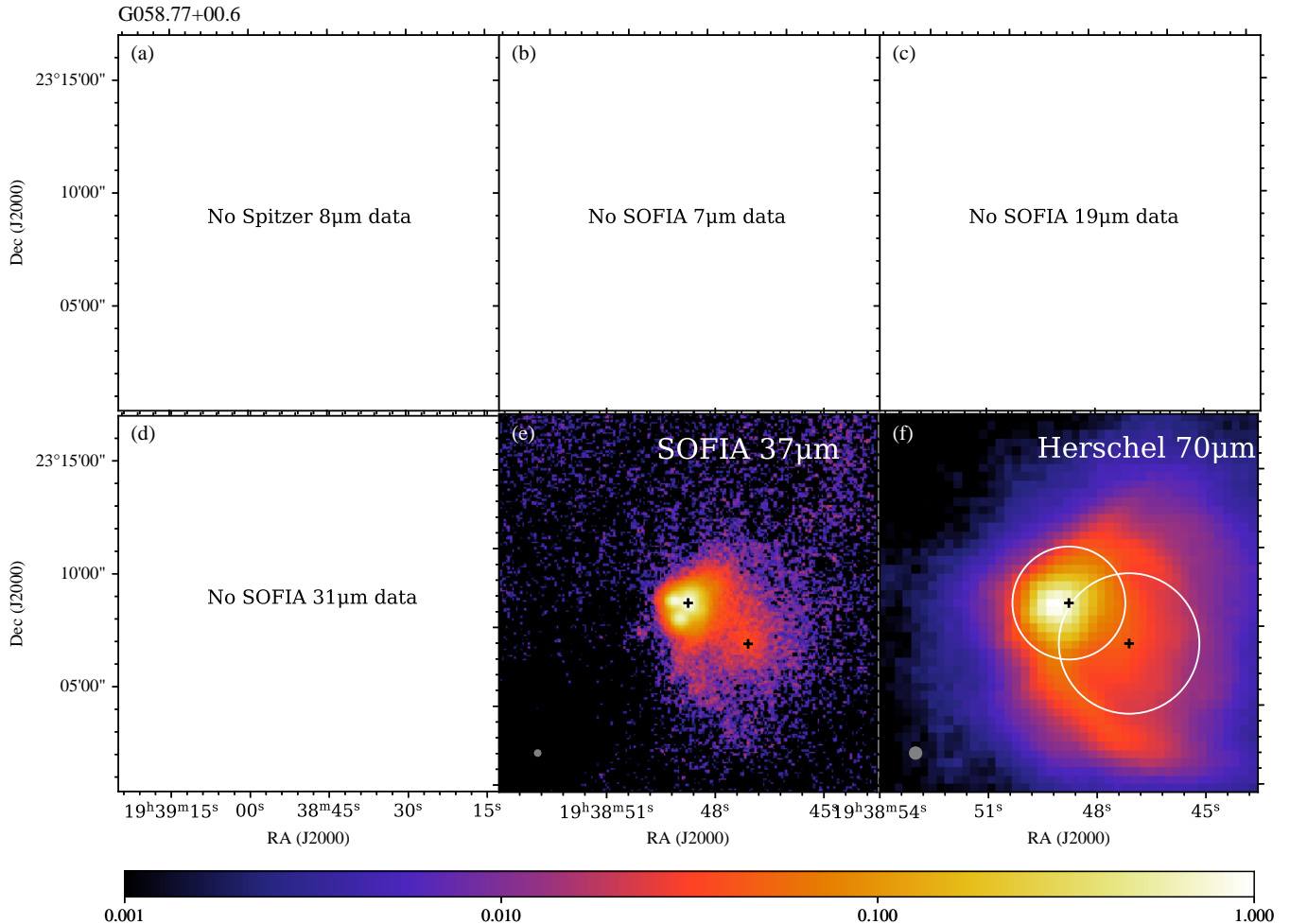


Figure 6. Multiwavelength images of G58.77+00.65, following the format of Figure 2.

clouds (IRDCs) (Moser et al. 2020; Liu et al. 2021). The data points are also color coded by the SED-derived current protostellar mass, m_* . Figure 10(b) plots the equivalent results, but for $\Sigma_{\text{cl,GB}}$ and showing only those SOMA sources with Herschel data. Figure 10(c) is the same as (b), but showing the results of restricted SED fitting where $\Sigma_{\text{cl,SED}}$ has been set equal to a value in the ZT18 grid closest to $\Sigma_{\text{cl,GB}}$. Figure 11(a) shows m_* versus M_c for the SOMA I-V and IRDC samples, while Figure 11(b) shows the results of the $\Sigma_{\text{cl,GB}}$ -restricted fitting.

We see that the initial core mass of the SOMA V sample ranges from $M_c \sim 30 - 200 M_\odot$, i.e., a somewhat narrower range than that covered by the ZT18 model grid ($10 - 480 M_\odot$) and that found in the SOMA I-IV and IRDC samples. The SOMA V sample shows a broad range of $\Sigma_{\text{cl,SED}}$ from $\sim 0.1 - 3 \text{ g cm}^{-2}$, i.e., the full range covered by the ZT18 models. However, as also shown in Fig. 9, we note that $\Sigma_{\text{cl,GB}}$ occupies a systematically lower range that extends up to $\sim 1.5 \text{ g cm}^{-2}$.

The current protostellar mass of the SOMA V sources ranges from $m_* \sim 4 - 40 M_\odot$. As with initial core mass, this appears to be a somewhat narrower range than found in the SOMA I-IV plus IRDC samples. In the overall sample, we see that IRDC sources tend to represent earlier evolutionary stage protostars, i.e., with $m_* \sim 0.01 - 0.1 M_c$, while the SOMA sources typically have $m_* \simeq 0.1 - 0.3 M_c$.

Figure 12(a) shows the current protostellar mass m_* versus clump environment mass surface density Σ_{cl} , as derived from the SED fitting of “good” models. Figure 12(b) shows the equivalent results, but with Σ_{cl} now derived empirically from the graybody fitting around the source. Figure 12(c) is the same as (b), but with restricted SED fitting using the graybody fitting results to constrain $\Sigma_{\text{cl,SED}}$.

Some models of massive star formation predict that in order to form massive protostars, a minimum value of Σ_{cl} is required. For example, Krumholz & McKee (2008) (hereafter KM08) predicted that in order for high-mass

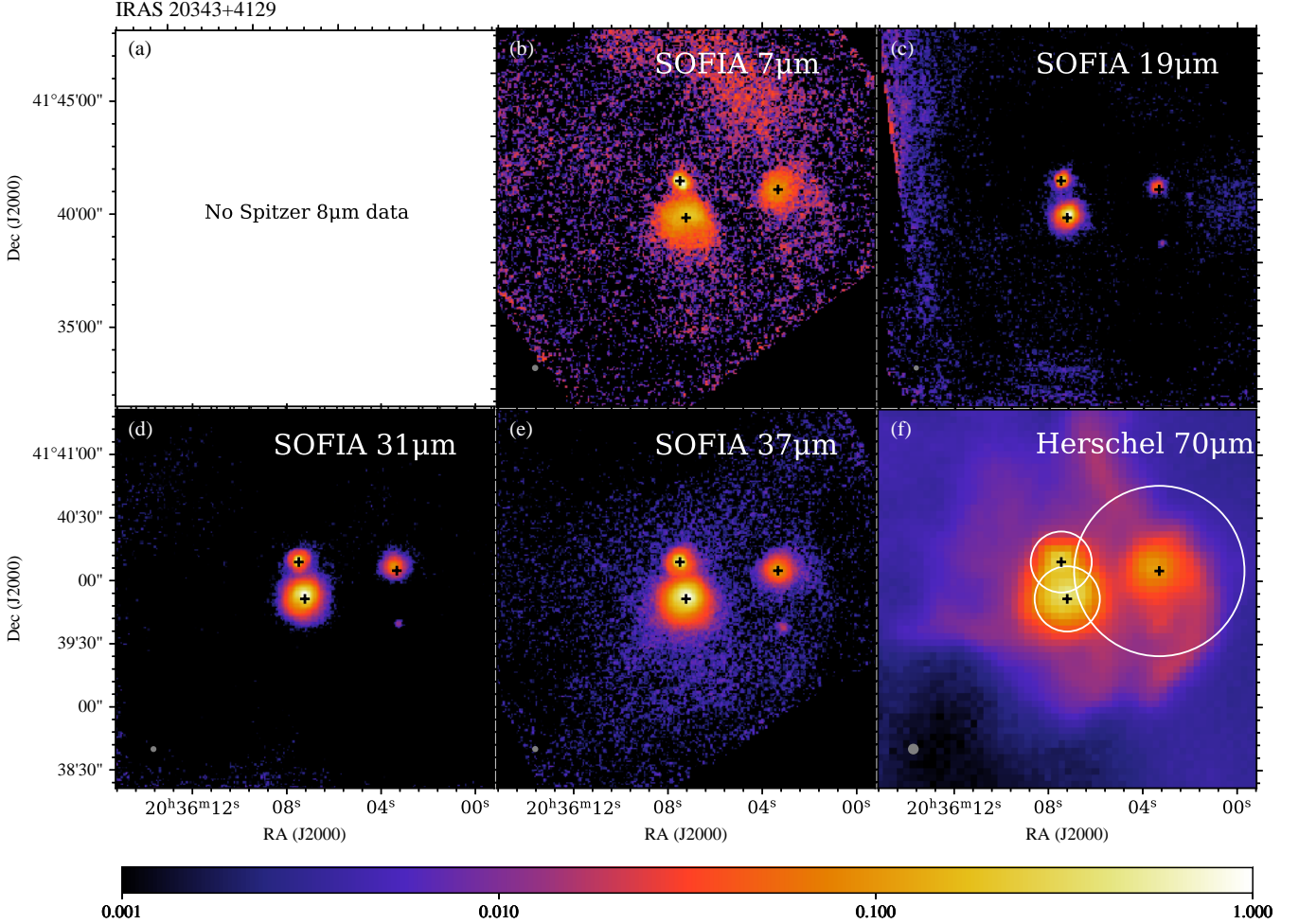


Figure 7. Multiwavelength images of IRAS 20343+4129, following the format of Figure 2.

stars to form, Σ_{cl} must be $\gtrsim 1 \text{ g cm}^{-2}$, with these conditions being needed so that a surrounding population of low-mass protostars has high enough accretion rates and luminosities to heat up the massive core, increase the Jeans mass, and prevent its fragmentation. The panels in Figure 12 show the KM08 condition on Σ_{cl} to form a star of a given mass m_* with red solid lines. As already noted in the SOMA IV paper, the derived properties of the SOMA and IRDC protostars are distributed broadly across a range of Σ_{cl} values that extend far below the KM08 limit. The results for $\Sigma_{\text{cl,GB}}$ extend to even smaller values, so that relatively few sources are above the KM08 limit. Thus, even with the possibility of factors of several systematic uncertainties in Σ_{cl} from graybody fitting (see above), these results do not indicate any evidence for a threshold Σ_{cl} being needed for massive star formation. An alternative mechanism of preventing fragmentation via magnetic field support (requiring $\gtrsim 0.1 \text{ mG}$ field strengths) has been proposed by Butler & Tan (2012), with there being increasing

observational evidence for such dynamically important B -fields present in early-stage (e.g., Law et al. 2024) and late-stage (e.g., Wang et al. 2014; Beltrán et al. 2024) protostellar cores.

The TCA model of McKee & Tan (2002, 2003) predicts that higher Σ_{cl} leads to higher pressures in a self-gravitating clump and thus higher prestellar core densities. This leads to more efficient star formation from a core experiencing internal feedback processes from the protostar (Tanaka et al. 2017). For example, a $M_c = 100 M_\odot$ core forms only a $\sim 20 M_\odot$ star in a $\Sigma_{\text{cl}} \sim 0.1 \text{ g cm}^{-2}$ environment, but a $\sim 50 M_\odot$ star in a $\sim 3 \text{ g cm}^{-2}$ environment. This example result for a $100 M_\odot$ core is shown by the green dashed line in the panels of Fig. 12.

The SOMA IV paper found tentative evidence for the upper envelope of the points in the $m_* - \Sigma_{\text{cl}}$ diagram following the shape of this TCA internal feedback prediction. The equivalent results of our analysis including the SOMA V sources are shown in Fig. 12a. Since the

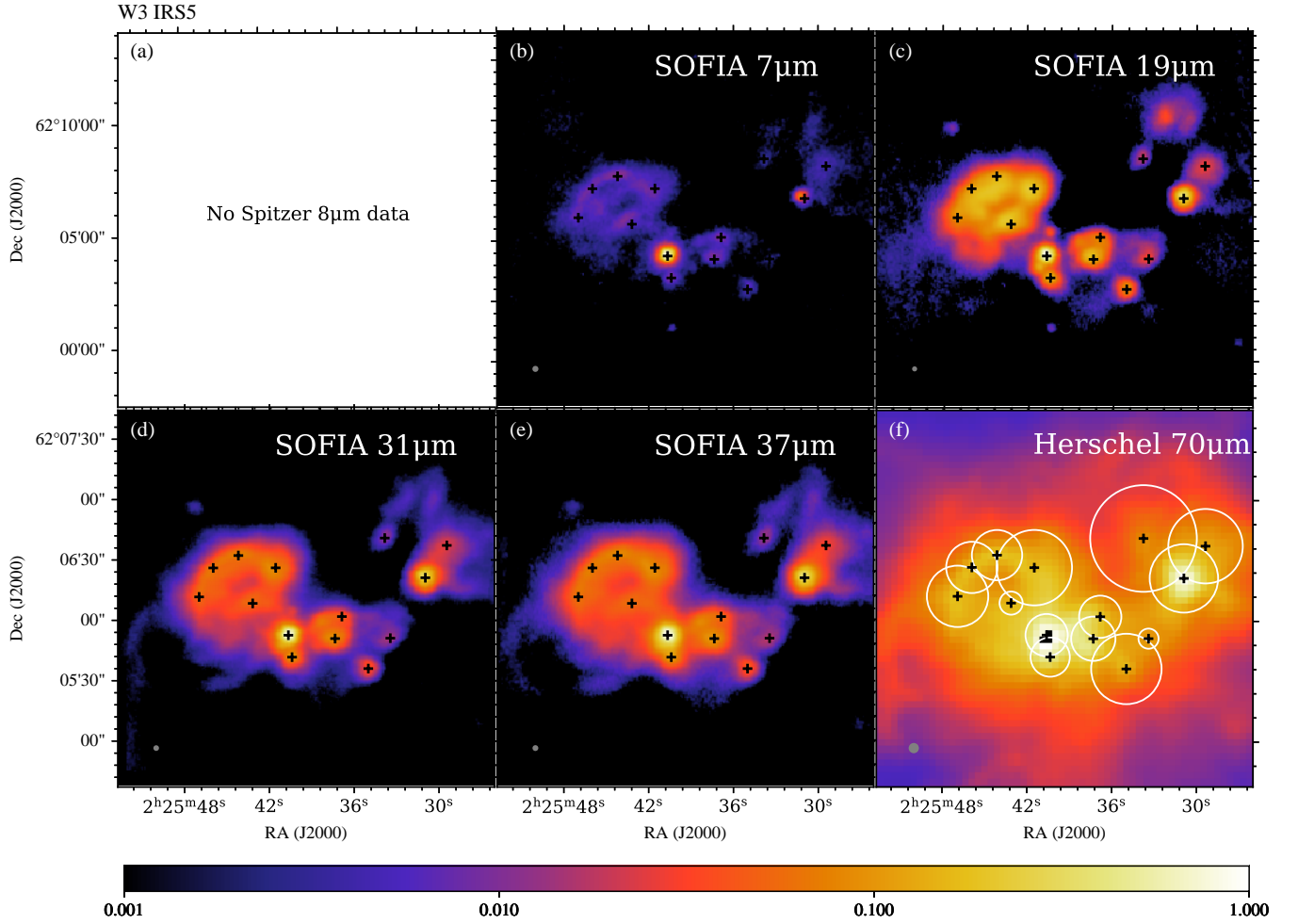


Figure 8. Multiwavelength images of W3 IRS5, following the format of Figure 2.

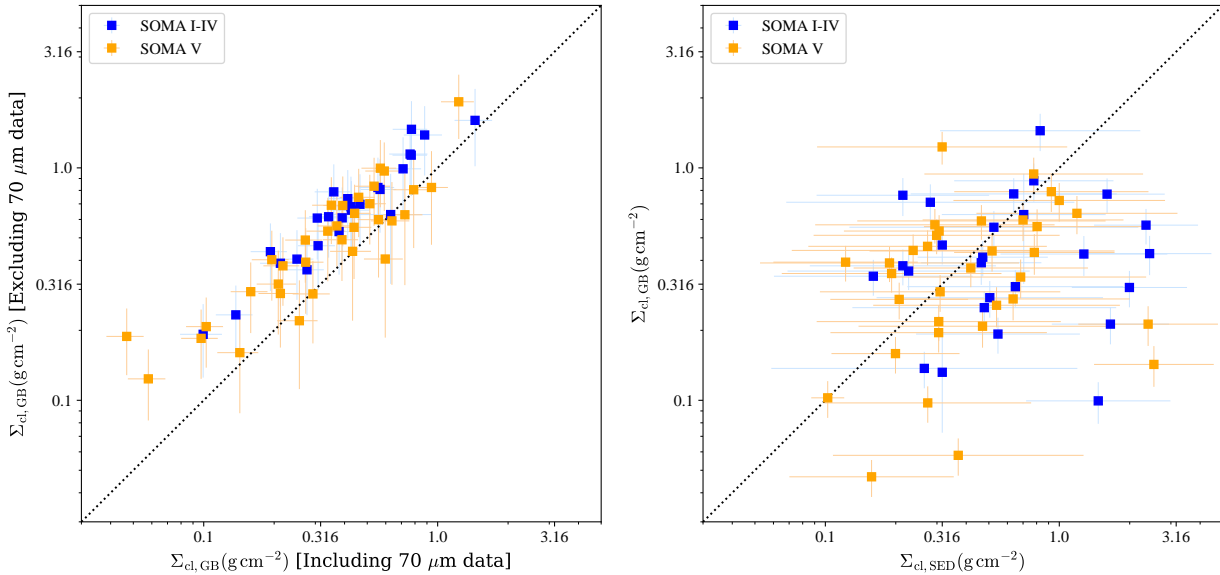


Figure 9. (a) Left: Comparison of $\Sigma_{cl,GB}$ measured only with Herschel 160 to 500 μ m fluxes versus that measured with Herschel 70 to 500 μ m fluxes. (b) Right: Comparison of $\Sigma_{cl,GB}$ (measured using Herschel 70 to 500 μ m fluxes) versus $\Sigma_{cl,SED}$.

SOMA I-IV sources define the most massive end of the

distribution, this result still holds: i.e., the most mas-

sive, $\gtrsim 30 M_{\odot}$ protostars tend to require $\Sigma_{\text{cl}} \gtrsim 1 \text{ g cm}^{-2}$ and the upper envelope could be bounded by the protostars expected to form from $\sim 200 M_{\odot}$ cores. However, when we consider the results of $\Sigma_{\text{cl,GB}}$ shown in Fig. 12b and c, this trend becomes less clear. There are examples of $\sim 50 M_{\odot}$ protostars forming in clump environments of only $\sim 0.1 \text{ g cm}^{-2}$ and little hint of an increasing upper envelope of m_* with increasing Σ_{cl} . In the context of the TCA models, which are being fit to these sources, this requires the initial core masses in the low- Σ_{cl} environments to be systematically more massive. A related point is that with lower values of Σ_{cl} from graybody fitting, the restricted SED fitting results with these conditions tend to increase the derived values of m_* . This is explained by the fact that lower Σ_{cl} values imply lower accretion rates, so that a larger m_* is needed to produce a given bolometric luminosity.

In Figure 12, we also notice that most of the SOMA V sources have $m_* \lesssim 25 M_{\odot}$ (marked by the upper gray dashed line). Figure 13 compares the mass distribution for the SOMA I-IV sources to the distribution for the SOMA V sources, before and after restricting the range of good models based on the graybody-derived Σ_{cl} values. Again, we see that SOMA V sources are somewhat lacking from the highest m_* bins.

Nevertheless, this result could indicate an environmental dependence on the initial mass function of stars at the high-mass end, i.e., the most massive stars ($\gtrsim 30 M_{\odot}$) do not form in clustered environments. The five SOMA sources with the most massive values of m_* are: G45.12+0.13 and G309.92+0.48 (presented in SOMA II) and AFGL2591, G32.03+0.05N, and G25.40-0.14 (presented in SOMA IV). Examining their SOFIA-FORCAST images we note that these tend to be relatively isolated protostars.

However, we also caution that the above result may be influenced by methodological differences in how flux estimation and SED fitting is done in crowded regions. As described above, our method of defining source apertures in crowded regions is limited by the presence of neighboring sources. This could cause a systematic underestimation in flux (both via limiting the area and by overestimating the background), and thus mass, of the most massive sources. On the other hand, we note that it seems likely that in some of the SOMA V regions we are actually overestimating fluxes since we cannot resolve sources that are closer than $10''$ apart, e.g., in G58.77+00.65. To more definitely establish if there is an environmental dependence of maximum protostellar mass will require independent measurements of mass, e.g., dynamical mass measurements via studies of accretion disk kinematics.

6. SUMMARY AND CONCLUSIONS

In this paper, the fifth in the SOFIA Massive (SOMA) Star Formation Survey, we have analyzed 34 protostar candidates in 7 regions of relatively clustered massive star formation. We have also presented version 2.0 of **sedcreator**, a Python package designed to facilitate the flux measurement and SED fitting process that was introduced by Fedriani et al. (2023) (SOMA Paper IV). In this new version of the package, we introduce a source detection method using the dendrogram algorithm on median-filtered $37 \mu\text{m}$ images. We also present an updated tool to automatically determine the aperture radii of sources in isolated or crowded regions so that this process can be done efficiently and uniformly. In addition, we have updated the flux calculation process to account for the presence of neighboring sources. We have presented an improved method of defining “good” SED model fits, which improves results, especially for faint sources. We have also developed a method for empirical clump mass surface density estimation via graybody fitting, which can then be used for “restricted SED fitting”. Here we summarize our main findings:

1. The SEDs of these 34 sources are generally well fit with the ZT18 models. We report the averaged properties of “good” model fits and their associated dispersions to account for the degeneracies present in the SED fitting process.
2. These sources span a wide range of environments and properties. After fitting the SEDs with the ZT18 RT models, we estimate initial core masses spanning $M_c \sim 30 - 200 M_{\odot}$, clump mass surface densities spanning the entire model grid range from $\Sigma_{\text{cl}} \sim 0.1 - 3 \text{ g cm}^{-2}$, and current protostellar masses from $m_* \sim 4 - 40 M_{\odot}$.
3. The distribution of SOMA protostars in the m_* versus Σ_{cl} plane provides insight into the conditions required for massive star formation to occur. Consistent with the SOMA I-IV results, massive protostars in the SOMA V sample appear to cover the entire sampled range of Σ_{cl} , which is inconsistent with the prediction that massive stars require a minimum of $\Sigma_{\text{cl}} \sim 1 \text{ g cm}^{-2}$ to form. In addition to doubling the number of massive protostars forming in low- Σ_{cl} environments, SOMA V also shows that this trend continues to hold in crowded regions.
4. We note tentative evidence for an environmental dependence on the initial mass function of stars at the high-mass end, i.e., the most massive stars (\gtrsim

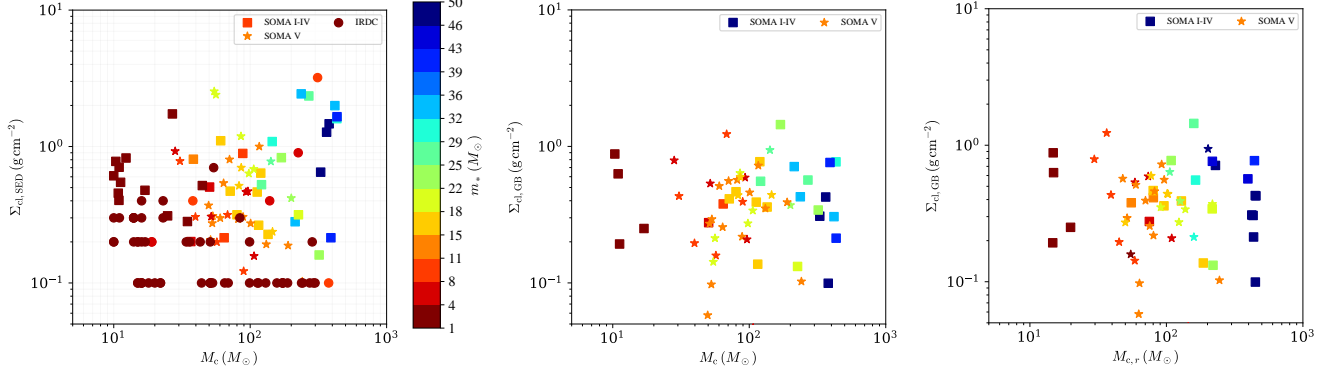


Figure 10. (a) *Left panel:* Mass surface density of the clump environment (Σ_{cl}) versus initial mass of the core (M_c) for SOMA I-V sources and the IRDC samples. Each data point is the average of good model fits. Each point is also color-coded with the current mass of the protostar (m_*). (b) *Middle panel:* Same as (a), but Σ_{cl} values are derived from the graybody fitting for the 60 SOMA I-V sources with available Herschel 70-500 μm data (see text). (c) *Right panel:* As (b), but M_c and m_* have been calculated with restricted SED fitting, i.e., using only models with a Σ_{cl} closest to the graybody fitting-derived value.

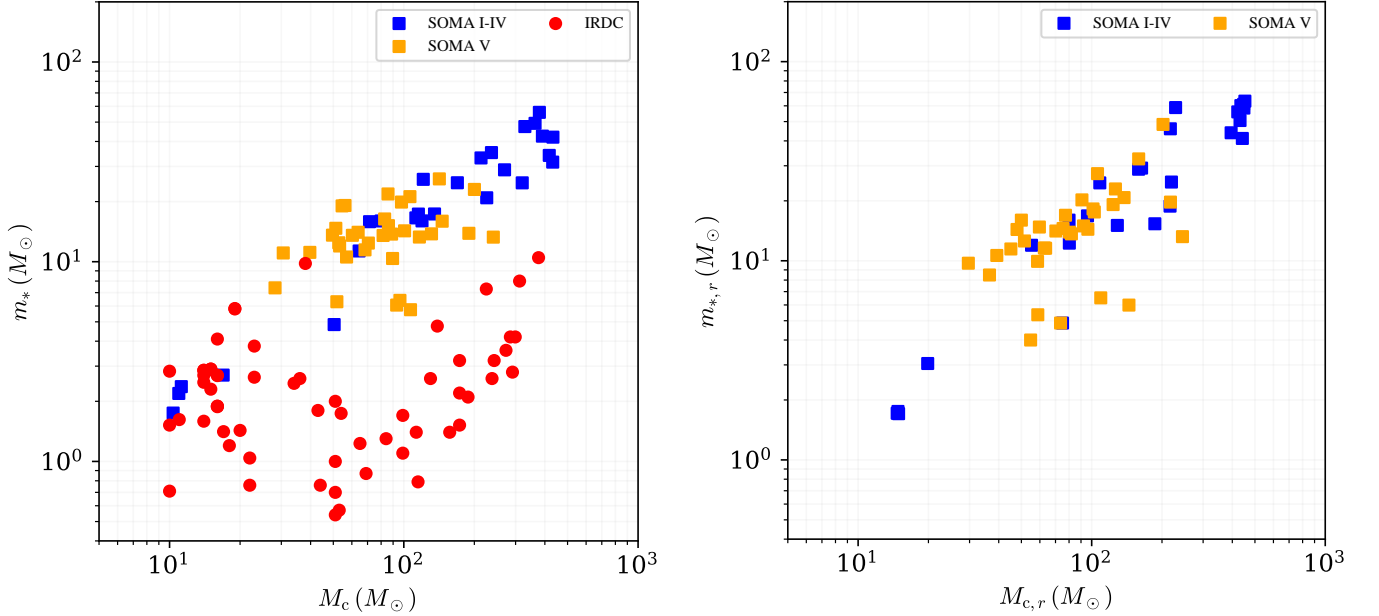


Figure 11. (a) *Left panel:* Current protostellar mass (m_*) versus initial core mass (M_c) for SOMA I-V sources and the IRDC samples. Each data point is the average of good model fits. (b) *Right panel:* Same as (a), but M_c and m_* have been calculated with restricted SED fitting, i.e., using only models with a Σ_{cl} closest to the graybody fitting-derived value.

$30M_\odot$) do not appear to form in the most clustered environments. However, further investigation of this result is needed, likely requiring independent, dynamical estimates of protostellar masses.

Acknowledgements: R.F. acknowledges support from the grants Juan de la Cierva FJC2021-046802-I, PID2020-114461GB-I00, PID2023-146295NB-I00, and from the Severo Ochoa grant CEX2021-001131-S funded by

MCIN/AEI/ 10.13039/501100011033 and by “European Union NextGenerationEU/PRTR”. J.C.T. acknowledges support from USRA-SOFIA grant 09_0085, NSF grants AST-2009674 and AST-2206450, ERC Advanced Grant 788829 (MSTAR), and the CCA Sabbatical Visiting Researcher program. G.C. acknowledges support from the ESO Fellowship Program and funding from the Swedish Research Council (VR Grant; Project: 2021-05589).

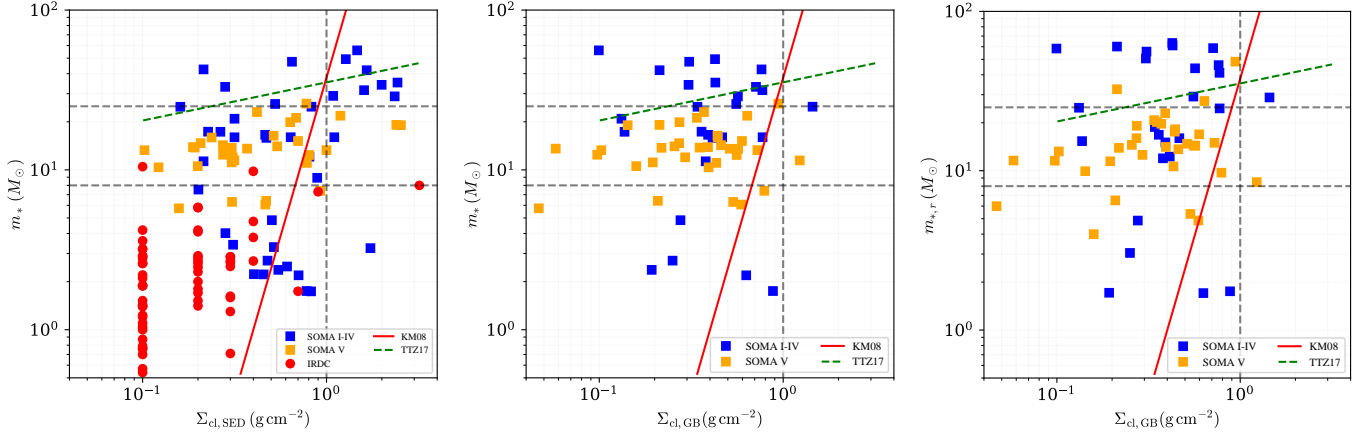


Figure 12. (a) *Left panel:* Current protostellar mass (m_*) versus clump environment mass surface density (Σ_{cl}) for the SOMA I-V sources and IRDC protostars (see the text). Lines indicating reference values of $m_* = 8$ and $25 M_\odot$ and $\Sigma_{\text{cl}} = 1 \text{ g cm}^{-2}$ (see the text) are highlighted. The red solid line shows the fiducial prediction of Krumholz & McKee (2008) (assuming their parameter values of $\delta = 1$ and $T_b = 10 \text{ K}$) for the minimum Σ_{cl} needed to form a star of given mass m_* . The green-dashed line shows the results for the final stellar mass formed from $100 M_\odot$ prestellar cores as a function of Σ_{cl} (Tanaka et al. 2017). (b) *Middle panel:* m_* versus Σ_{cl} derived from the graybody fitting for the 60 SOMA I-V sources with available Herschel 70-500 μm data (see the text). (c) *Right panel:* As (b), but m_* has been calculated using only models with a Σ_{cl} closest to the graybody fitting-derived value.

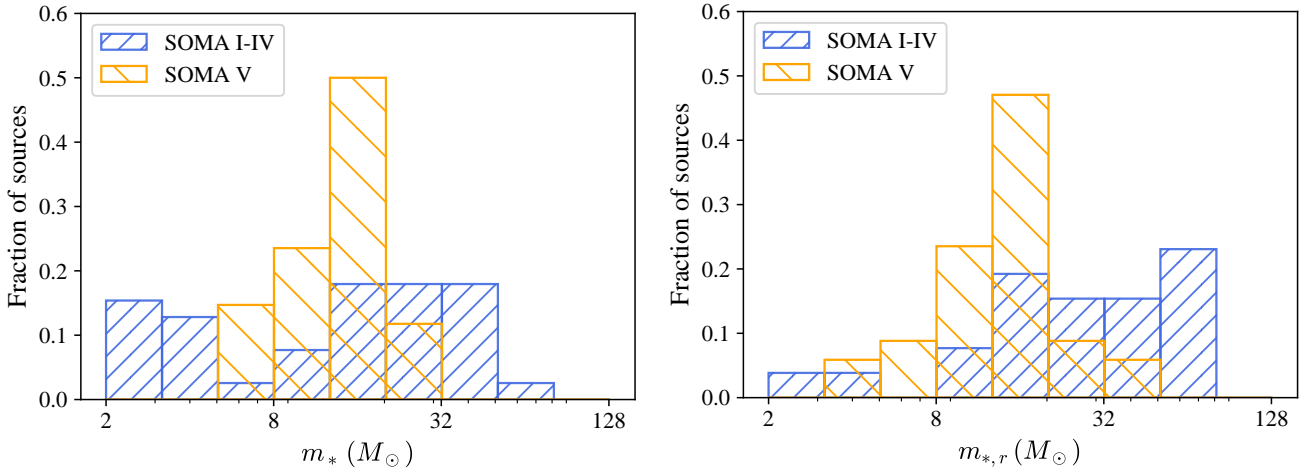


Figure 13. (a) *Left panel:* Current protostellar mass (m_*) distribution for SOMA I-IV sources (blue) and SOMA V sources (orange). (b) *Right panel:* As (a), but for restricted SED fitting, i.e., only considering models with a Σ_{cl} closest to the graybody-derived value.

A. TESTING GRAYBODY Σ MEASUREMENTS

Here we apply the graybody fitting method described in Section 3 to the ZT18 grid of radiative transfer models to derive $\Sigma_{\text{c,env,GB}}$, i.e., the mass surface density of the protostellar core envelope, which can then be compared with the actual value of the model. To accomplish this, we first constructed an SED of the predicted fluxes at the Herschel 70, 160, 250, 350, and 500 μm bands for each model in the grid. We then fit the graybody distribution given in Section 3 to each of these SEDs to derive a corresponding $\Sigma_{\text{c,env,GB}}$ value. Next, we repeated this process, but excluded the 70 μm data from the graybody fitting. We then computed the actual $\Sigma_{\text{c,env}}$ for the protostellar cores defined by the remaining envelope mass ($M_{\text{c,env}}$) for each of the models via:

$$\Sigma_{\text{c,env}} = M_{\text{c,env}} / (\pi R_c^2), \quad (\text{A1})$$

where R_c is the radius of the core. Figure A1 shows the results of this comparison when the $70\mu\text{m}$ data is included (a) and excluded (b). From this figure, we can see that including the $70\mu\text{m}$ data leads to better agreement between $\Sigma_{\text{c,env,GB}}$ and $\Sigma_{\text{c,env}}$. In particular, there is less scatter in the derived values of $\Sigma_{\text{c,env,GB}}$ for a given input $\Sigma_{\text{c,env}}$. However, we do note a systematic trend for $\Sigma_{\text{c,env,GB}}$ to overestimate the true value, especially for the highest mass surface densities. Nevertheless, we expect that the impact for interpretation of the SOMA sources of this effect is modest, since most values of $\Sigma_{\text{cl,GB}}$ are $\lesssim 1 \text{ g cm}^{-2}$.

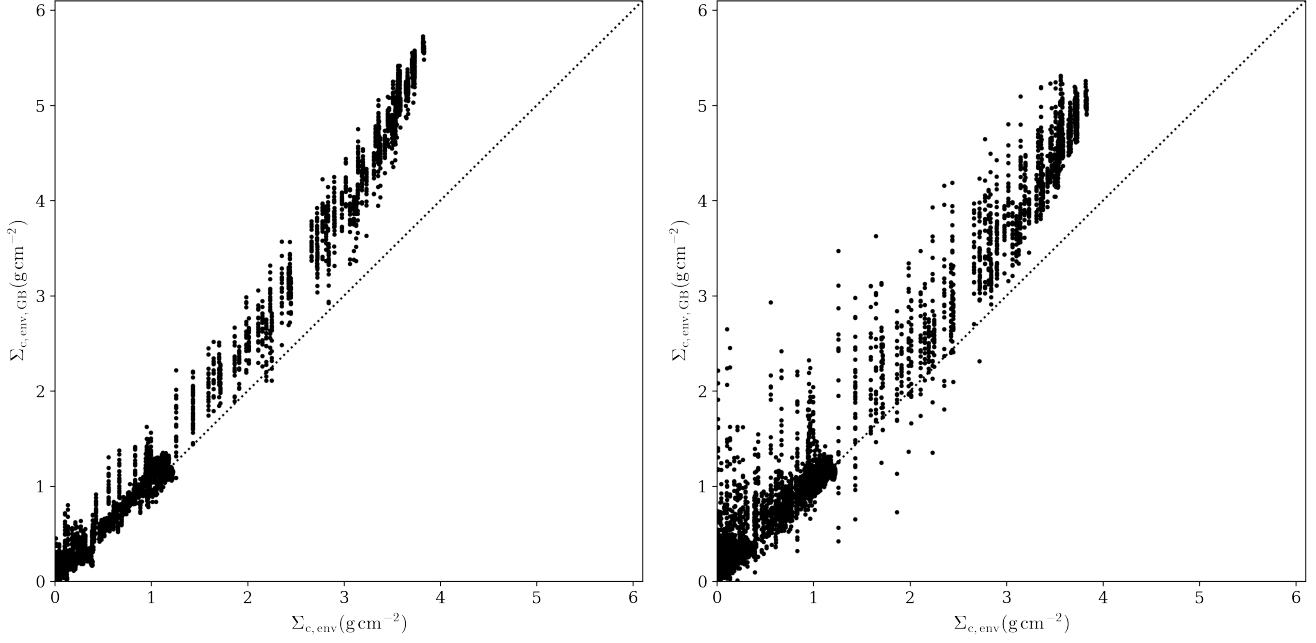


Figure A1. (a) *Left panel:* Clump environment mass surface density derived from graybody fitting to Herschel 70-500 μm background flux values ($\Sigma_{\text{c,env,GB}}$) vs. theoretical $\Sigma_{\text{c,env}}$ for the ZT18 grid of Radiative transfer models. (b) *Right panel:* As (a), but excluding the Herschel 70 μm data from the fitting.

B. SOMA V SED FITS

Here we present the results of the SED fitting for the 34 sources in the SOMA V sample obtained using Sedcreator (version 2.0). Tables B1 and B2 present the measured fluxes and best models. Figure A2 contains the source SEDs and “good” model fits (see main text for details), and Figure A3 presents the good model distributions in the $\Sigma_{\text{cl}} - M_c$, $m_* - M_c$, and $m_* - \Sigma_{\text{cl}}$ planes.

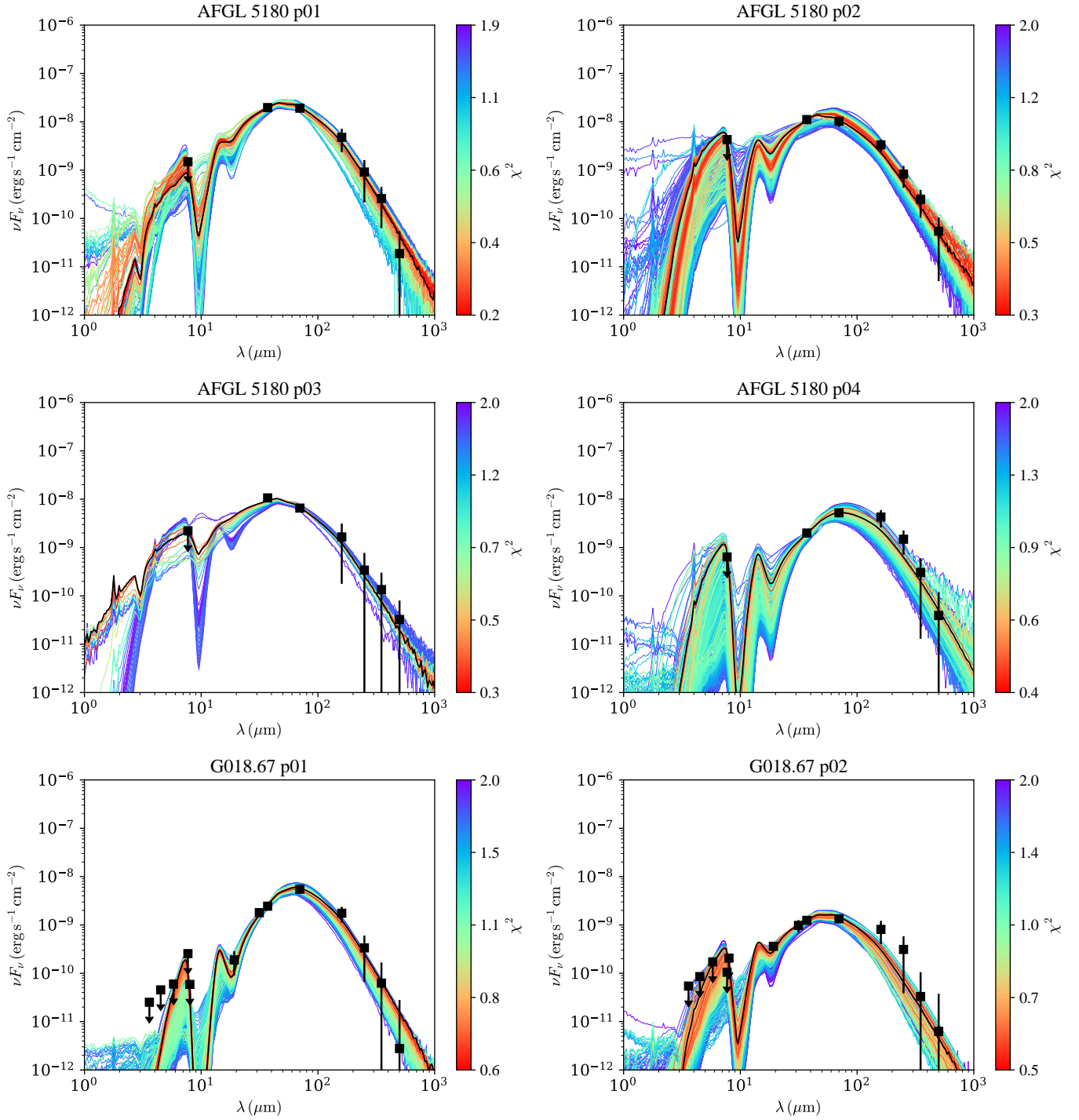


Figure A2. SOMA V sources analyzed with Sedcreator. Protostellar model fitting to the fixed aperture, background-subtracted SED data using the ZT18 model grid. For each source, the best fitting protostar model is shown with a black line, while all other “good” model fits (see text) are shown with colored lines (red to blue with increasing χ^2). Flux values are those from Table B1. Note that the data at $\lesssim 8 \mu\text{m}$ are treated as upper limits (see text). The resulting model parameters are listed in Table B2.

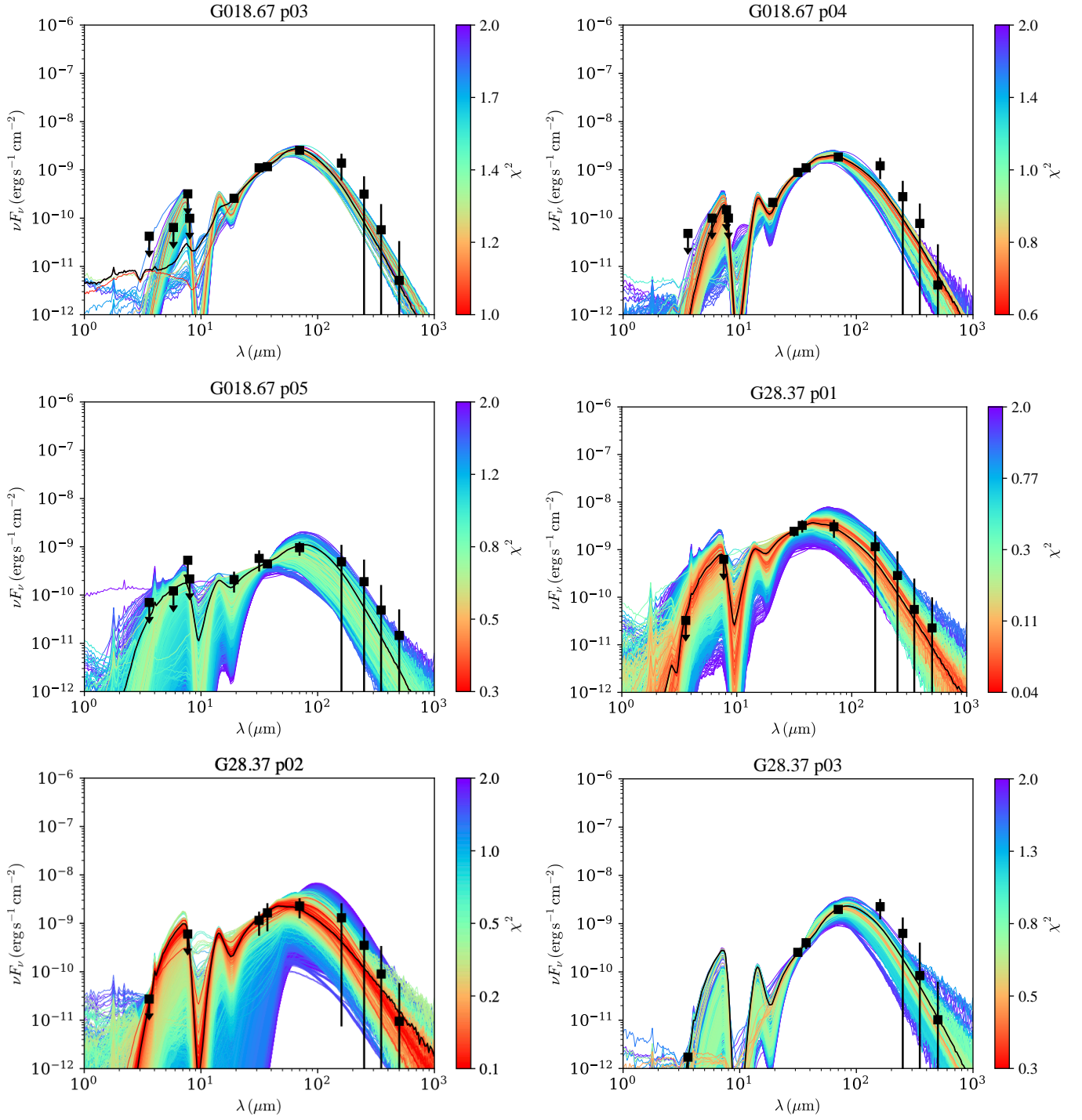


Figure A2. (Continued.)

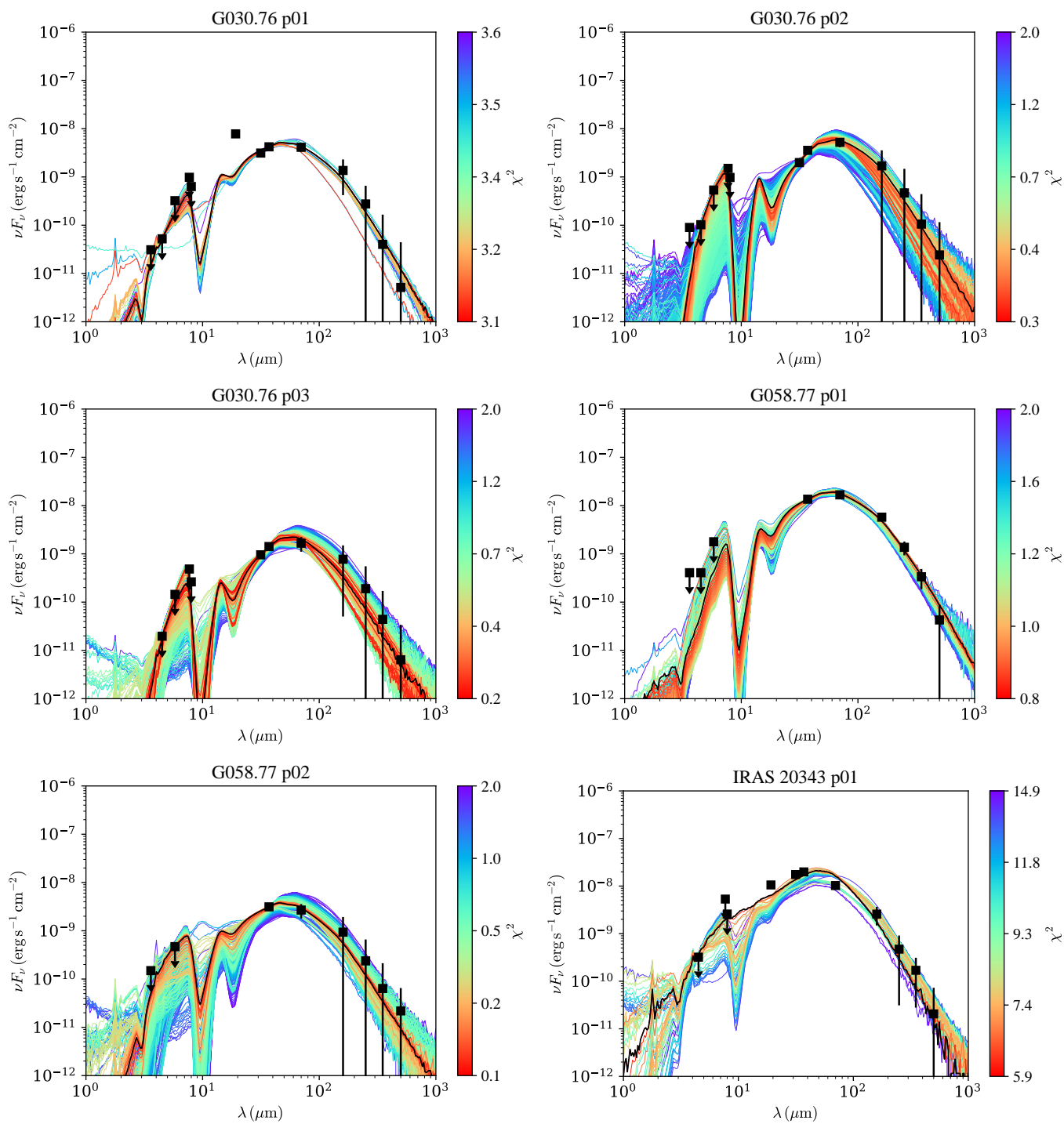


Figure A2. (Continued.)

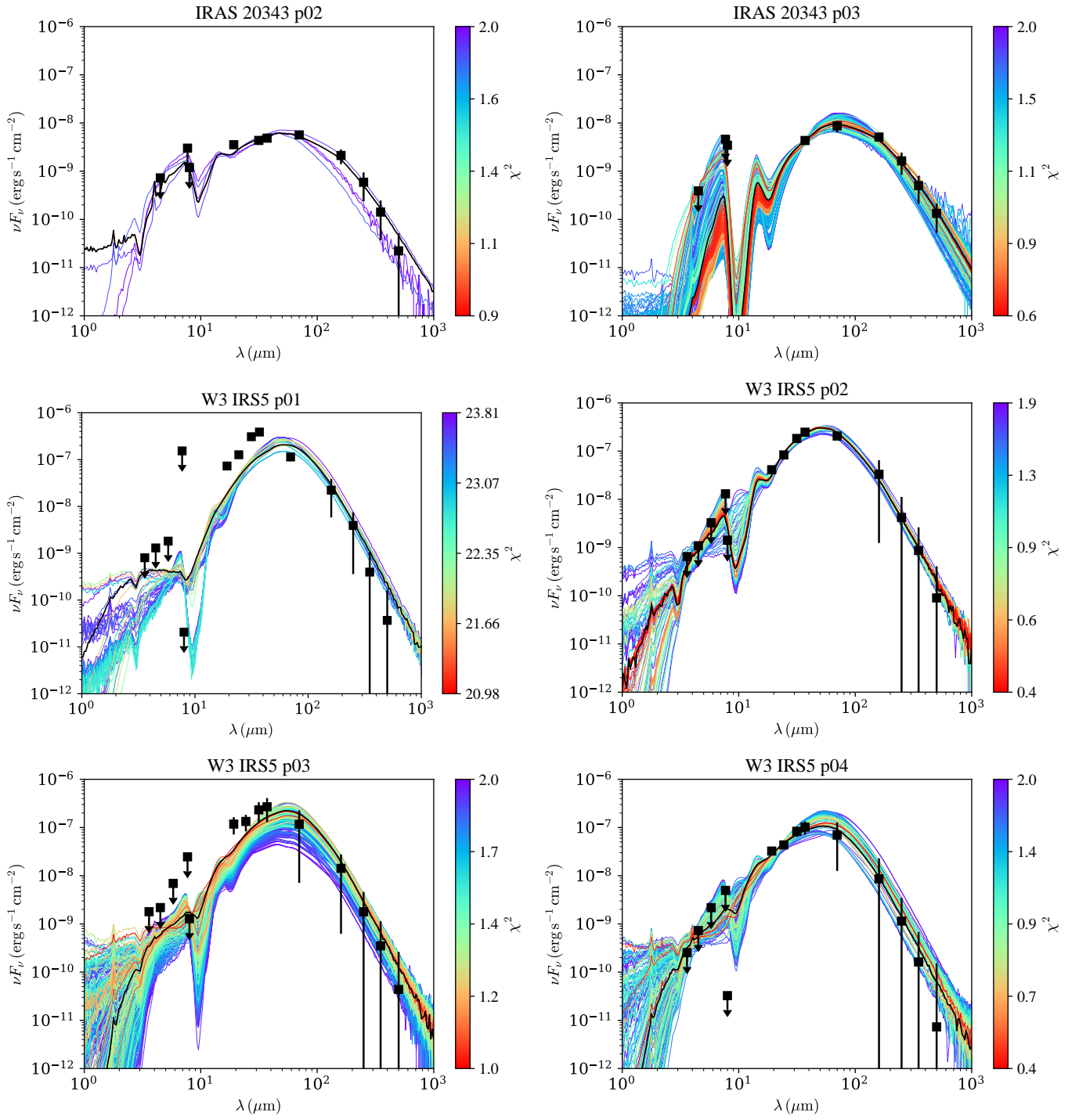


Figure A2. (Continued.)

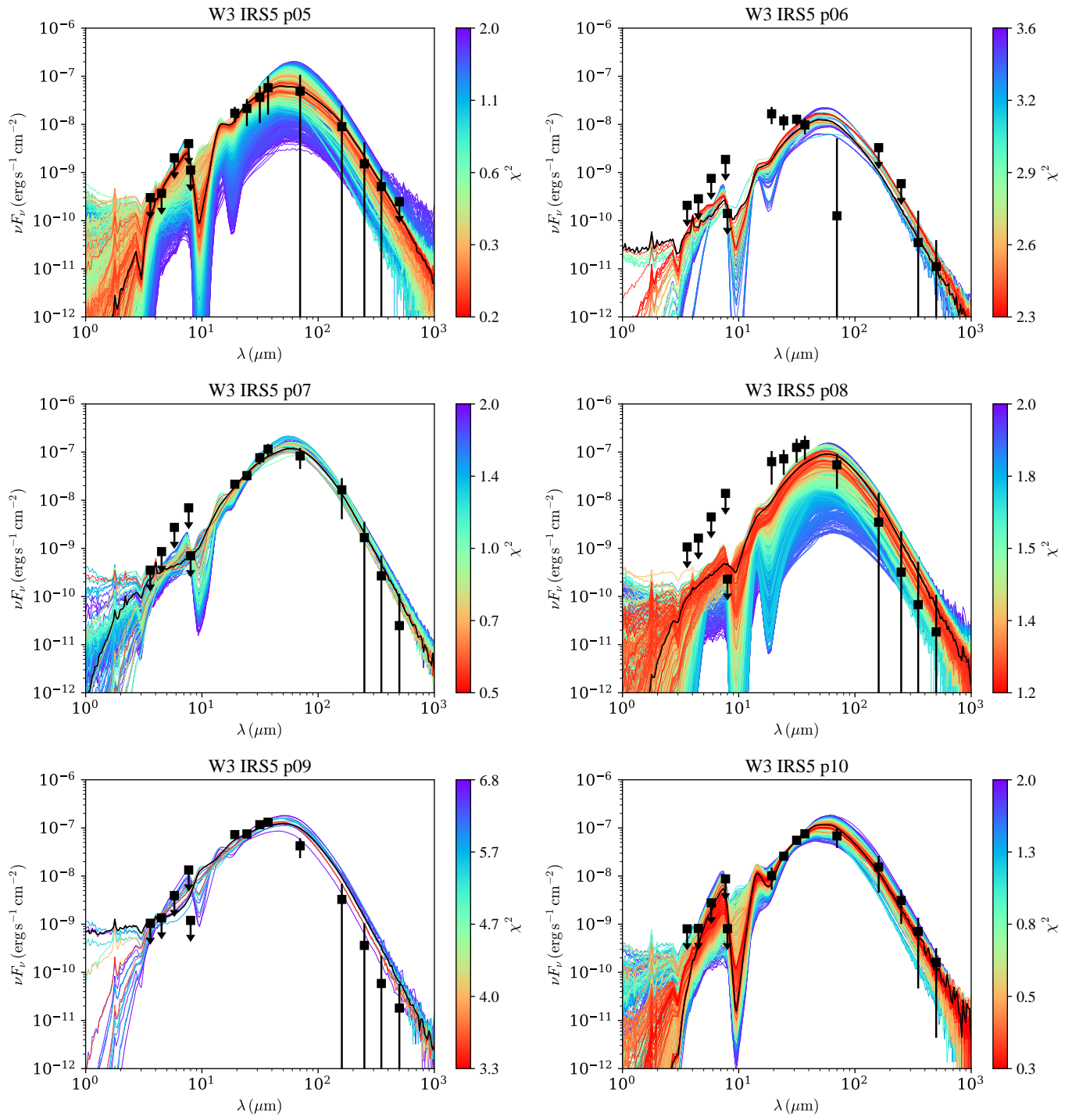


Figure A2. (Continued.)

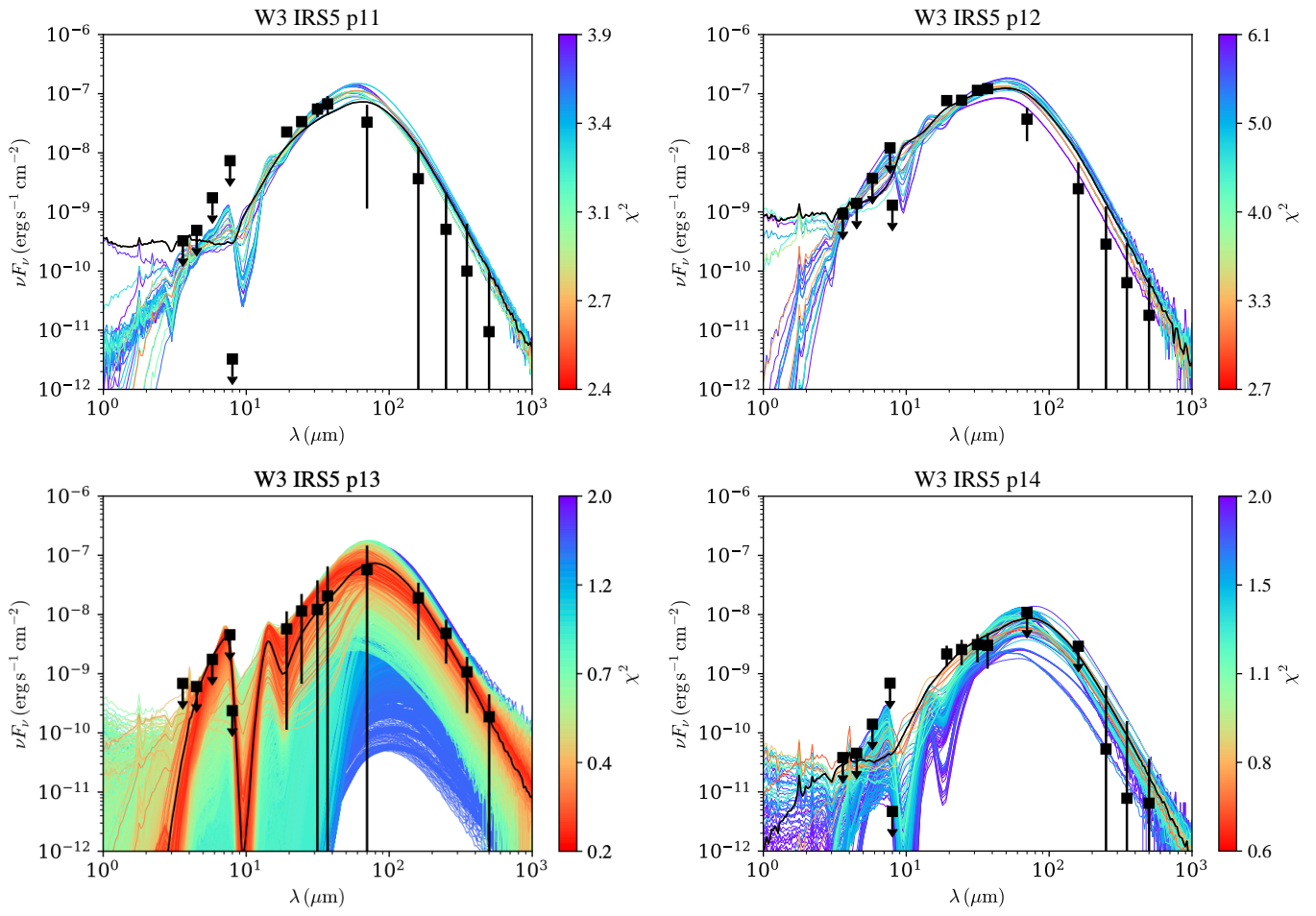
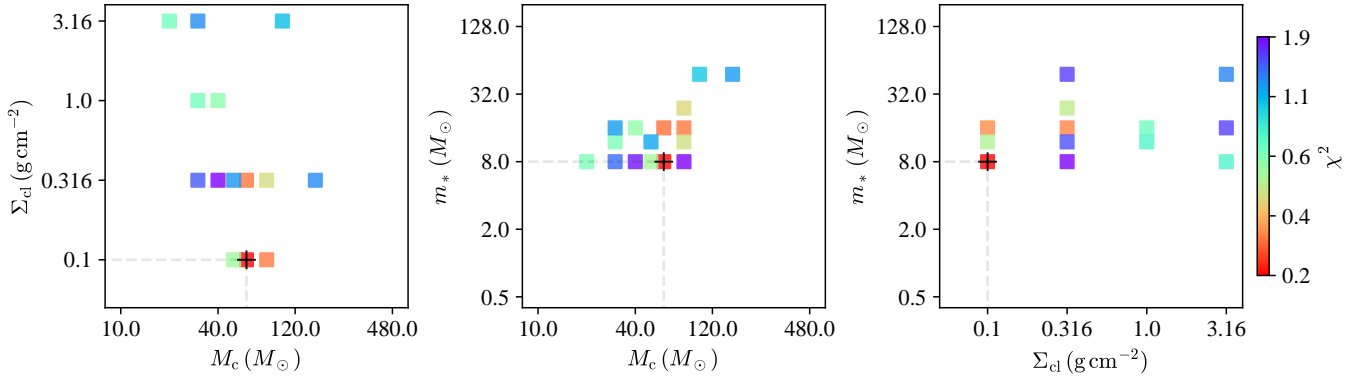
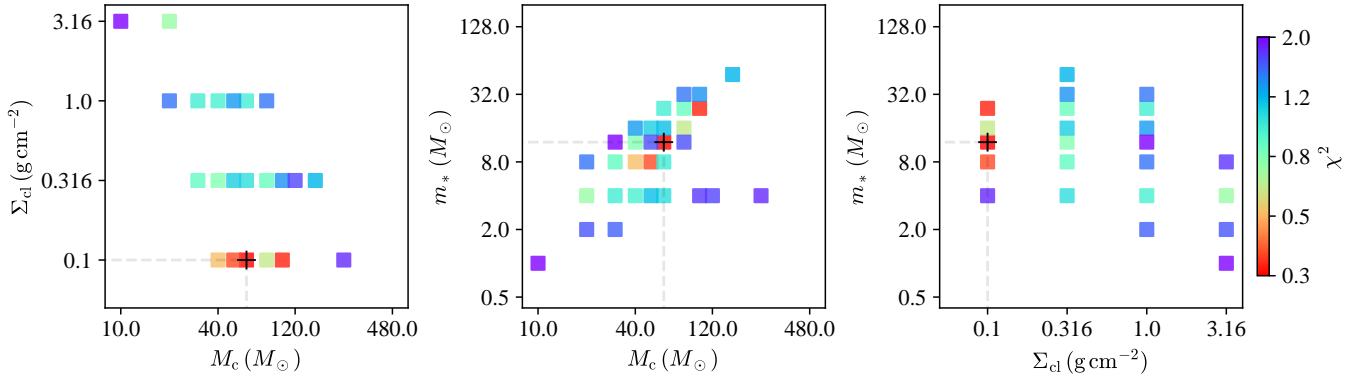


Figure A2. (Continued.)

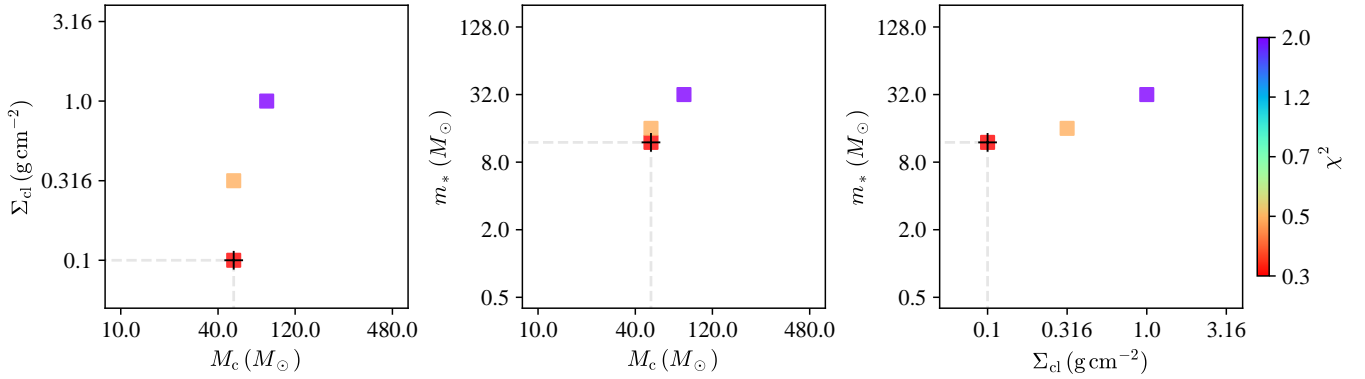
AFGL 5180 p01



AFGL 5180 p02



AFGL 5180 p03



AFGL 5180 p04

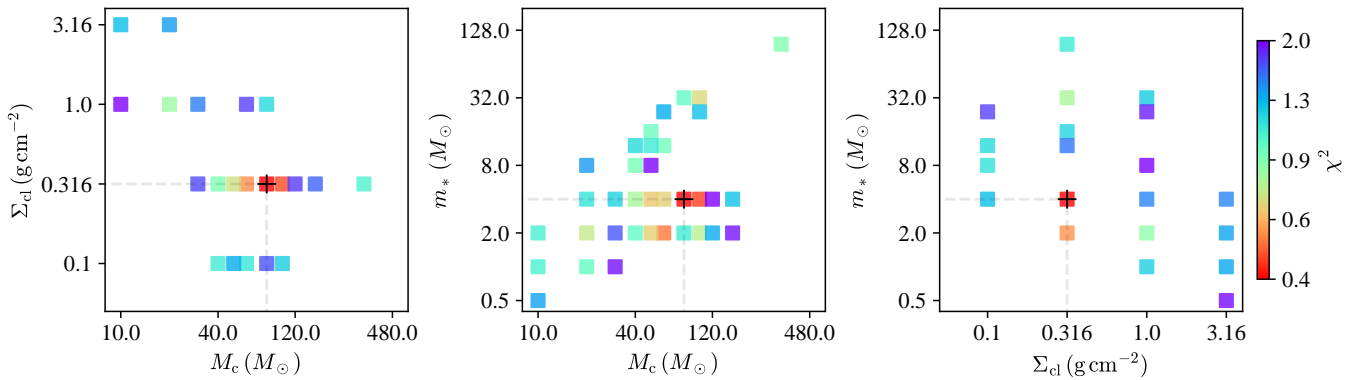


Figure A3. Σ_{cl} vs. M_c (left column), m_* vs. M_c (center column), and m_* vs. Σ_{cl} (right column) for the “good” model fits for each source, color-coded by χ^2 value. The black cross distinguishes the best-fit model.

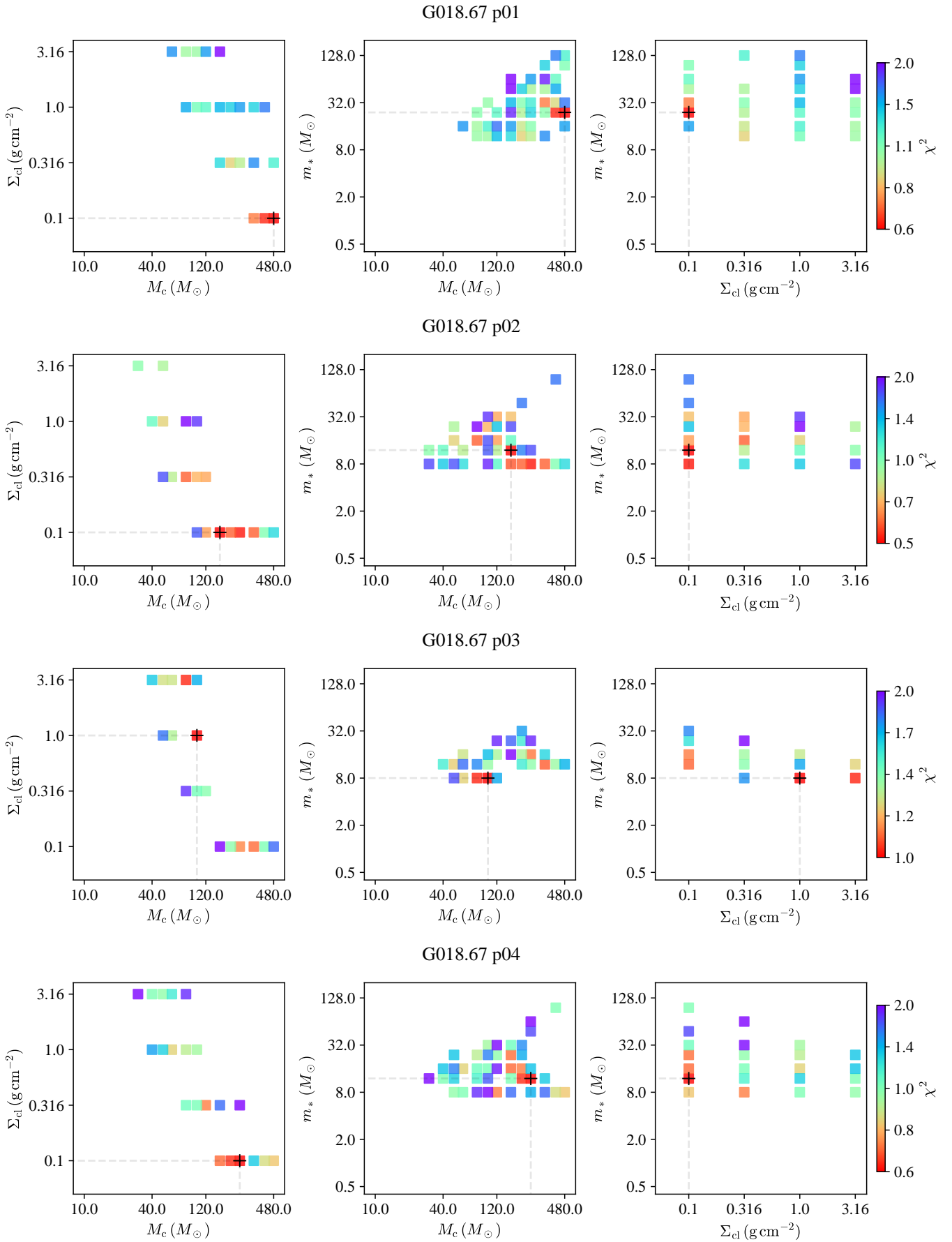
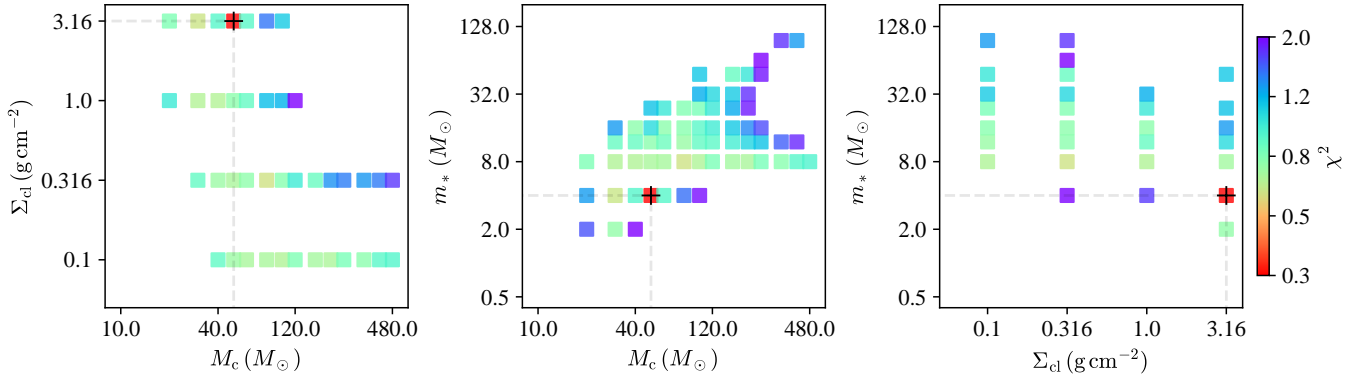
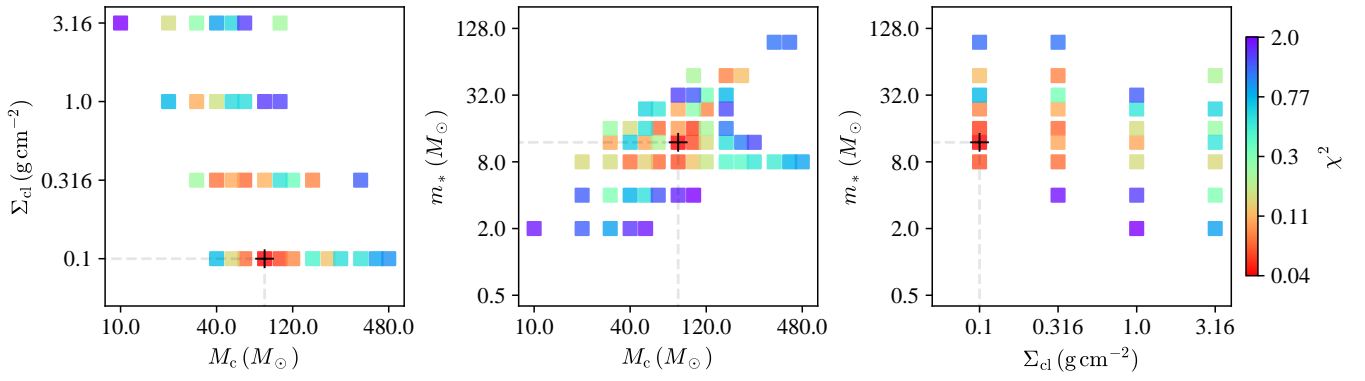


Figure A3. (Continued.)

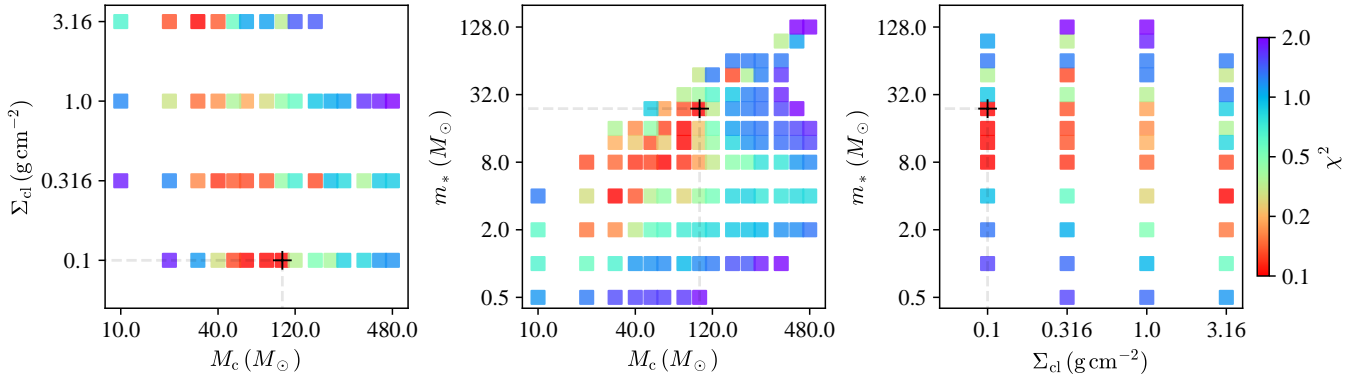
G018.67 p05



G28.37 p01



G28.37 p02



G030.76 p03

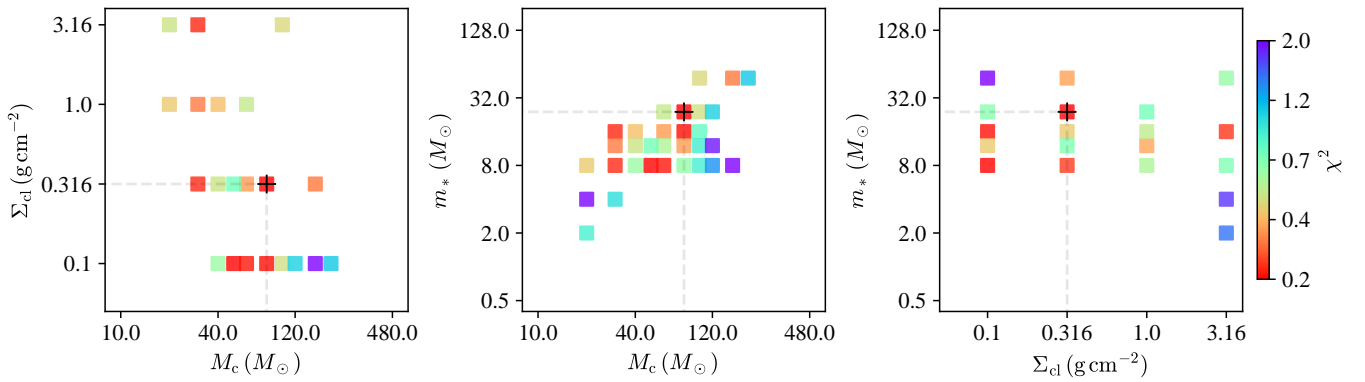
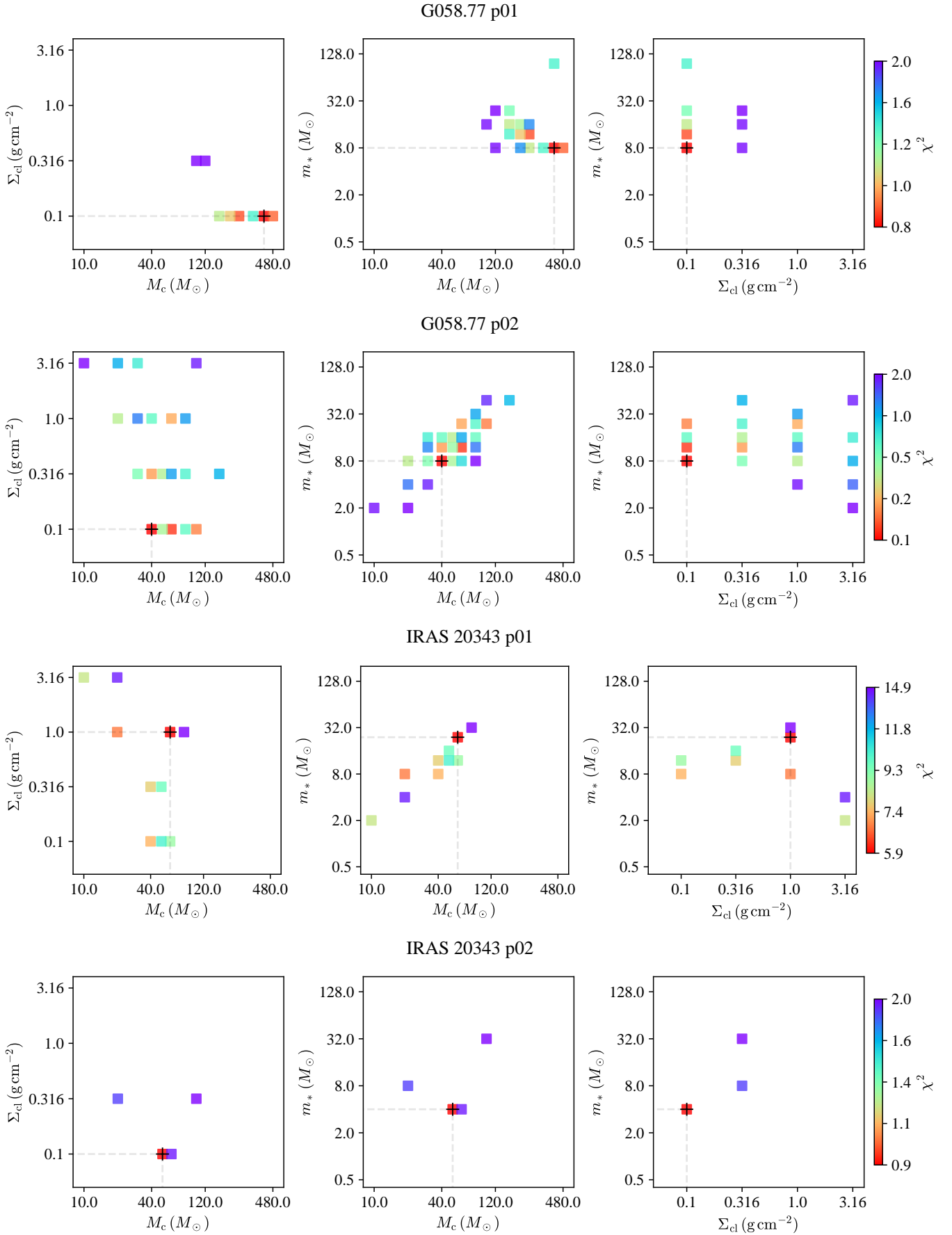
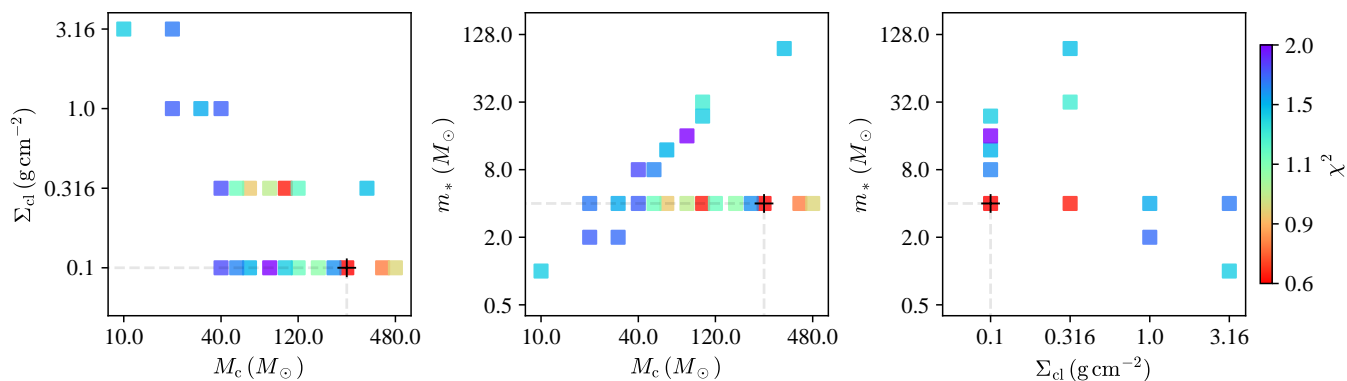


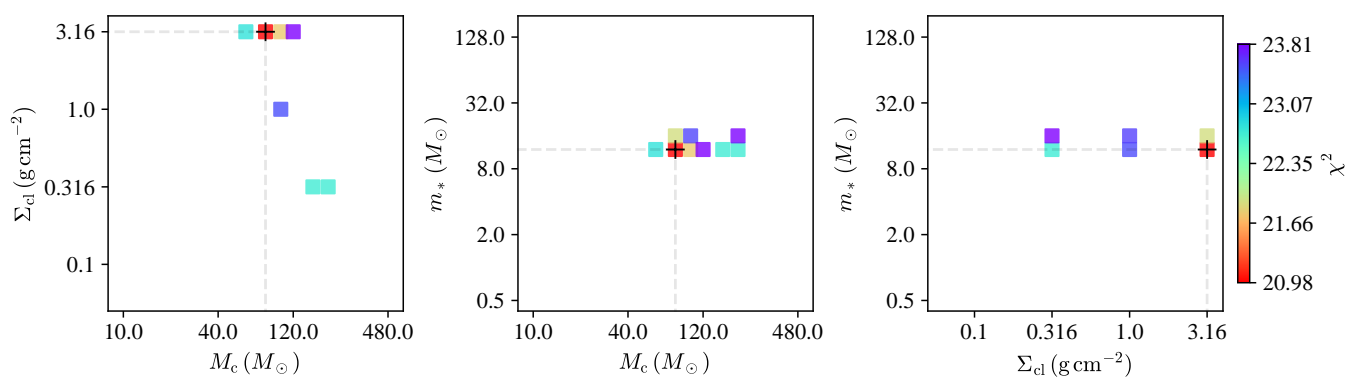
Figure A3. (Continued.)

**Figure A3.** (Continued.)

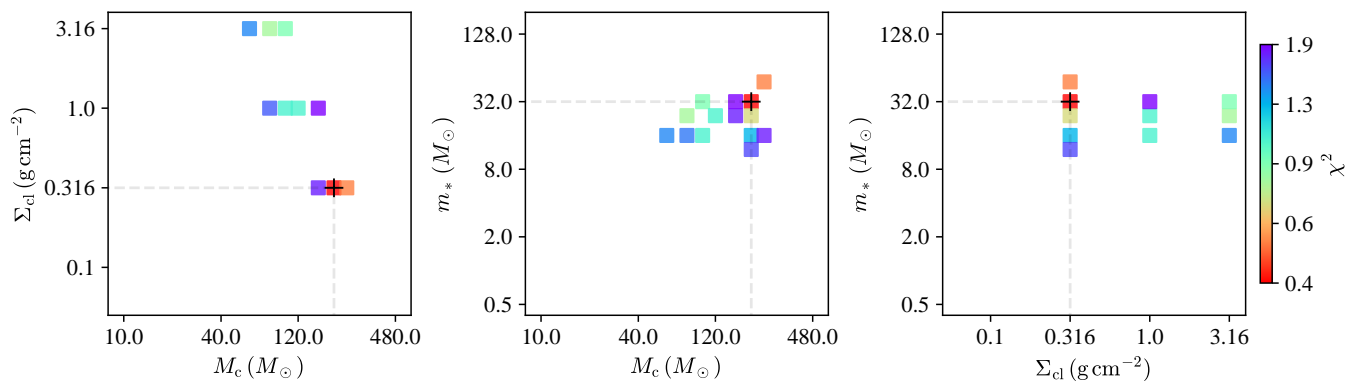
IRAS 20343 p03



W3 IRS5 p01



W3 IRS5 p02



W3 IRS5 p03

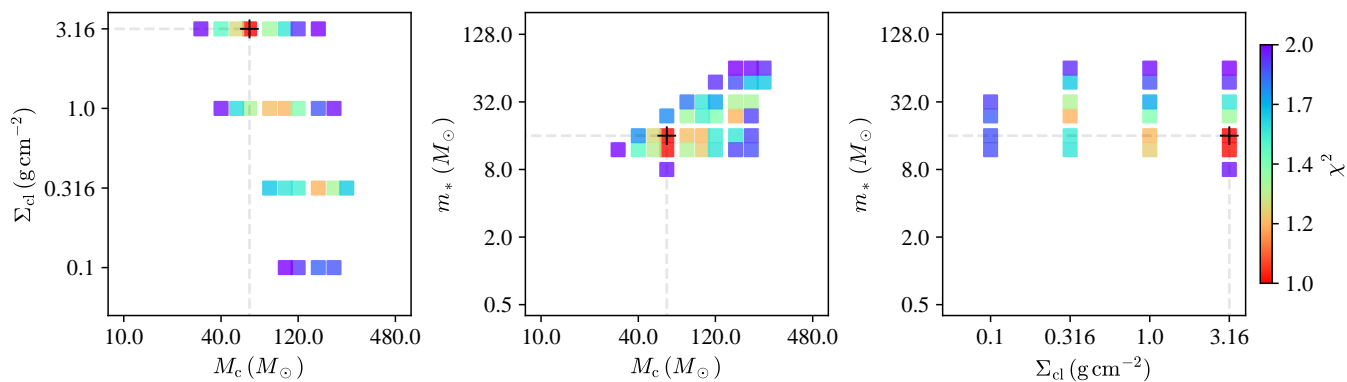


Figure A3. (Continued.)

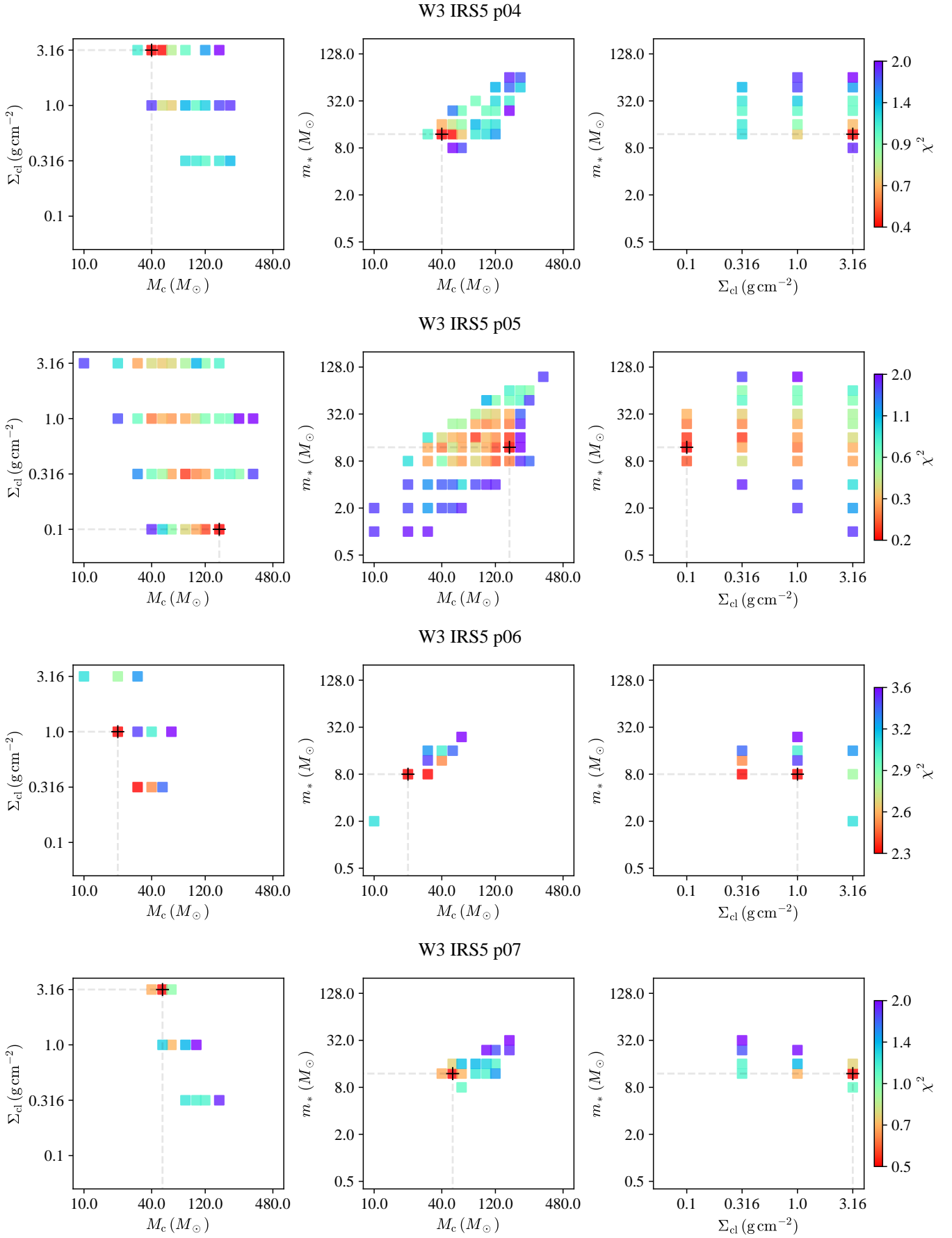


Figure A3. (Continued.)

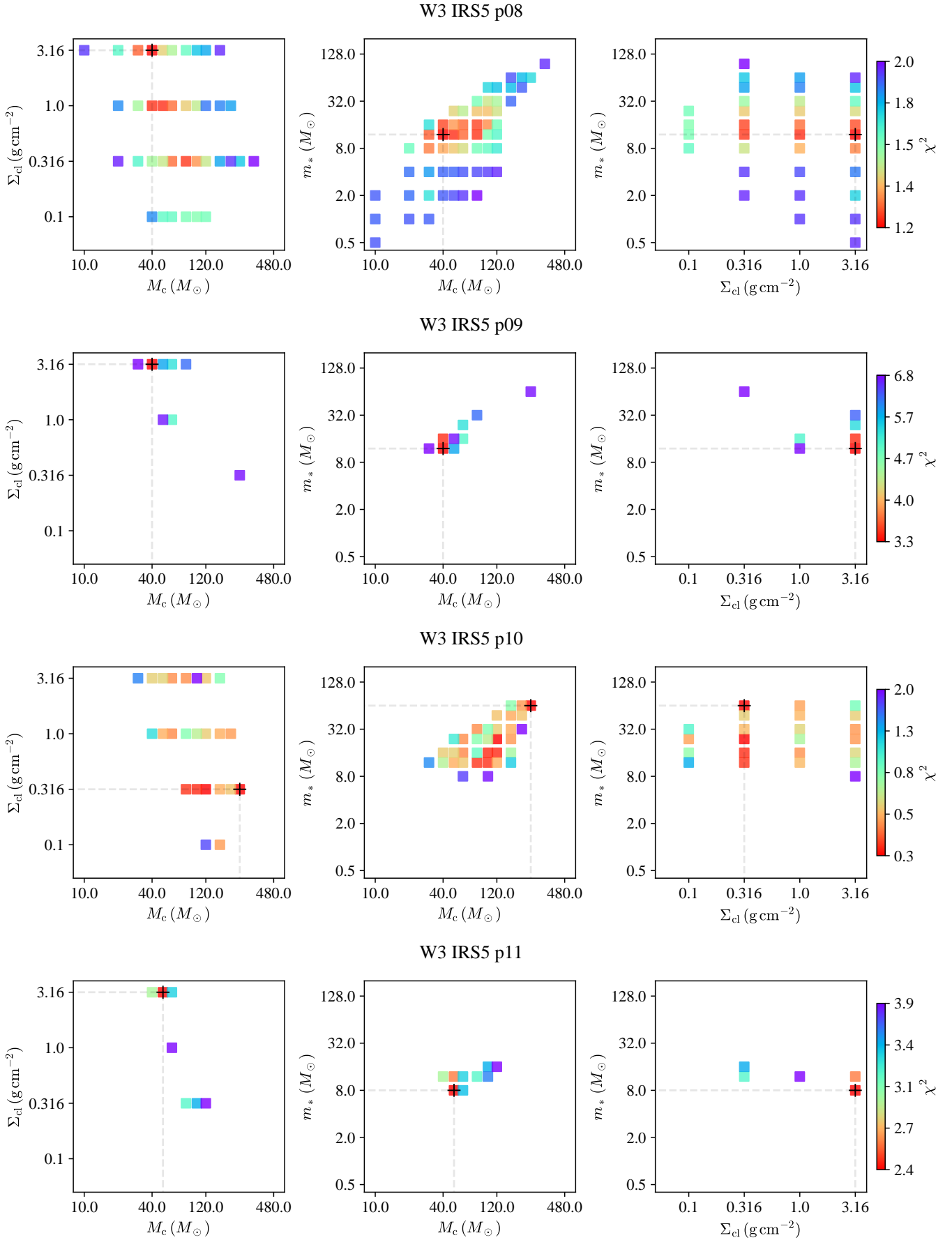


Figure A3. (Continued.)

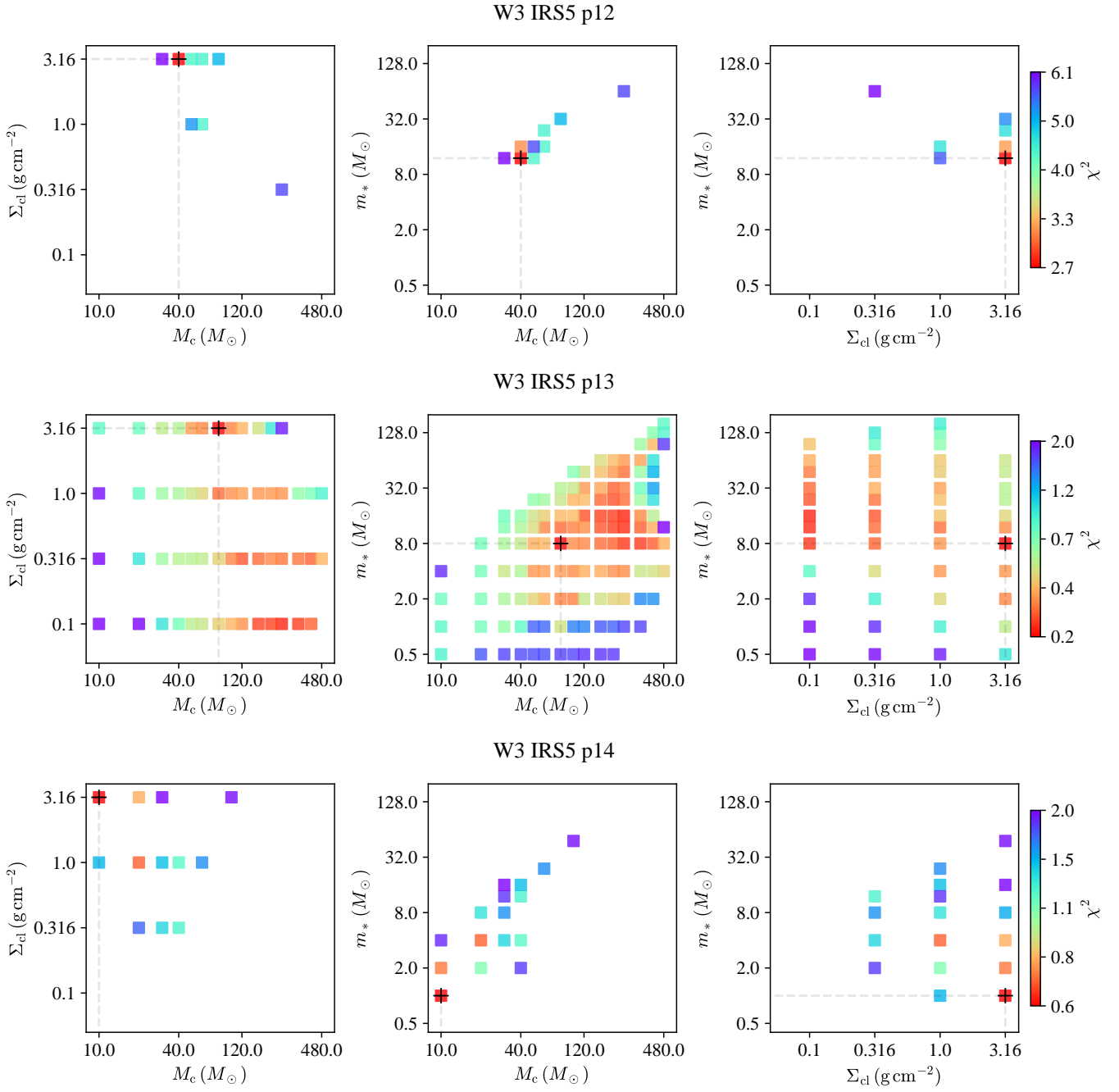
**Figure A3.** (Continued.)

Table B1. Integrated Flux Densities

Source	radius ($''$ /pc)	$F_{3.6}$	$F_{4.5}$	$F_{5.8}$	$F_{7.7}$	$F_{8.0}$	$F_{19.7}$	$F_{24.2}$	$F_{31.5}$	$F_{37.1}$	F_{70}	F_{160}	F_{250}	F_{350}	F_{500}
AFGL5180 p01	12.25	3.82	243.65	446.14	254.15	76.21	30.08	3.13
	0.10	(3.14)	(248.27)	(518.46)	(379.70)	(52.59)	(52.59)	(9.16)
AFGL5180 p02	24.25	11.00	137.41	239.83	177.59	68.96	28.90	9.11
	0.21	(9.06)	(133.23)	(253.28)	(223.10)	(101.28)	(45.48)	(17.32)
AFGL5180 p03	12.25	5.69	131.63	152.94	88.38	28.41	15.77	5.41
	0.10	(6.62)	(144.09)	(206.44)	(166.81)	(64.48)	(35.20)	(13.31)
AFGL5180 p04	14.75	1.64	24.66	121.80	228.09	123.79	35.70	6.55
	0.13	(0.59)	(27.51)	(138.60)	(315.10)	(187.23)	(69.69)	(19.91)
G18.67 p01	10.0	0.03	0.07	0.12	0.65	0.16	1.21	...	18.88	30.24	128.12	93.32	27.98	7.31	0.46
	0.52	(0.08)	(0.10)	(0.34)	(0.76)	(1.75)	(19.80)	(30.18)	(135.33)	(125.33)	(19.48)	(19.48)	(4.66)
G18.67 p02	10.5	0.07	0.13	0.33	0.27	0.55	2.31	...	10.26	15.40	31.34	43.12	25.95	3.85	1.05
	0.55	(0.12)	(0.15)	(0.53)	(2.07)	(1.06)	(2.57)	...	(4.75)	(12.56)	(36.05)	(64.48)	(48.54)	(12.30)	(6.26)
G18.67 p03	11.75	0.05	...	0.12	0.82	0.26	1.65	...	11.61	14.41	59.36	73.80	26.24	6.70	0.86
	0.62	(0.12)	...	(0.40)	(0.89)	(1.00)	(2.01)	...	(11.16)	(12.98)	(66.62)	(114.92)	(61.36)	(22.85)	(5.59)
G18.67 p04	10.25	0.06	...	0.19	0.38	0.27	1.36	...	9.30	13.67	43.04	64.84	23.24	9.07	0.69
	0.54	(0.11)	...	(0.40)	(0.83)	(0.82)	(1.75)	...	(7.28)	(11.64)	(48.13)	(94.72)	(49.33)	(23.44)	(4.80)
G18.67 p05	15.25	0.08	...	0.24	1.35	0.57	1.34	...	6.04	5.47	22.38	26.04	15.77	5.70	2.43
	0.80	(0.18)	...	(0.64)	(0.70)	(1.68)	(2.87)	...	(3.07)	(4.64)	(29.55)	(58.40)	(45.18)	(18.82)	(8.41)
G28.37 p01	12.5	0.04	1.61	25.53	39.92	70.49	61.57	23.85	6.46	3.77
	0.30	(0.06)	(2.51)	(27.09)	(45.40)	(86.03)	(129.25)	(76.90)	(28.73)	(16.58)
G28.37 p02	10.75	0.03	1.55	12.10	20.40	53.24	69.57	29.33	10.52	1.58
	0.26	(0.04)	(1.96)	(13.46)	(24.01)	(73.04)	(138.39)	(70.04)	(39.80)	(9.72)
G28.37 p03	9.75	0.25	2.67	4.97	46.02	119.88	52.32	9.79	1.70
	0.24	(0.01)	(-0.08)	(3.12)	(5.72)	(52.30)	(172.84)	(111.83)	(47.33)	(10.42)
G30.76 p01	10.25	0.04	0.08	0.62	2.53	1.69	49.97	...	32.85	52.09	96.08	72.73	23.02	4.69	0.86
	0.24	(0.06)	(0.10)	(0.82)	(2.55)	(2.35)	(16.26)	...	(33.55)	(54.13)	(116.63)	(122.50)	(54.74)	(19.34)	(7.41)
G30.76 p02	17.0	0.11	0.15	1.04	3.86	2.60	-31.60	...	20.84	43.99	121.83	90.36	38.95	12.33	4.04
	0.40	(0.16)	(0.20)	(1.57)	(3.53)	(4.43)	(-100.90)	...	(21.31)	(42.75)	(144.56)	(189.32)	(122.64)	(51.49)	(19.30)
G30.76 p03	9.5	...	0.03	0.28	1.25	0.70	17.91	...	3.01	[5.97]	[25.81]	[99.37]	[83.79]	[39.18]	[15.26]
	0.23	...	(0.05)	(0.45)	(1.09)	(1.28)	(-1.05)	...	(10.54)	(18.89)	(46.66)	(79.68)	(46.09)	(19.87)	(5.67)
		...	[0.01]	[0.09]	[0.21]	[0.24]	[14.19]	...	[1.64]	[2.44]	[12.94]	[38.61]	[30.28]	[14.75]	[4.60]

Table B1 continued

Table B1 (continued)

Source	radius ($''$ /pc)	$F_{3.6}$	$F_{4.5}$	$F_{5.8}$	$F_{7.7}$	$F_{8.0}$	$F_{19.7}$	$F_{24.2}$	$F_{31.5}$	$F_{37.1}$	F_{70}	F_{160}	F_{250}	F_{350}	F_{500}
G58.77 p01	21.5	0.49 (0.55)	0.61 (0.66)	3.45 (3.78)	167.81 (167.02)	389.55 (414.15)	307.17 (358.04)	113.96 (148.37)	39.17 (56.25)	7.14 (14.84)
	0.34	[0.07]	[0.07]	[0.47]	[17.92]	[59.43]	[36.24]	[17.52]	[7.74]	[7.74]
G58.77 p02	26.75	0.18 (0.30)	...	0.91 (1.65)	38.70 (37.56)	62.72 (102.72)	49.93 (24.80)	19.83 (65.02)	7.44 (24.80)	3.65 (10.84)
	0.43	[0.04]	...	[0.23]	[5.90]	[20.77]	[53.03]	[35.25]	[17.38]	[7.20]
IRAS20343 p01	15.5	...	0.48 (0.56)	...	13.69 (14.35)	6.91 (8.45)	67.65 (65.35)	183.59 (177.81)	245.86 (254.91)	137.45 (194.00)	39.38 (75.95)	19.82 (36.27)	3.44 (12.13)
	0.11	...	[0.05]	...	[1.46]	[0.78]	[6.79]	[18.40]	[24.36]	[58.20]	[36.79]	[16.57]	[8.70]
IRAS20343 p02	14.5	...	1.09 (1.16)	...	7.73 (7.83)	3.18 (4.25)	22.71 (18.80)	60.07 (64.15)	132.32 (149.90)	112.90 (149.26)	49.25 (78.15)	16.57 (28.70)	3.71 (8.55)
	0.10	...	[0.11]	...	[0.87]	[0.45]	[2.64]	[7.08]	[22.80]	[38.08]	[29.32]	[12.25]	[4.85]
IRAS20343 p03	40.5	...	0.59 (0.78)	...	11.82 (10.96)	9.22 (13.02)	11.03 (-12.09)	41.14 (-23.69)	53.73 (56.06)	273.21 (249.71)	136.57 (201.65)	58.76 (92.28)	22.27 (35.61)
	0.27	...	[0.14]	...	[1.18]	[2.81]	[8.33]	[4.92]	[5.37]	[54.17]	[66.50]	[34.04]	[13.52]
W3 p01	10.5	0.96 (1.37)	1.95 (2.97)	3.51 (9.55)	393.61 (401.79)	-2.57 (0.06)	467.06 (492.82)	1033.13 (1126.77)	3237.44 (3649.99)	4792.79 (4660.43)	2654.94 (2054.05)	1185.81 (2054.05)	326.79 (621.93)	46.21 (129.51)	6.15 (26.84)
	0.09	[0.12]	[0.24]	[1.04]	[39.50]	[0.30]	[53.79]	[113.18]	[347.98]	[518.20]	[504.09]	[876.30]	[296.94]	[83.42]	[20.69]
W3 p02	17.0	0.78 (1.10)	1.64 (1.83)	6.32 (9.05)	33.51 (33.04)	-0.14 (3.80)	263.91 (267.20)	680.52 (684.68)	1926.57 (3211.40)	3063.63 (3211.40)	4808.90 (6605.29)	1766.40 (3457.13)	352.29 (306.79)	101.58 (68.25)	15.05 (68.25)
	0.15	[0.33]	[0.25]	[2.80]	[3.38]	[3.94]	[26.60]	[98.18]	[198.16]	[340.14]	[517.22]	[1699.93]	[985.78]	[205.46]	[53.22]
W3 p03	18.75	2.15 (2.65)	3.28 (3.71)	13.40 (17.57)	63.33 (55.12)	3.42 (9.65)	754.30 (732.65)	1086.88 (1074.12)	2441.45 (2484.64)	3334.67 (3511.43)	2734.16 (4175.09)	149.14 (1476.72)	41.00 (386.17)	7.29 (132.19)	7.29 (43.89)
	0.17	[1.03]	[2.62]	[10.64]	[35.13]	[0.90]	[296.05]	[409.32]	[1077.12]	[1725.69]	[2568.12]	[723.69]	[237.50]	[91.28]	[36.60]
W3 p04	11.0	0.30 (0.66)	1.09 (1.52)	4.21 (7.56)	12.74 (15.49)	0.09 (2.92)	207.96 (220.92)	354.11 (398.95)	876.02 (1056.16)	1264.06 (1626.69)	1631.40 (291.06)	459.96 (1227.11)	95.69 (291.06)	18.96 (78.85)	1.22 (25.39)
	0.10	[0.36]	[0.44]	[3.38]	[3.03]	[2.84]	[24.50]	[57.14]	[200.28]	[384.03]	[1338.25]	[768.54]	[195.60]	[59.93]	[24.18]
W3 p05	17.5	0.36 (0.85)	0.55 (1.05)	3.91 (6.97)	10.26 (4.73)	3.00 (11.66)	109.31 (99.17)	174.81 (162.57)	384.39 (367.23)	716.16 (666.39)	1145.79 (2230.23)	478.86 (1297.69)	126.49 (353.01)	59.55 (136.26)	-1.61 (41.33)
	0.16	[0.23]	[0.42]	[2.86]	[8.55]	[1.02]	[39.14]	[99.91]	[272.38]	[519.28]	[1354.66]	[820.23]	[226.88]	[76.94]	[42.94]
W3 p06	5.75	0.25 (0.64)	0.43 (1.13)	1.46 (4.55)	4.81 (12.71)	-0.42 (0.38)	106.38 (222.70)	96.53 (233.24)	134.16 (430.73)	120.43 (518.50)	2.94 (49.02)	-1.58 (175.55)	-2.80 (49.02)	4.10 (18.80)	1.84 (6.59)
	0.05	[0.13]	[0.18]	[0.32]	[1.64]	[0.12]	[41.64]	[34.72]	[33.98]	[43.62]	[117.39]	[177.13]	[51.82]	[14.70]	[4.75]
W3 p07	9.75	0.63 (0.63)	1.29 (1.62)	5.28 (7.93)	17.88 (18.58)	-0.48 (1.87)	137.90 (141.29)	264.23 (278.33)	802.54 (882.35)	1419.25 (1604.35)	1941.18 (3032.27)	877.41 (1534.07)	139.53 (296.61)	31.34 (82.80)	4.14 (18.99)
	0.09	[0.13]	[0.53]	[1.94]	[5.52]	[0.14]	[21.30]	[55.56]	[216.67]	[424.35]	[901.90]	[662.50]	[157.70]	[51.55]	[14.85]
W3 p08	15.25	1.28 (1.81)	2.45 (2.94)	8.70 (12.91)	35.65 (42.15)	0.61 (5.90)	405.71 (429.53)	590.35 (624.69)	1313.89 (1429.84)	1779.34 (2058.18)	1274.87 (2381.37)	186.68 (756.56)	26.72 (61.66)	7.91 (61.66)	3.07 (17.96)
	0.14	[0.88]	[1.84]	[6.29]	[19.11]	[0.62]	[270.54]	[317.61]	[674.70]	[926.58]	[871.48]	[570.18]	[162.82]	[53.75]	[14.89]
W3 p09	12.5	1.26 (1.51)	2.03 (2.26)	7.62 (9.29)	34.37 (33.10)	-0.27 (3.20)	464.83 (463.81)	610.99 (606.86)	1226.59 (1253.41)	1625.25 (1700.05)	991.26 (1421.25)	30.22 (367.07)	6.84 (87.65)	3.02 (25.57)	3.02 (9.49)
	0.11	[0.29]	[0.31]	[1.83]	[3.66]	[3.47]	[46.49]	[61.24]	[125.56]	[178.70]	[441.25]	[193.14]	[57.51]	[18.74]	[6.47]
W3 p10	18.5	0.96 (1.46)	1.22 (1.61)	5.37 (10.07)	22.42 (32.83)	2.15 (10.18)	65.12 (68.91)	210.48 (221.85)	582.43 (696.66)	935.37 (1122.90)	1591.17 (2056.98)	824.17 (1402.30)	259.15 (158.99)	82.42 (158.99)	26.89 (52.91)
	0.16	[0.35]	[0.38]	[1.99]	[3.98]	[4.56]	[31.71]	[40.38]	[72.89]	[121.11]	[693.91]	[583.98]	[174.83]	[77.02]	[26.16]
W3 p11	10.5	0.39 (0.60)	0.73 (0.85)	3.36 (5.08)	18.89 (18.41)	0.01 (2.42)	144.15 (136.28)	274.68 (284.65)	576.85 (634.94)	830.74 (973.11)	769.37 (1598.79)	194.94 (674.52)	42.40 (178.61)	11.66 (73.96)	1.58 (15.99)
	0.09	[0.11]	[0.45]	[1.32]	[3.79]	[0.36]	[21.43]	[50.14]	[157.34]	[295.99]	[742.83]	[475.98]	[136.28]	[62.31]	[14.42]

Table B1 continued

Table B1 (*continued*)

Source	radius (''/pc)	$F_{3.6}$	$F_{4.5}$	$F_{5.8}$	$F_{7.7}$	$F_{8.0}$	$F_{19.7}$	$F_{24.2}$	$F_{31.5}$	$F_{37.1}$	F_{70}	F_{160}	F_{250}	F_{350}	F_{500}
W3 p12	12.75	1.11 (1.41)	2.10 (2.38)	7.17 (9.60)	31.20 (34.85)	-0.38 (3.48)	489.81 (494.10)	631.30 (636.60)	1196.75 (1236.20)	1506.11 (1615.55)	866.07 (1359.13)	131.83 (365.58)	23.79 (104.07)	7.43 (34.55)	2.98 (12.82)
	0.11	[0.32]	[0.35]	[2.54]	[4.80]	[3.86]	[49.17]	[63.35]	[126.01]	[186.18]	[500.61]	[234.12]	[80.31]	[27.11]	[9.84]
W3 p13	26.5	0.82 (1.84)	0.91 (1.81)	3.38 (12.49)	11.68 (6.12)	0.63 (17.67)	36.61 (19.62)	93.37 (68.54)	127.77 (118.03)	254.67 (208.42)	1335.42 (2809.61)	1019.31 (1834.38)	402.19 (678.18)	125.05 (224.13)	31.19 (74.70)
	0.24	[0.25]	[0.28]	[1.49]	[14.98]	[5.49]	[35.88]	[87.86]	[269.81]	[549.48]	[2079.79]	[821.42]	[278.91]	[99.87]	[43.62]
W3 p14	5.0	0.05 (0.13)	0.07 (0.15)	0.27 (0.92)	1.78 (2.15)	0.01 (1.09)	13.77 (21.97)	20.85 (37.85)	32.58 (73.51)	37.34 (105.99)	-0.78 (254.51)	-2.38 (155.13)	4.44 (52.44)	0.91 (18.35)	1.08 (6.04)
	0.04	[0.01]	[0.02]	[0.14]	[0.47]	[0.15]	[5.29]	[9.50]	[16.35]	[22.34]	[16.98]	[157.52]	[48.00]	[17.44]	[4.97]

NOTE— $F_{3.6}$, $F_{4.5}$, $F_{5.8}$, and $F_{8.0}$ refer to fluxes from Spitzer-IRAC at 3.6, 4.5, 5.8, and 8.0 μm , respectively. $F_{7.7}$, $F_{19.1}$, $F_{31.5}$, and $F_{37.1}$ refer to fluxes from SOFIA-FORCAST at 7.7, 19.1, 31.5, and 37.5 μm , respectively. F_{70} , F_{160} , F_{250} , F_{350} , and F_{500} refer to fluxes from Herschel-PACS/SPIRE at 70, 160, 250, 350, and 500 μm , respectively. $F_{12.0}$, $F_{25.0}$, $F_{60.0}$, and $F_{100.0}$ refer to fluxes from IRAS-HIRES at 12.0, 25.0, 60.0, and 100.0 μm , respectively. The three dots refer to either data not found or saturated at that wavelength. First row for each source refers to background subtracted flux. Second row for each source with fluxes in parenthesis refers to non background subtracted flux (in many FORCAST 7.7 μm images we find that the estimated background has a slight negative value, which results from a calibration offset problem; hence, background subtracted values appear larger in this table; however, we still expect these background subtracted values to be accurate). Third row for each source with square brackets refers to the associated error to the background subtracted fluxes. † No Herschel-PACS 70 μm data is available and SOFIA-FORCAST 37 μm was used to find the optimal aperture (§3.2.1). For the radius column for each source, the first row refers to '"/>

Table B2. Parameters of the Best Five Fitted Models and Average and Dispersion of Good Models

Source	χ^2	M_c (M_\odot)	Σ_{cl} ($g\text{ cm}^{-2}$)	R_c (pc)	m_* (M_\odot)	θ_{view} ($^\circ$)	A_V (mag)	M_{env} (M_\odot)	$\theta_{w,esc}$ (deg)	\dot{M}_{disk} (M_\odot/yr)	$L_{bol,iso}$ (L_\odot)	L_{bol} (L_\odot)
AFGL5180 p01	0.21	60	0.100	0.18	8.0	88.6	30	40.2	33.2	4.4×10^{-5}	4.1×10^3	1.0×10^4
$d = 1.8\text{ kpc}$	0.27	60	0.316	0.10	16.0	64.8	42	19.0	55.6	1.1×10^{-4}	4.4×10^3	3.6×10^4
$R_{ap} = 12.25''$	0.28	80	0.21	0.21	16.0	79.9	38	31.2	53.8	5.0×10^{-5}	4.4×10^3	2.9×10^4
$R_{ap} = 0.10\text{ pc}$	0.37	80	0.316	0.12	24.0	82.8	24	14.1	66.6	1.0×10^{-4}	3.8×10^3	8.1×10^4
Avg. model	0.39	80	0.100	0.21	12.0	88.6	52	46.5	40.0	5.4×10^{-5}	4.7×10^3	1.6×10^4
Avg. model	#161	53^{+28}_{-18}	$0.309^{+0.700}_{-0.215}$	$0.10^{+0.10}_{-0.05}$	$12.0^{+7.1}_{-4.5}$	70.9 ± 12.9	58 ± 51	$16.7^{+34.1}_{-11.2}$	45.9 ± 12.7	$10.0^{+12.4}_{-5.5} \times 10^{-5}$	$4.9^{+2.4}_{-1.8} \times 10^3$	$2.5^{+4.4}_{-1.6} \times 10^4$
Avg. model $\Sigma_{cl,GB} = 0.29$	#55	52^{+24}_{-17}	0.316	$0.09^{+0.02}_{-0.02}$	$12.6^{+4.0}_{-4.9}$	70.9 ± 12.7	38 ± 28	$18.6^{+4.5}_{-3.7}$	48.9 ± 11.6	$9.7^{+1.0}_{-0.9} \times 10^{-5}$	$4.0^{+1.0}_{-0.8} \times 10^3$	$2.6^{+3.7}_{-1.3} \times 10^4$
AFGL5180 p02	0.30	60	0.100	0.18	12.0	12.8	115	24.9	51.5	4.2×10^{-5}	4.4×10^4	1.5×10^4
$d = 1.8\text{ kpc}$	0.33	100	0.100	0.23	24.0	61.6	156	18.5	69.7	4.1×10^{-5}	5.7×10^4	7.1×10^4
$R_{ap} = 24.25''$	0.36	50	0.100	0.16	8.0	29.0	146	30.0	37.1	4.1×10^{-5}	3.1×10^4	9.5×10^3
$R_{ap} = 0.21\text{ pc}$	0.49	40	0.100	0.15	8.0	12.8	104	20.0	43.2	3.6×10^{-5}	3.0×10^4	8.8×10^3
Avg. model	0.60	80	0.100	0.21	16.0	51.3	174	31.2	53.8	5.0×10^{-5}	3.3×10^4	2.9×10^4
Avg. model	#370	53^{+32}_{-23}	$0.274^{+0.484}_{-0.175}$	$0.10^{+0.10}_{-0.05}$	$12.4^{+9.9}_{-5.3}$	51.9 ± 22.7	121 ± 67	$15.0^{+17.6}_{-10.7}$	52.5 ± 14.7	$7.9^{+7.1}_{-4.7} \times 10^{-5}$	$1.4^{+5.2}_{-2.1} \times 10^4$	$2.2^{+4.7}_{-1.7} \times 10^4$
Avg. model $\Sigma_{cl,GB} = 0.10$	#155	64^{+23}_{-17}	0.100	$0.19^{+0.03}_{-0.03}$	$11.6^{+3.6}_{-3.6}$	56.1 ± 21.5	111 ± 54	$27.4^{+13.2}_{-8.9}$	47.8 ± 12.0	$4.3^{+0.6}_{-0.6} \times 10^{-5}$	$0.9^{+1.0}_{-0.7} \times 10^4$	$1.6^{+0.8}_{-0.8} \times 10^4$
AFGL5180 p03	0.28	50	0.100	0.16	12.0	77.0	0	15.0	59.5	3.4×10^{-5}	1.6×10^3	1.4×10^4
$d = 1.8\text{ kpc}$	0.43	50	0.316	0.09	16.0	74.0	3	7.8	67.6	7.1×10^{-5}	1.7×10^3	3.1×10^4
$R_{ap} = 12.25''$	1.77	80	1.000	0.07	32.0	85.7	5	2.7	78.7	1.4×10^{-4}	1.7×10^3	1.6×10^5
$R_{ap} = 0.10\text{ pc}$	2.23	40	0.100	0.15	8.0	39.2	131	20.0	43.2	3.6×10^{-5}	2.0×10^4	8.8×10^3
Avg. model	2.24	20	1.000	0.03	8.0	43.5	147	4.0	50.7	1.5×10^{-4}	1.8×10^4	1.1×10^4
Avg. model	#38	51^{+5}_{-5}	$0.207^{+0.201}_{-0.102}$	$0.12^{+0.04}_{-0.03}$	$14.7^{+3.1}_{-3.1}$	61.0 ± 20.8	67 ± 60	$9.7^{+15.4}_{-3.5}$	64.8 ± 5.1	$5.4^{+2.9}_{-1.9} \times 10^{-5}$	$7.4^{+29.8}_{-16.0} \times 10^3$	$2.4^{+2.0}_{-1.1} \times 10^4$
Avg. model $\Sigma_{cl,GB} = 0.27$	#20	50^{+0}_{-0}	0.316	$0.09^{+0.00}_{-0.00}$	$16.0^{+0.0}_{-0.0}$	57.3 ± 21.4	87 ± 63	$7.8^{+0.0}_{-0.0}$	67.6 ± 0.0	$7.1^{+0.0}_{-0.0} \times 10^{-5}$	$12.2^{+10.0}_{-10.0} \times 10^3$	$3.1^{+0.0}_{-0.0} \times 10^4$
AFGL5180 p04	0.42	80	0.316	0.12	4.0	12.8	167	72.5	15.9	8.9×10^{-5}	5.1×10^3	9.2×10^2
$d = 1.8\text{ kpc}$	0.47	100	0.316	0.13	4.0	12.8	179	90.7	14.2	9.5×10^{-5}	5.4×10^3	1.1×10^3
$R_{ap} = 14.75''$	0.53	60	0.316	0.10	2.0	12.8	133	56.4	13.3	5.9×10^{-5}	4.1×10^3	8.7×10^2
$R_{ap} = 0.13\text{ pc}$	0.65	50	0.316	0.09	4.0	12.8	229	41.4	21.6	7.7×10^{-5}	8.2×10^3	1.4×10^3
Avg. model	0.67	50	0.316	0.09	2.0	12.8	141	45.8	14.9	5.6×10^{-5}	4.4×10^3	8.1×10^2
Avg. model	#479	52^{+43}_{-23}	$0.306^{+0.476}_{-0.186}$	$0.10^{+0.09}_{-0.05}$	$6.3^{+9.9}_{-3.9}$	53.7 ± 22.6	151 ± 130	$21.5^{+39.9}_{-14.0}$	38.1 ± 23.0	$7.0^{+5.0}_{-2.9} \times 10^{-5}$	$3.4^{+19.9}_{-2.9} \times 10^3$	$4.8^{+26.7}_{-4.1} \times 10^3$
Avg. model $\Sigma_{cl,GB} = 0.53$	#237	59^{+36}_{-22}	0.316	$0.10^{+0.03}_{-0.02}$	$5.4^{+8.3}_{-3.3}$	55.2 ± 22.4	98 ± 117	$29.0^{+44.5}_{-17.5}$	32.3 ± 23.6	$7.1^{+1.5}_{-1.2} \times 10^{-5}$	$2.5^{+13.4}_{-2.0} \times 10^3$	$3.5^{+18.1}_{-2.7} \times 10^3$
G18.67 p01	0.60	480	0.100	0.51	24.0	43.5	162	417.7	21.0	1.4×10^{-4}	6.2×10^4	8.7×10^4
$d = 10.8\text{ kpc}$	0.64	400	0.100	0.47	24.0	51.3	148	331.0	23.7	1.3×10^{-4}	5.5×10^4	8.6×10^4
$R_{ap} = 10.00''$	0.73	320	0.100	0.42	32.0	61.6	175	228.4	33.5	1.3×10^{-4}	6.9×10^4	1.6×10^5
$R_{ap} = 0.52\text{ pc}$	0.86	200	0.316	0.19	12.0	22.3	84	172.7	17.3	1.9×10^{-4}	3.5×10^4	4.0×10^4
Avg. model	0.88	400	0.100	0.47	32.0	51.3	202	304.1	29.2	1.5×10^{-4}	8.6×10^4	1.6×10^5
Avg. model	#570	200^{+167}_{-91}	$0.419^{+0.908}_{-0.286}$	$0.16^{+0.22}_{-0.09}$	$23.0^{+18.5}_{-10.2}$	64.6 ± 16.4	109 ± 68	$128.5^{+137.3}_{-66.4}$	30.7 ± 12.4	$2.9^{+2.9}_{-1.5} \times 10^{-4}$	$4.3^{+2.9}_{-1.7} \times 10^4$	$1.2^{+2.0}_{-0.7} \times 10^5$
Avg. model $\Sigma_{cl,GB} = 0.37$	#226	217^{+60}_{-47}	0.316	$0.19^{+0.02}_{-0.02}$	$19.7^{+13.9}_{-8.1}$	63.9 ± 17.1	87 ± 51	$156.3^{+57.0}_{-41.8}$	27.5 ± 12.2	$2.3^{+0.4}_{-0.4} \times 10^{-4}$	$3.7^{+1.5}_{-1.1} \times 10^4$	$0.8^{+1.1}_{-0.3} \times 10^5$
G18.67 p02	0.46	160	0.100	0.29	12.0	29.0	65	130.2	24.6	7.4×10^{-5}	1.6×10^4	1.9×10^4
$d = 10.8\text{ kpc}$	0.48	240	0.100	0.36	8.0	22.3	16	225.7	13.3	7.1×10^{-5}	1.0×10^4	1.1×10^4
$R_{ap} = 10.50''$	0.54	160	0.100	0.29	17.1	22.3	27	142.8	17.1	6.3×10^{-5}	1.0×10^4	1.1×10^4
$R_{ap} = 0.55\text{ pc}$	0.55	80	0.316	0.12	16.0	43.5	89	41.6	41.5	1.5×10^{-4}	2.3×10^4	4.2×10^4
Avg. model	0.55	200	0.100	0.33	8.0	22.3	10	180.9	14.4	6.7×10^{-5}	9.1×10^3	9.5×10^3
Avg. model	#413	131^{+130}_{-65}	$0.192^{+0.374}_{-0.127}$	$0.19^{+0.25}_{-0.11}$	$13.8^{+9.6}_{-5.6}$	58.8 ± 19.9	51 ± 65	$70.9^{+150.2}_{-48.1}$	34.3 ± 18.1	$1.1^{+0.5}_{-0.5} \times 10^{-4}$	$1.6^{+3.2}_{-2.1} \times 10^4$	$3.1^{+6.1}_{-2.1} \times 10^4$
Avg. model $\Sigma_{cl,GB} = 0.35$	#68	91^{+25}_{-20}	0.316	$0.12^{+0.01}_{-0.01}$	$20.2^{+6.6}_{-6.6}$	56.8 ± 20.9	73 ± 73	$34.8^{+5.9}_{-5.9}$	50.0 ± 10.4	$1.4^{+0.1}_{-0.1} \times 10^{-4}$	$2.6^{+2.0}_{-2.0} \times 10^4$	$6.6^{+3.4}_{-3.4} \times 10^4$
G18.67 p03	0.97	100	1.000	0.07	8.0	22.3	0	84.3	17.5	3.1×10^{-4}	1.2×10^4	1.3×10^4
$d = 10.8\text{ kpc}$	1.00	80	3.160	0.04	8.0	29.0	0	64.8	18.8	7.0×10^{-4}	1.3×10^4	1.8×10^4

Table B2 continued

Table B2 (continued)

Source	χ^2	M_c (M_\odot)	Σ_{cl} ($g\text{ cm}^{-2}$)	R_c (pc)	m_* (M_\odot)	θ_{view} ($^\circ$)	A_V (mag)	M_{env} (M_\odot)	$\theta_{w,esc}$ (deg)	\dot{M}_{disk} (M_\odot/yr)	$L_{bol,iso}$ (L_\odot)	L_{bol} (L_\odot)
$R_{ap} = 11.75''$	1.06	320	0.100	0.42	12.0	22.3	94	296.2	14.9	9.3×10^{-5}	2.1×10^4	2.2×10^4
$R_{ap} = 0.62\text{ pc}$	1.08	240	0.100	0.36	16.0	29.0	129	196.8	24.2	9.5×10^{-5}	2.9×10^4	3.5×10^4
	1.19	50	3.160	0.03	12.0	34.4	141	27.7	30.2	7.1×10^{-4}	3.4×10^4	5.1×10^4
Avg. model	#175	190^{+197}_{-97}	$0.188^{+0.485}_{-0.135}$	$0.23^{+0.38}_{-0.15}$	$13.9^{+4.5}_{-3.4}$	53.7 ± 18.6	90 ± 43	$143.3^{+218.0}_{-86.5}$	24.3 ± 9.7	$1.3^{+1.4}_{-0.7} \times 10^{-4}$	$2.1^{+1.5}_{-0.9} \times 10^4$	$3.3^{+2.2}_{-1.3} \times 10^4$
Avg. model $\Sigma_{cl,CB} = 0.39$	#94	126^{+57}_{-39}	0.316	$0.15^{+0.03}_{-0.02}$	$22.9^{+18.6}_{-10.3}$	52.2 ± 20.3	144 ± 95	$59.5^{+10.6}_{-9.0}$	43.6 ± 12.9	$1.8^{+0.3}_{-0.3} \times 10^{-4}$	$6.0^{+17.8}_{-5.0} \times 10^4$	$9.4^{+17.9}_{-6.1} \times 10^4$
G18.67 p04	0.55	240	0.100	0.36	12.0	29.0	86	210.9	18.9	8.5×10^{-5}	1.7×10^4	2.0×10^4
$d = 10.8\text{ kpc}$	0.59	200	0.100	0.33	12.0	29.0	85	174.1	20.5	8.0×10^{-5}	1.7×10^4	2.0×10^4
$R_{ap} = 10.25''$	0.66	160	0.100	0.29	16.0	34.4	125	115.9	31.6	8.1×10^{-5}	2.6×10^4	3.3×10^4
$R_{ap} = 0.54\text{ pc}$	0.66	160	0.100	0.29	24.0	51.3	137	86.6	44.7	8.5×10^{-5}	2.8×10^4	7.8×10^4
	0.68	200	0.100	0.33	16.0	29.0	154	159.7	26.6	8.9×10^{-5}	4.3×10^4	3.4×10^4
Avg. model	#469	146^{+160}_{-76}	$0.237^{+0.546}_{-0.165}$	$0.18^{+0.29}_{-0.11}$	$16.0^{+11.9}_{-6.8}$	58.5 ± 20.5	90 ± 78	$80.1^{+161.3}_{-53.5}$	34.1 ± 17.3	$1.4^{+1.4}_{-0.7} \times 10^{-4}$	$2.3^{+5.9}_{-1.6} \times 10^4$	$4.4^{+9.0}_{-3.0} \times 10^4$
Avg. model $\Sigma_{cl,CB} = 0.44$	#74	101^{+18}_{-18}	0.316	$0.13^{+0.01}_{-0.01}$	$18.2^{+5.4}_{-5.4}$	54.5 ± 21.7	97 ± 71	$51.9^{+12.9}_{-12.9}$	41.7 ± 9.9	$1.6^{+0.2}_{-0.2} \times 10^{-4}$	$2.4^{+1.6}_{-1.6} \times 10^4$	$5.6^{+2.6}_{-2.6} \times 10^4$
G18.67 p05	0.28	50	3.160	0.03	4.0	22.3	59	41.6	18.7	4.4×10^{-4}	1.1×10^4	7.2×10^3
$d = 10.8\text{ kpc}$	0.55	80	0.316	0.12	8.0	22.3	128	62.7	22.6	1.2×10^{-4}	2.6×10^4	8.2×10^3
$R_{ap} = 15.25''$	0.56	30	3.160	0.02	4.0	29.0	19	22.0	26.0	3.7×10^{-4}	5.4×10^3	4.9×10^3
$R_{ap} = 0.80\text{ pc}$	0.62	40	1.000	0.05	8.0	29.0	167	23.9	31.4	2.3×10^{-4}	4.4×10^4	1.3×10^4
	0.62	30	1.000	0.04	8.0	39.2	84	13.9	37.7	2.0×10^{-4}	1.2×10^4	1.2×10^4
Avg. model	#1616	89^{+95}_{-46}	$0.305^{+0.710}_{-0.213}$	$0.13^{+0.18}_{-0.07}$	$13.8^{+11.3}_{-6.2}$	55.5 ± 22.1	150 ± 99	$38.2^{+86.8}_{-26.5}$	39.8 ± 17.6	$1.3^{+1.5}_{-0.7} \times 10^{-4}$	$2.0^{+1.5}_{-1.5} \times 10^4$	$3.3^{+2.3}_{-1.6} \times 10^4$
Avg. model $\Sigma_{cl,CB} = 0.22$	#431	80^{+32}_{-32}	0.316	$0.12^{+0.03}_{-0.03}$	$13.9^{+11.4}_{-6.3}$	55.4 ± 22.2	130 ± 91	$34.4^{+18.7}_{-18.7}$	42.3 ± 17.9	$1.2^{+0.4}_{-0.3} \times 10^{-4}$	$1.8^{+1.5}_{-1.4} \times 10^4$	$3.1^{+6.9}_{-2.2} \times 10^4$
G28.37 p01	0.04	80	0.100	0.21	12.0	47.5	47	46.5	40.0	5.4×10^{-5}	6.9×10^3	1.6×10^4
$d = 5.0\text{ kpc}$	0.06	100	0.100	0.23	16.0	47.5	103	53.0	44.7	6.2×10^{-5}	1.3×10^4	3.0×10^4
$R_{ap} = 12.50''$	0.06	100	0.100	0.23	12.0	12.8	140	68.8	34.0	6.1×10^{-5}	6.9×10^4	1.7×10^4
$R_{ap} = 0.30\text{ pc}$	0.07	80	0.100	0.21	8.0	34.4	47	61.5	26.8	5.0×10^{-5}	7.0×10^3	9.7×10^3
	0.07	60	0.100	0.18	8.0	39.2	36	40.2	33.2	4.4×10^{-5}	6.1×10^3	1.0×10^4
Avg. model	#1278	82^{+87}_{-42}	$0.294^{+0.661}_{-0.203}$	$0.12^{+0.17}_{-0.07}$	$13.5^{+12.2}_{-6.4}$	55.0 ± 22.1	93 ± 74	$30.1^{+75.1}_{-21.5}$	42.8 ± 19.0	$1.1^{+1.3}_{-0.6} \times 10^{-4}$	$1.9^{+6.7}_{-2.2} \times 10^4$	$3.0^{+7.6}_{-2.2} \times 10^4$
Avg. model $\Sigma_{cl,CB} = 0.57$	#226	48^{+26}_{-17}	1.000	$0.05^{+0.01}_{-0.01}$	$14.4^{+11.1}_{-6.3}$	53.3 ± 22.5	95 ± 80	$11.6^{+14.4}_{-6.4}$	50.6 ± 14.9	$2.3^{+0.7}_{-0.6} \times 10^{-4}$	$2.1^{+8.6}_{-1.7} \times 10^4$	$4.3^{+9.0}_{-2.9} \times 10^4$
G28.37 p02	0.12	100	0.100	0.23	24.0	12.8	160	18.5	69.7	4.1×10^{-5}	1.7×10^5	7.1×10^4
$d = 5.0\text{ kpc}$	0.12	30	3.160	0.02	4.0	29.0	64	22.0	26.0	3.7×10^{-4}	5.4×10^3	4.9×10^3
$R_{ap} = 10.75''$	0.12	60	0.100	0.18	8.0	29.0	137	40.2	33.2	4.4×10^{-5}	3.4×10^4	1.0×10^4
$R_{ap} = 0.26\text{ pc}$	0.12	80	0.100	0.21	16.0	51.3	140	31.2	53.8	5.0×10^{-5}	3.3×10^4	2.9×10^4
	0.12	80	0.100	0.21	12.0	39.2	142	46.5	40.0	5.4×10^{-5}	2.9×10^4	1.6×10^4
Avg. model	#5857	93^{+132}_{-55}	$0.465^{+1.112}_{-0.328}$	$0.10^{+0.15}_{-0.06}$	$6.1^{+14.0}_{-4.2}$	57.4 ± 21.5	331 ± 378	$58.5^{+133.0}_{-40.6}$	25.9 ± 19.2	$1.3^{+2.2}_{-0.8} \times 10^{-4}$	$5.7^{+38.7}_{-5.0} \times 10^3$	$8.5^{+64.5}_{-7.5} \times 10^3$
Avg. model $\Sigma_{cl,CB} = 0.59$	#1532	74^{+99}_{-42}	1.000	$0.06^{+0.03}_{-0.02}$	$4.9^{+12.6}_{-3.5}$	57.7 ± 21.4	332 ± 385	$46.7^{+97.7}_{-31.6}$	24.4 ± 18.7	$2.0^{+1.9}_{-1.0} \times 10^{-4}$	$5.3^{+28.4}_{-4.5} \times 10^3$	$8.9^{+54.3}_{-7.1} \times 10^3$
G28.37 p03	0.32	80	1.000	0.07	4.0	12.8	210	71.9	15.2	2.1×10^{-4}	1.8×10^4	2.9×10^3
$d = 5.0\text{ kpc}$	0.48	30	3.160	0.02	4.0	47.5	7	22.0	26.0	3.7×10^{-4}	1.9×10^3	4.9×10^3
$R_{ap} = 9.75''$	0.48	40	1.000	0.05	2.0	22.3	0	35.8	15.6	1.3×10^{-4}	1.6×10^3	2.0×10^3
$R_{ap} = 0.24\text{ pc}$	0.50	20	3.160	0.02	1.0	22.3	28	18.0	13.9	1.8×10^{-4}	1.9×10^3	2.2×10^3
	0.52	20	3.160	0.02	2.0	43.5	9	16.0	22.0	2.4×10^{-4}	1.8×10^3	3.9×10^3
Avg. model	#761	68^{+62}_{-33}	$0.316^{+0.765}_{-0.223}$	$0.11^{+0.15}_{-0.06}$	$11.5^{+12.6}_{-6.0}$	53.4 ± 22.5	279 ± 96	$26.6^{+52.2}_{-17.6}$	41.6 ± 18.0	$1.1^{+1.2}_{-0.6} \times 10^{-4}$	$1.4^{+5.6}_{-1.1} \times 10^4$	$2.3^{+6.4}_{-1.7} \times 10^4$
Avg. model $\Sigma_{cl,CB} = 1.23$	#86	37^{+12}_{-9}	1.000	$0.04^{+0.01}_{-0.01}$	$8.5^{+13.5}_{-3.9}$	46.2 ± 25.0	229 ± 101	$12.2^{+13.5}_{-6.8}$	42.4 ± 15.9	$1.9^{+0.2}_{-0.2} \times 10^{-4}$	$1.0^{+0.8}_{-0.8} \times 10^4$	$1.5^{+5.9}_{-1.1} \times 10^4$
G30.76 p01	3.12	100	0.100	0.23	8.0	58.3	13	81.1	23.3	5.5×10^{-5}	6.3×10^3	1.0×10^4
$d = 4.9\text{ kpc}$	3.15	30	1.000	0.04	12.0	64.8	7	5.7	53.4	1.9×10^{-4}	5.1×10^3	4.1×10^4
$R_{ap} = 10.25''$	3.22	80	0.100	0.21	8.0	71.0	2	61.5	26.8	5.0×10^{-5}	5.2×10^3	9.7×10^3
$R_{ap} = 0.24\text{ pc}$	3.26	100	0.100	0.23	12.0	68.0	32	68.8	34.0	6.1×10^{-5}	7.1×10^3	1.7×10^4
	3.38	120	0.100	0.25	8.0	39.2	40	101.1	20.8	5.8×10^{-5}	8.2×10^3	1.1×10^4
Avg. model	#52	90^{+34}_{-29}	$0.122^{+0.126}_{-0.062}$	$0.20^{+0.13}_{-0.08}$	$10.4^{+4.0}_{-2.9}$	67.7 ± 15.1	26 ± 21	$58.4^{+45.0}_{-25.4}$	32.5 ± 10.2	$6.4^{+3.4}_{-2.2} \times 10^{-5}$	$6.6^{+1.4}_{-1.2} \times 10^3$	$1.6^{+1.2}_{-0.7} \times 10^4$

Table B2 continued

Table B2 (continued)

Source	χ^2	M_c	Σ_{cl}	R_c	m_*	θ_{view}	A_V	M_{env}	$\theta_{w,\text{esc}}$	\dot{M}_{disk}	$L_{\text{bol,iso}}$	L_{bol}
		(M_{\odot})	(g cm^{-2})	(pc)	(M_{\odot})	($^{\circ}$)	(mag)	(M_{\odot})	(deg)	(M_{\odot}/yr)	(L_{\odot})	(L_{\odot})
Avg. model $\Sigma_{\text{cl,GB}} = 0.39$	#96	70^{+29}_{-21}	0.316	$0.11^{+0.02}_{-0.02}$	$14.1^{+10.0}_{-5.9}$	60.8 ± 18.4	55 ± 79	$31.3^{+9.5}_{-7.3}$	44.1 ± 13.0	$12.1^{+2.2}_{-1.8} \times 10^{-5}$	$10.6^{+29.5}_{-7.8} \times 10^3$	$3.4^{+5.8}_{-2.1} \times 10^4$
G30.76 p02	0.26	160	0.100	0.29	12.0	12.8	195	130.2	24.6	7.4×10^{-5}	9.4×10^4	1.9×10^4
$d = 4.9$ kpc	0.29	40	1.000	0.05	12.0	34.4	217	15.6	42.4	2.5×10^{-4}	1.3×10^5	4.5×10^4
$R_{\text{ap}} = 17.00''$	0.31	50	3.160	0.03	24.0	54.9	251	5.5	56.4	6.8×10^{-4}	1.2×10^5	1.9×10^5
$R_{\text{ap}} = 0.40$ pc	0.32	100	0.316	0.13	24.0	51.3	208	35.5	53.9	1.5×10^{-4}	8.7×10^4	8.8×10^4
0.32	80	80	0.316	0.12	16.0	34.4	208	41.6	41.5	1.5×10^{-4}	1.2×10^5	4.2×10^4
Avg. model	#1057	101^{+97}_{-59}	$0.274^{+0.611}_{-0.189}$	$0.14^{+0.19}_{-0.08}$	$14.3^{+11.2}_{-5.9}$	56.9 ± 21.5	125 ± 84	$45.7^{+101.6}_{-34.3}$	38.1 ± 17.5	$1.3^{+1.4}_{-0.7} \times 10^{-4}$	$2.0^{+8.0}_{-1.4} \times 10^4$	$3.5^{+8.0}_{-1.4} \times 10^4$
Avg. model $\Sigma_{\text{cl,GB}} = 0.46$	#302	82^{+26}_{-25}	0.316	$0.12^{+0.02}_{-0.02}$	$13.6^{+5.7}_{-5.7}$	59.2 ± 21.1	96 ± 84	$40.2^{+16.9}_{-10.3}$	39.6 ± 15.7	$1.3^{+0.3}_{-0.2} \times 10^{-4}$	$1.4^{+1.1}_{-1.1} \times 10^4$	$3.1^{+2.0}_{-1.7} \times 10^4$
G30.76 p03	0.23	80	0.316	0.12	24.0	71.0	132	14.1	66.6	1.0×10^{-4}	5.9×10^3	8.1×10^4
$d = 4.9$ kpc	0.23	50	0.100	0.16	8.0	54.9	94	30.0	37.1	4.1×10^{-5}	4.0×10^3	9.5×10^3
$R_{\text{ap}} = 9.50''$	0.24	80	0.100	0.21	16.0	68.0	126	31.2	53.8	5.0×10^{-5}	5.3×10^3	2.9×10^4
$R_{\text{ap}} = 0.23$ pc	0.24	60	0.100	0.18	8.0	39.2	133	40.2	33.2	4.4×10^{-5}	6.1×10^3	1.0×10^4
0.25	30	30	3.160	0.02	16.0	51.3	292	1.0	56.0	5.1×10^{-4}	7.4×10^4	1.0×10^5
Avg. model	#516	60^{+47}_{-27}	$0.299^{+0.704}_{-0.210}$	$0.10^{+0.13}_{-0.06}$	$13.6^{+10.6}_{-5.9}$	58.1 ± 21.9	160 ± 88	$18.0^{+34.5}_{-11.8}$	48.6 ± 14.6	$9.9^{+12.0}_{-5.4} \times 10^{-5}$	$1.3^{+5.6}_{-1.1} \times 10^4$	$3.0^{+6.4}_{-1.6} \times 10^4$
Avg. model $\Sigma_{\text{cl,GB}} = 0.51$	#140	60^{+38}_{-23}	0.316	$0.10^{+0.03}_{-0.02}$	$14.8^{+12.3}_{-6.7}$	56.2 ± 22.5	157 ± 88	$18.0^{+7.8}_{-5.4}$	52.4 ± 14.6	$9.9^{+1.2}_{-1.1} \times 10^{-5}$	$1.6^{+1.9}_{-1.3} \times 10^4$	$3.5^{+7.3}_{-1.7} \times 10^4$
G58.77 p01	0.75	400	0.100	0.47	8.0	22.3	2	386.2	9.6	8.1×10^{-5}	9.8×10^3	1.0×10^4
$d = 3.3$ kpc	0.83	240	0.100	0.36	12.0	22.3	116	210.9	18.9	8.5×10^{-5}	2.8×10^4	2.0×10^4
$R_{\text{ap}} = 21.50''$	0.85	480	0.100	0.51	8.0	22.3	0	463.2	8.6	8.5×10^{-5}	9.5×10^3	9.7×10^3
$R_{\text{ap}} = 0.34$ pc	0.99	200	0.100	0.33	12.0	29.0	79	174.1	20.5	8.0×10^{-5}	1.7×10^4	2.0×10^4
1.07	240	240	0.100	0.36	8.0	22.3	7	225.7	13.3	7.1×10^{-5}	1.0×10^4	1.1×10^4
Avg. model	#198	241^{+116}_{-78}	$0.102^{+0.018}_{-0.015}$	$0.36^{+0.09}_{-0.07}$	$13.3^{+11.1}_{-6.0}$	56.3 ± 20.2	73 ± 76	$178.0^{+148.9}_{-81.1}$	24.4 ± 16.6	$8.2^{+1.1}_{-0.9} \times 10^{-5}$	$2.0^{+5.5}_{-1.5} \times 10^4$	$2.5^{+5.5}_{-1.7} \times 10^4$
Avg. model $\Sigma_{\text{cl,GB}} = 0.10$	#194	245^{+113}_{-77}	0.100	$0.36^{+0.08}_{-0.06}$	$13.2^{+11.1}_{-6.0}$	56.8 ± 20.0	71 ± 75	$181.6^{+148.2}_{-81.6}$	24.2 ± 16.6	$8.1^{+0.6}_{-0.5} \times 10^{-5}$	$2.0^{+5.1}_{-1.4} \times 10^4$	$2.5^{+5.5}_{-1.7} \times 10^4$
G58.77 p02	0.12	40	0.100	0.15	8.0	58.3	40	20.0	43.2	3.6×10^{-5}	2.8×10^3	8.8×10^3
$d = 3.3$ kpc	0.15	60	0.100	0.18	12.0	61.6	59	24.9	51.5	4.2×10^{-5}	3.2×10^3	1.5×10^4
$R_{\text{ap}} = 26.75''$	0.19	100	0.100	0.23	24.0	77.0	104	18.5	69.7	4.1×10^{-5}	5.0×10^3	7.1×10^4
$R_{\text{ap}} = 0.43$ pc	0.22	40	0.316	0.08	12.0	61.6	38	10.8	56.7	8.1×10^{-5}	2.7×10^3	2.0×10^4
0.23	60	60	1.000	0.06	24.0	74.0	56	4.9	70.9	1.9×10^{-4}	3.7×10^3	9.3×10^4
Avg. model	#440	50^{+33}_{-20}	$0.370^{+0.900}_{-0.262}$	$0.09^{+0.10}_{-0.05}$	$13.6^{+9.9}_{-5.7}$	56.3 ± 22.0	141 ± 87	$11.2^{+17.6}_{-6.8}$	54.2 ± 12.5	$1.0^{+1.4}_{-0.6} \times 10^{-4}$	$1.4^{+5.7}_{-1.1} \times 10^4$	$2.9^{+6.0}_{-2.0} \times 10^4$
Avg. model $\Sigma_{\text{cl,GB}} = 0.06$	#161	63^{+21}_{-16}	0.100	$0.18^{+0.03}_{-0.02}$	$11.6^{+5.1}_{-3.5}$	56.8 ± 21.8	118 ± 57	$26.9^{+12.2}_{-8.4}$	48.2 ± 11.7	$0.4^{+0.1}_{-0.1} \times 10^{-4}$	$0.9^{+2.4}_{-0.7} \times 10^4$	$1.6^{+1.5}_{-0.8} \times 10^4$
IRAS20343 p01	5.86	60	1.000	0.06	24.0	88.6	8	4.9	70.9	1.9×10^{-4}	2.1×10^3	9.3×10^4
$d = 1.4$ kpc	6.77	20	1.000	0.03	8.0	58.3	7	4.0	50.7	1.5×10^{-4}	2.2×10^3	1.1×10^4
$R_{\text{ap}} = 15.50''$	7.32	40	0.100	0.15	8.0	79.9	30	20.0	43.2	3.6×10^{-5}	2.2×10^3	8.8×10^3
$R_{\text{ap}} = 0.11$ pc	7.67	40	0.316	0.08	12.0	77.0	0	10.8	56.7	8.1×10^{-5}	1.8×10^3	2.0×10^4
8.06	10	10	3.160	0.01	2.0	39.2	0	5.7	35.4	1.8×10^{-4}	1.4×10^3	2.6×10^3
Avg. model	#64	40^{+22}_{-14}	$0.305^{+0.580}_{-0.200}$	$0.08^{+0.08}_{-0.04}$	$11.1^{+6.5}_{-4.1}$	75.3 ± 11.3	28 ± 27	$9.9^{+10.2}_{-5.0}$	54.9 ± 10.1	$7.5^{+7.0}_{-3.6} \times 10^{-5}$	$2.0^{+0.6}_{-0.5} \times 10^3$	$1.7^{+2.2}_{-1.0} \times 10^4$
Avg. model $\Sigma_{\text{cl,GB}} = 0.20$	#90	45^{+15}_{-15}	0.316	$0.09^{+0.02}_{-0.02}$	$11.6^{+5.3}_{-5.3}$	51.7 ± 23.8	119 ± 87	$10.0^{+5.0}_{-5.0}$	55.8 ± 17.8	$7.0^{+1.2}_{-1.2} \times 10^{-5}$	$10.0^{+1.9}_{-0.9} \times 10^3$	$1.7^{+1.3}_{-1.3} \times 10^4$
IRAS20343 p02	0.95	50	0.100	0.16	4.0	29.0	0	41.0	23.7	3.2×10^{-5}	7.1×10^2	7.9×10^2
$d = 1.4$ kpc	1.81	20	0.316	0.06	8.0	79.9	19	1.6	65.5	4.4×10^{-5}	7.7×10^2	9.9×10^3
$R_{\text{ap}} = 14.50''$	1.88	60	0.100	0.18	4.0	29.0	1	51.2	21.1	3.4×10^{-5}	7.9×10^2	8.9×10^2
$R_{\text{ap}} = 0.10$ pc	1.93	100	0.316	0.13	32.0	85.7	51	4.5	81.4	5.0×10^{-5}	1.3×10^3	1.4×10^5
2.16	30	30	0.100	0.13	8.0	71.0	33	8.0	56.6	2.6×10^{-5}	9.8×10^2	6.3×10^3
Avg. model	#5	57^{+53}_{-28}	$0.199^{+0.175}_{-0.093}$	$0.12^{+0.07}_{-0.04}$	$10.6^{+6.9}_{-4.4}$	62.4 ± 27.5	20 ± 19	$9.3^{+33.1}_{-7.8}$	54.6 ± 27.0	$4.1^{+0.8}_{-0.8} \times 10^{-5}$	$8.8^{+1.8}_{-0.6} \times 10^2$	$1.1^{+12.9}_{-0.8} \times 10^4$
Avg. model $\Sigma_{\text{cl,GB}} = 0.16$	#2	55^{+8}_{-7}	0.100	$0.17^{+0.01}_{-0.01}$	$4.0^{+0.0}_{-0.0}$	29.0 ± 0.0	0 ± 0	$45.8^{+7.8}_{-6.7}$	22.4 ± 1.3	$3.3^{+0.1}_{-0.1} \times 10^{-5}$	$7.5^{+0.6}_{-0.6} \times 10^2$	$0.1^{+0.0}_{-0.0} \times 10^4$
IRAS20343 p03	0.65	240	0.100	0.36	4.0	22.3	47	229.0	9.1	5.1×10^{-5}	1.0×10^3	1.0×10^3
$d = 1.4$ kpc	0.68	100	0.316	0.13	4.0	12.8	149	90.7	14.2	9.5×10^{-5}	5.4×10^3	1.1×10^3
$R_{\text{ap}} = 40.50''$	0.78	400	0.100	0.47	4.0	88.6	9	389.8	6.6	5.8×10^{-5}	9.4×10^2	1.0×10^3

Table B2 continued

Table B2 (continued)

Source	χ^2	M_c (M_\odot)	Σ_{cl} ($g\text{ cm}^{-2}$)	R_c (pc)	m_* (M_\odot)	θ_{view} ($^\circ$)	A_V (mag)	M_{env} (M_\odot)	$\theta_{w,esc}$ (deg)	\dot{M}_{disk} (M_\odot/yr)	$L_{bol,iso}$ (L_\odot)	L_{bol} (L_\odot)
$R_{ap} = 0.27\text{ pc}$	0.89	60	0.316	0.10	4.0	12.8	195	51.4	19.4	8.2×10^{-5}	9.0×10^3	1.4×10^3
	0.92	480	0.100	0.51	4.0	88.6	0	474.1	6.0	6.1×10^{-5}	9.2×10^2	1.0×10^3
Avg. model	#253	107^{+18}_{-62}	$0.158^{+0.196}_{-0.087}$	$0.19^{+0.21}_{-0.10}$	$5.8^{+6.1}_{-3.0}$	49.8 ± 22.3	111 ± 125	$67.9^{+161.0}_{-47.8}$	26.2 ± 21.4	$5.7^{+1.3}_{-1.9} \times 10^{-5}$	$2.9^{+2.3}_{-2.3} \times 10^3$	$2.9^{+2.0}_{-2.3} \times 10^3$
Avg. model $\Sigma_{cl,CB} = 0.05$	#177	144^{+168}_{-78}	0.100	$0.28^{+0.13}_{-0.09}$	$6.0^{+5.0}_{-2.7}$	52.2 ± 20.8	117 ± 132	$99.6^{+213.9}_{-67.9}$	24.6 ± 21.3	$4.7^{+0.8}_{-0.7} \times 10^{-5}$	$2.6^{+1.1}_{-2.1} \times 10^3$	$2.8^{+1.0}_{-2.2} \times 10^3$
W3 p01	20.98	80	3.160	0.04	12.0	39.2	10	58.0	22.5	8.4×10^{-4}	2.8×10^4	5.0×10^4
$d = 1.8\text{ kpc}$	21.76	100	3.160	0.04	12.0	34.4	18	76.7	20.2	9.4×10^{-4}	3.5×10^4	5.2×10^4
$R_{ap} = 10.50''$	21.89	80	3.160	0.04	16.0	47.5	59	50.0	26.6	9.5×10^{-4}	4.6×10^4	1.1×10^5
$R_{ap} = 0.09\text{ pc}$	22.69	160	0.316	0.17	12.0	88.6	0	135.3	19.8	1.8×10^{-4}	2.4×10^4	3.8×10^4
22.69	22.69	200	0.316	0.19	12.0	85.7	0	172.7	17.3	1.9×10^{-4}	2.8×10^4	4.0×10^4
Avg. model	#45	117^{+57}_{-38}	$0.999^{+1.832}_{-0.647}$	$0.08^{+0.08}_{-0.04}$	$13.3^{+2.0}_{-1.7}$	64.4 ± 18.1	11 ± 20	$86.7^{+58.5}_{-34.9}$	22.7 ± 4.2	$4.1^{+4.2}_{-2.1} \times 10^{-4}$	$3.0^{+0.6}_{-0.5} \times 10^4$	$5.8^{+3.0}_{-2.0} \times 10^4$
Avg. model $\Sigma_{cl,CB} = 0.72$	#124	92^{+24}_{-19}	1.000	$0.07^{+0.01}_{-0.01}$	$15.0^{+4.2}_{-3.3}$	65.6 ± 15.8	14 ± 21	$60.1^{+21.9}_{-16.1}$	29.3 ± 5.9	$3.9^{+0.6}_{-0.7} \times 10^{-4}$	$2.5^{+1.0}_{-0.7} \times 10^4$	$7.2^{+3.8}_{-2.5} \times 10^4$
W3 p02	0.42	200	0.316	0.19	32.0	88.6	6	114.7	40.5	2.6×10^{-4}	4.0×10^4	1.8×10^5
$d = 1.8\text{ kpc}$	0.54	240	0.316	0.20	48.0	88.6	39	104.2	49.7	2.9×10^{-4}	5.1×10^4	3.8×10^5
$R_{ap} = 17.00''$	0.69	200	0.316	0.19	24.0	54.9	1	139.7	31.9	2.5×10^{-4}	4.0×10^4	1.0×10^5
$R_{ap} = 0.15\text{ pc}$	0.80	80	3.160	0.04	24.0	54.9	52	35.1	37.3	1.1×10^{-3}	5.6×10^4	2.6×10^5
0.90	0.90	100	3.160	0.04	32.0	54.9	70	36.9	42.4	1.2×10^{-3}	6.5×10^4	3.5×10^5
Avg. model	#78	142^{+83}_{-52}	$0.778^{+1.504}_{-0.513}$	$0.10^{+0.11}_{-0.05}$	$26.0^{+10.6}_{-7.5}$	60.0 ± 15.8	27 ± 29	$77.5^{+60.5}_{-34.0}$	36.8 ± 7.3	$4.4^{+4.1}_{-2.1} \times 10^{-4}$	$4.6^{+1.3}_{-1.0} \times 10^4$	$1.7^{+1.3}_{-0.7} \times 10^5$
Avg. model $\Sigma_{cl,CB} = 0.94$	#54	202^{+110}_{-71}	1.000	$0.10^{+0.03}_{-0.02}$	$48.4^{+23.8}_{-42.3}$	65.6 ± 16.9	39 ± 34	$75.0^{+12.3}_{-10.5}$	48.3 ± 11.0	$6.6^{+1.9}_{-1.5} \times 10^{-4}$	$5.6^{+1.9}_{-1.4} \times 10^4$	$4.7^{+8.2}_{-3.0} \times 10^5$
W3 p03	1.04	60	3.160	0.03	16.0	47.5	37	31.1	32.0	8.4×10^{-4}	3.9×10^4	1.1×10^5
$d = 1.8\text{ kpc}$	1.05	60	3.160	0.03	12.0	39.2	3	37.8	26.7	7.6×10^{-4}	2.6×10^4	5.0×10^4
$R_{ap} = 18.75''$	1.22	160	0.316	0.17	24.0	77.0	37.2	97.6	37.2	2.2×10^{-4}	2.7×10^4	9.9×10^4
$R_{ap} = 0.17\text{ pc}$	1.23	100	1.000	0.07	16.0	39.2	12	66.7	28.3	4.2×10^{-4}	4.3×10^4	9.3×10^4
1.24	1.24	80	1.000	0.07	16.0	47.5	2	46.3	33.6	3.8×10^{-4}	2.8×10^4	8.5×10^4
Avg. model	#397	106^{+65}_{-40}	$0.684^{+1.667}_{-0.485}$	$0.09^{+0.11}_{-0.05}$	$21.2^{+12.6}_{-7.9}$	67.9 ± 15.0	35 ± 37	$49.4^{+51.9}_{-25.3}$	39.6 ± 10.7	$3.2^{+4.5}_{-1.9} \times 10^{-4}$	$2.3^{+1.3}_{-0.8} \times 10^4$	$1.0^{+1.6}_{-0.6} \times 10^5$
Avg. model $\Sigma_{cl,CB} = 0.34$	#139	138^{+49}_{-36}	0.316	$0.15^{+0.03}_{-0.02}$	$20.8^{+16.9}_{-17.7}$	66.4 ± 14.8	23 ± 32	$79.4^{+11.0}_{-22.5}$	37.6 ± 10.8	$1.9^{+0.7}_{-0.3} \times 10^{-4}$	$2.2^{+0.7}_{-0.7} \times 10^4$	$0.8^{+1.0}_{-0.4} \times 10^5$
W3 p04	0.45	40	3.160	0.03	12.0	43.5	34	17.7	35.0	6.5×10^{-4}	2.1×10^4	4.9×10^4
$d = 1.8\text{ kpc}$	0.45	50	3.160	0.03	12.0	39.2	29	27.7	30.2	7.1×10^{-4}	2.2×10^4	5.1×10^4
$R_{ap} = 11.00''$	0.65	40	3.160	0.03	16.0	54.9	45	10.3	43.6	6.8×10^{-4}	2.4×10^4	1.1×10^5
$R_{ap} = 0.10\text{ pc}$	0.68	60	1.000	0.06	12.0	39.2	10	36.2	31.5	3.1×10^{-4}	2.2×10^4	4.7×10^4
0.72	0.72	50	1.000	0.05	12.0	43.5	4	26.0	35.7	2.8×10^{-4}	1.7×10^4	4.6×10^4
Avg. model	#152	86^{+58}_{-60}	$1.190^{+2.010}_{-0.747}$	$0.06^{+0.06}_{-0.03}$	$21.8^{+14.9}_{-10.3}$	59.6 ± 15.0	28 ± 26	$32.7^{+31.9}_{-11.0}$	43.1 ± 10.8	$4.4^{+4.0}_{-1.1} \times 10^{-4}$	$2.4^{+0.9}_{-0.6} \times 10^4$	$1.2^{+1.7}_{-0.6} \times 10^5$
Avg. model $\Sigma_{cl,CB} = 0.64$	#37	106^{+60}_{-38}	1.000	$0.08^{+0.02}_{-0.02}$	$27.4^{+11.5}_{-12.0}$	60.6 ± 15.1	23 ± 21	$39.0^{+8.6}_{-8.6}$	47.3 ± 10.8	$4.3^{+1.1}_{-0.9} \times 10^{-4}$	$2.4^{+0.6}_{-0.5} \times 10^4$	$1.7^{+2.6}_{-1.0} \times 10^5$
W3 p05	0.15	160	0.100	0.29	12.0	88.6	16	130.2	24.6	7.4×10^{-5}	1.1×10^4	1.9×10^4
$d = 1.8\text{ kpc}$	0.18	160	0.100	0.29	16.0	88.6	44	115.9	31.6	8.1×10^{-5}	1.4×10^4	3.3×10^4
$R_{ap} = 17.50''$	0.19	80	0.316	0.12	16.0	61.6	4	41.6	41.5	1.5×10^{-4}	1.0×10^4	4.2×10^4
$R_{ap} = 0.16\text{ pc}$	0.19	120	0.100	0.25	12.0	79.9	11	88.0	30.3	6.6×10^{-5}	8.1×10^3	1.8×10^4
0.20	0.20	120	0.100	0.25	8.0	71.0	0	101.1	20.8	5.8×10^{-5}	7.1×10^3	1.1×10^4
Avg. model	#1678	83^{+63}_{-36}	$0.516^{+1.207}_{-0.361}$	$0.09^{+0.11}_{-0.05}$	$16.4^{+15.6}_{-8.0}$	53.0 ± 22.4	132 ± 129	$31.1^{+52.5}_{-19.5}$	42.9 ± 16.2	$1.9^{+2.2}_{-0.9} \times 10^{-4}$	$3.2^{+12.5}_{-2.6} \times 10^4$	$5.3^{+14.6}_{-3.9} \times 10^4$
Avg. model $\Sigma_{cl,CB} = 0.44$	#587	103^{+72}_{-42}	0.316	$0.13^{+0.04}_{-0.03}$	$17.6^{+17.5}_{-8.8}$	54.2 ± 21.9	122 ± 128	$41.2^{+55.8}_{-23.7}$	43.5 ± 18.8	$1.4^{+0.6}_{-0.4} \times 10^{-4}$	$3.5^{+14.2}_{-2.7} \times 10^4$	$5.9^{+14.4}_{-3.8} \times 10^4$
W3 p06	2.34	20	1.000	0.03	8.0	71.0	0	4.0	50.7	1.5×10^{-4}	1.6×10^3	1.1×10^4
$d = 1.8\text{ kpc}$	2.35	30	0.316	0.07	8.0	88.6	6	12.3	44.5	7.8×10^{-5}	2.3×10^3	1.2×10^4
$R_{ap} = 5.75''$	2.53	40	0.316	0.08	12.0	88.6	19	10.8	56.7	8.1×10^{-5}	1.7×10^3	2.0×10^4
$R_{ap} = 0.05\text{ pc}$	2.81	20	3.160	0.02	8.0	51.3	64	4.9	44.8	4.0×10^{-4}	4.0×10^3	1.3×10^4
3.02	3.02	40	1.000	0.05	16.0	88.6	56	6.1	60.3	2.0×10^{-4}	2.8×10^3	5.3×10^4
Avg. model	#61	31^{+12}_{-9}	$0.782^{+0.941}_{-0.427}$	$0.05^{+0.03}_{-0.02}$	$11.4^{+5.3}_{-3.6}$	76.1 ± 10.4	71 ± 71	$5.6^{+6.0}_{-2.9}$	53.8 ± 7.1	$1.5^{+1.3}_{-0.7} \times 10^{-4}$	$2.9^{+2.7}_{-1.4} \times 10^3$	$2.5^{+3.4}_{-1.4} \times 10^4$
Avg. model $\Sigma_{cl,CB} = 0.43$	#92	39^{+14}_{-11}	0.316	$0.08^{+0.01}_{-0.01}$	$10.6^{+5.0}_{-3.4}$	53.2 ± 23.0	195 ± 119	$11.2^{+10.7}_{-5.5}$	53.0 ± 11.2	$0.8^{+0.2}_{-0.2} \times 10^{-4}$	$8.7^{+34.6}_{-7.0} \times 10^3$	$1.6^{+2.0}_{-0.9} \times 10^4$

Table B2 continued

Table B2 (continued)

Source	χ^2	M_c (M_\odot)	Σ_{cl} ($g\text{ cm}^{-2}$)	R_c (pc)	m_* (M_\odot)	θ_{view} ($^\circ$)	A_V (mag)	M_{env} (M_\odot)	$\theta_{w,esc}$ (deg)	\dot{M}_{disk} (M_\odot/yr)	$L_{bol,iso}$ (L_\odot)	L_{bol} (L_\odot)
W3 p07	0.52	50	3.160	0.03	12.0	43.5	19	27.7	30.2	7.1×10^{-4}	1.8×10^4	5.1×10^4
$d = 1.8\text{ kpc}$	0.69	40	3.160	0.03	12.0	47.5	35	17.7	35.0	6.5×10^{-4}	1.7×10^4	4.9×10^4
$R_{ap} = 9.75''$	0.71	60	1.000	0.06	12.0	43.5	6	36.2	6	3.1×10^{-4}	1.9×10^4	4.7×10^4
$R_{ap} = 0.09\text{ pc}$	0.76	50	3.160	0.03	16.0	51.3	75	20.5	36.6	7.7×10^{-4}	3.1×10^4	1.1×10^5
	0.92	60	3.160	0.03	12.0	47.5	1	37.8	26.7	7.6×10^{-4}	2.1×10^4	5.0×10^4
Avg. model	#139	86^{+39}_{-27}	$0.700^{+1.181}_{-0.439}$	$0.08^{+0.08}_{-0.04}$	$15.2^{+4.8}_{-3.6}$	65.3 ± 14.7	17 ± 22	$50.7^{+33.3}_{-20.1}$	33.1 ± 6.1	$2.9^{+2.7}_{-1.4} \times 10^{-4}$	$1.9^{+0.6}_{-0.5} \times 10^4$	$5.9^{+4.0}_{-2.4} \times 10^4$
Avg. model $\Sigma_{cl,CB} = 0.60$	#24	77^{+22}_{-17}	1.000	$0.06^{+0.01}_{-0.01}$	$16.9^{+5.9}_{-4.0}$	55.2 ± 12.2	16 ± 16	$40.4^{+11.6}_{-9.0}$	37.1 ± 5.5	$3.7^{+0.6}_{-0.6} \times 10^{-4}$	$2.1^{+0.5}_{-0.4} \times 10^4$	$8.2^{+4.6}_{-3.0} \times 10^4$
W3 p08	1.19	40	3.160	0.03	12.0	51.3	41	17.7	35.0	6.5×10^{-4}	1.5×10^4	4.9×10^4
$d = 1.8\text{ kpc}$	1.23	50	1.000	0.05	12.0	54.9	10	26.0	35.7	2.8×10^{-4}	1.3×10^4	4.6×10^4
$R_{ap} = 15.25''$	1.23	40	1.000	0.05	12.0	77.0	0	15.6	42.4	2.5×10^{-4}	7.8×10^3	4.5×10^4
$R_{ap} = 0.14\text{ pc}$	1.23	80	0.316	0.12	12.0	88.6	2	53.4	30.6	1.4×10^{-4}	1.3×10^4	3.4×10^4
	1.24	80	0.316	0.12	16.0	85.7	11	41.6	41.5	1.5×10^{-4}	9.2×10^3	4.2×10^4
Avg. model	#1884	64^{+45}_{-26}	$0.539^{+1.276}_{-0.379}$	$0.08^{+0.09}_{-0.04}$	$14.0^{+12.7}_{-6.4}$	56.0 ± 22.1	163 ± 142	$22.2^{+35.3}_{-17.6}$	44.5 ± 15.2	$1.7^{+2.7}_{-1.0} \times 10^{-4}$	$1.9^{+5.8}_{-4.8} \times 10^4$	$3.8^{+10.0}_{-7.5} \times 10^4$
Avg. model $\Sigma_{cl,CB} = 0.26$	#434	75^{+29}_{-29}	0.316	$0.11^{+0.02}_{-0.02}$	$14.5^{+6.4}_{-4.4}$	57.5 ± 21.7	141 ± 136	$29.3^{+16.4}_{-10.4}$	44.9 ± 17.2	$1.2^{+0.3}_{-0.3} \times 10^{-4}$	$1.7^{+1.3}_{-1.3} \times 10^4$	$3.4^{+7.5}_{-2.4} \times 10^4$
W3 p09	3.32	40	3.160	0.03	12.0	43.5	1	17.7	35.0	6.5×10^{-4}	2.1×10^4	4.9×10^4
$d = 1.8\text{ kpc}$	3.46	40	3.160	0.03	16.0	54.9	18	10.3	43.6	6.8×10^{-4}	2.4×10^4	1.1×10^5
$R_{ap} = 12.50''$	5.00	60	1.000	0.06	16.0	47.5	5	26.2	41.7	3.2×10^{-4}	2.1×10^4	7.5×10^4
$R_{ap} = 0.11\text{ pc}$	5.28	60	3.160	0.03	24.0	58.3	40	14.7	47.6	8.5×10^{-4}	3.3×10^4	2.2×10^5
	5.73	50	3.160	0.03	12.0	39.2	0	27.7	30.2	7.1×10^{-4}	2.2×10^4	5.1×10^4
Avg. model	#21	55^{+30}_{-19}	$2.538^{+2.036}_{-1.130}$	$0.09^{+0.10}_{-0.01}$	$19.0^{+10.4}_{-6.7}$	54.2 ± 11.3	30 ± 23	$16.2^{+18.8}_{-5.7}$	44.0 ± 7.8	$6.5^{+3.2}_{-2.2} \times 10^{-4}$	$2.8^{+1.0}_{-0.7} \times 10^4$	$1.3^{+1.4}_{-0.7} \times 10^5$
Avg. model $\Sigma_{cl,CB} = 0.14$	#170	59^{+19}_{-14}	0.100	$0.18^{+0.03}_{-0.02}$	$9.9^{+3.1}_{-2.4}$	55.8 ± 22.0	73 ± 128	$29.2^{+18.7}_{-11.4}$	43.5 ± 10.7	$0.4^{+0.1}_{-0.1} \times 10^{-4}$	$0.7^{+1.4}_{-0.5} \times 10^4$	$0.1^{+0.1}_{-0.1} \times 10^5$
W3 p10	0.35	240	0.316	0.20	64.0	79.9	111	48.3	66.1	2.3×10^{-4}	3.2×10^4	6.2×10^5
$d = 1.8\text{ kpc}$	0.35	120	0.316	0.14	24.0	68.0	30	57.1	46.8	1.8×10^{-4}	1.6×10^4	9.3×10^4
$R_{ap} = 18.50''$	0.38	100	0.316	0.13	16.0	54.9	16	61.1	35.9	1.6×10^{-4}	1.5×10^4	4.5×10^4
$R_{ap} = 0.16\text{ pc}$	0.38	120	0.316	0.14	16.0	39.2	58	82.2	32.1	1.8×10^{-4}	2.2×10^4	4.6×10^4
	0.38	100	0.316	0.13	12.0	34.4	52	73.2	26.9	1.5×10^{-4}	2.1×10^4	3.5×10^4
Avg. model	#502	98^{+60}_{-37}	$0.635^{+0.365}_{-0.433}$	$0.09^{+0.10}_{-0.05}$	$19.9^{+12.4}_{-7.7}$	66.1 ± 15.1	46 ± 41	$42.9^{+47.9}_{-22.6}$	40.9 ± 12.0	$2.8^{+3.4}_{-1.5} \times 10^{-4}$	$1.9^{+1.1}_{-0.7} \times 10^4$	$8.8^{+13.4}_{-5.3} \times 10^4$
Avg. model $\Sigma_{cl,CB} = 0.27$	#201	124^{+43}_{-32}	0.316	$0.15^{+0.02}_{-0.02}$	$19.2^{+11.2}_{-7.1}$	66.5 ± 15.6	44 ± 41	$68.0^{+32.5}_{-22.0}$	38.2 ± 12.6	$1.8^{+0.3}_{-0.3} \times 10^{-4}$	$1.9^{+1.0}_{-0.7} \times 10^4$	$6.9^{+8.3}_{-3.8} \times 10^4$
W3 p11	2.43	50	3.160	0.03	8.0	34.4	0	35.1	24.9	6.0×10^{-4}	1.1×10^4	1.7×10^4
$d = 1.8\text{ kpc}$	2.62	50	3.160	0.03	12.0	43.5	36	27.7	30.2	7.1×10^{-4}	1.8×10^4	5.1×10^4
$R_{ap} = 10.50''$	2.94	40	3.160	0.03	12.0	47.5	51	17.7	35.0	6.5×10^{-4}	1.7×10^4	4.9×10^4
$R_{ap} = 0.09\text{ pc}$	3.17	80	0.316	0.12	12.0	88.6	0	53.4	30.6	1.4×10^{-4}	1.3×10^4	3.4×10^4
	3.33	60	3.160	0.03	12.0	39.2	54	37.8	26.7	7.6×10^{-4}	2.6×10^4	5.0×10^4
Avg. model	#37	71^{+29}_{-21}	$0.804^{+1.644}_{-0.540}$	$0.07^{+0.07}_{-0.04}$	$12.4^{+2.1}_{-1.8}$	65.4 ± 18.6	14 ± 21	$43.3^{+26.6}_{-16.5}$	30.9 ± 3.6	$2.8^{+3.0}_{-1.4} \times 10^{-4}$	$1.5^{+0.3}_{-0.3} \times 10^4$	$4.0^{+1.2}_{-0.9} \times 10^4$
Avg. model $\Sigma_{cl,CB} = 0.56$	#94	96^{+25}_{-20}	0.316	$0.13^{+0.02}_{-0.01}$	$14.4^{+3.9}_{-3.1}$	73.2 ± 11.2	13 ± 16	$60.0^{+24.4}_{-17.3}$	34.1 ± 7.7	$1.6^{+0.2}_{-0.2} \times 10^{-4}$	$1.4^{+0.5}_{-0.4} \times 10^4$	$4.2^{+1.8}_{-1.2} \times 10^4$
W3 p12	2.68	40	3.160	0.03	12.0	43.5	0	17.7	35.0	6.5×10^{-4}	2.1×10^4	4.9×10^4
$d = 1.8\text{ kpc}$	3.14	40	3.160	0.03	16.0	54.9	16	10.3	43.6	6.8×10^{-4}	2.4×10^4	1.1×10^5
$R_{ap} = 12.75''$	4.36	50	3.160	0.03	12.0	39.2	0	27.7	30.2	7.1×10^{-4}	2.2×10^4	5.1×10^4
$R_{ap} = 0.11\text{ pc}$	4.37	60	1.000	0.06	16.0	47.5	4	26.2	41.7	3.2×10^{-4}	2.1×10^4	7.5×10^4
	4.40	60	3.160	0.03	24.0	54.9	59	14.7	47.6	8.5×10^{-4}	4.1×10^4	2.2×10^5
Avg. model	#25	56^{+37}_{-22}	$2.397^{+2.370}_{-1.192}$	$0.04^{+0.03}_{-0.02}$	$19.1^{+12.0}_{-4.4}$	54.3 ± 12.8	29 ± 21	$16.9^{+10.8}_{-6.6}$	44.0 ± 9.0	$6.3^{+3.3}_{-2.2} \times 10^{-4}$	$2.8^{+1.9}_{-0.7} \times 10^4$	$1.3^{+1.5}_{-0.7} \times 10^5$
Avg. model $\Sigma_{cl,CB} = 0.21$	#36	159^{+44}_{-44}	0.316	$0.17^{+0.02}_{-0.02}$	$32.5^{+22.3}_{-13.3}$	67.3 ± 17.3	21 ± 22	$62.3^{+10.3}_{-10.3}$	50.1 ± 11.5	$2.1^{+0.3}_{-0.3} \times 10^{-4}$	$2.6^{+0.6}_{-0.6} \times 10^4$	$1.8^{+3.1}_{-3.1} \times 10^5$
W3 p13	0.25	80	3.160	0.04	8.0	22.3	179	64.8	18.8	7.0×10^{-4}	3.1×10^4	1.8×10^4
$d = 1.8\text{ kpc}$	0.27	240	0.100	0.36	16.0	29.0	170	196.8	24.2	9.5×10^{-5}	2.9×10^4	3.5×10^4
$R_{ap} = 26.50''$	0.27	240	0.100	0.36	12.0	22.3	177	210.9	18.9	8.5×10^{-5}	2.8×10^4	2.0×10^4
$R_{ap} = 0.24\text{ pc}$	0.28	240	0.100	0.36	8.0	22.3	61	225.7	13.3	7.1×10^{-5}	1.0×10^4	1.1×10^4

Table B2 continued

Table B2 (continued)

Source	χ^2	M_c (M_\odot)	Σ_{cl} (g cm^{-2})	R_c (pc)	m_* (M_\odot)	θ_{view} ($^\circ$)	A_V (mag)	M_{env} (M_\odot)	$\theta_{w,\text{esc}}$ (deg)	\dot{M}_{disk} (M_\odot/yr)	$L_{\text{bol,iso}}$ (L_\odot)	L_{bol} (L_\odot)
Avg. model	0.29	320	0.100	0.42	8.0	22.3	34	307.3	10.6	7.7×10^{-5}	8.6×10^3	8.8×10^3
	#7525	96^{+153}_{-59}	$0.470^{+1.122}_{-0.331}$	$0.11^{+0.14}_{-0.06}$	$6.4^{+19.2}_{-4.8}$	57.5 ± 21.4	407 ± 301	$59.9^{+143.7}_{-42.3}$	26.4 ± 19.2	$1.4^{+3.3}_{-1.0} \times 10^{-4}$	$6.3^{+69.1}_{-5.8} \times 10^3$	$9.6^{+116.0}_{-8.9} \times 10^3$
Avg. model $\Sigma_{\text{cl,GB}} = 0.21$	#2196	109^{+184}_{-69}	0.316	$0.14^{+0.09}_{-0.05}$	$6.5^{+20.0}_{-4.9}$	57.6 ± 21.3	426 ± 295	$67.2^{+185.4}_{-49.3}$	26.9 ± 20.9	$1.0^{+1.2}_{-0.6} \times 10^{-4}$	$5.7^{+61.5}_{-5.2} \times 10^3$	$8.4^{+98.3}_{-7.7} \times 10^3$
W3 p14	0.58	10	3.160	0.01	1.0	29.0	8	7.9	22.2	1.4×10^{-4}	1.3×10^3	2.0×10^3
$d = 1.8$ kpc	0.67	20	1.000	0.03	4.0	39.2	7	11.2	35.6	1.3×10^{-4}	8.4×10^2	1.7×10^3
$R_{\text{ap}} = 5.00''$	0.70	10	3.160	0.01	2.0	43.5	0	5.7	35.4	1.8×10^{-4}	9.3×10^2	2.6×10^3
$R_{\text{ap}} = 0.04$ pc	0.77	20	3.160	0.02	4.0	39.2	31	11.6	33.6	3.1×10^{-4}	1.6×10^3	3.3×10^3
Avg. model	1.04	20	1.000	0.03	2.0	29.0	0	15.7	24.5	1.0×10^{-4}	9.2×10^2	1.3×10^3
	#148	28^{+17}_{-11}	$0.925^{+1.480}_{-0.569}$	$0.04^{+0.03}_{-0.02}$	$7.4^{+9.0}_{-4.1}$	64.3 ± 17.3	114 ± 118	$7.4^{+10.7}_{-4.4}$	45.3 ± 14.2	$1.5^{+1.7}_{-0.8} \times 10^{-4}$	$2.0^{+3.4}_{-1.3} \times 10^3$	$1.0^{+4.4}_{-0.8} \times 10^4$
Avg. model $\Sigma_{\text{cl,GB}} = 0.79$	#46	30^{+14}_{-10}	1.000	$0.04^{+0.01}_{-0.01}$	$9.7^{+9.1}_{-4.7}$	67.8 ± 17.8	132 ± 93	$6.3^{+9.4}_{-2.6}$	51.5 ± 12.6	$1.7^{+0.3}_{-0.3} \times 10^{-4}$	$2.4^{+2.2}_{-1.2} \times 10^3$	$1.9^{+5.4}_{-1.4} \times 10^4$

NOTE—For each source, the first five rows refer to the best five models taken from the 432 physical models for the non-restricted Σ_{cl} case. The sixth row shows the average and dispersion of good model fits (see the text) for the non-restricted Σ_{cl} case. The seventh row shows the average and dispersion of good models for the restricted $\Sigma_{\text{cl,GB}}$ case. The number next to the symbol # represents the number of models considered in the average of the good models. Upper and lower scripts in the average model rows refer to the upper and lower range of the dispersion of the good models.

C. SOMA I-IV SED FITS

Here we present the results of the SED fitting for the sources in the SOMA I-IV sample using the updated definition of “good” models. Table ?? presents the best

models including the $\Sigma_{\text{cl,GB}}$ restricted models. Figure C1 contains the source SEDs and “good” model fits (see main text for details), and Figure C2 presents the “good” model distributions in the $\Sigma_{\text{cl}} - M_c$, $m_* - M_c$, and $m_* - \Sigma_{\text{cl}}$ planes.

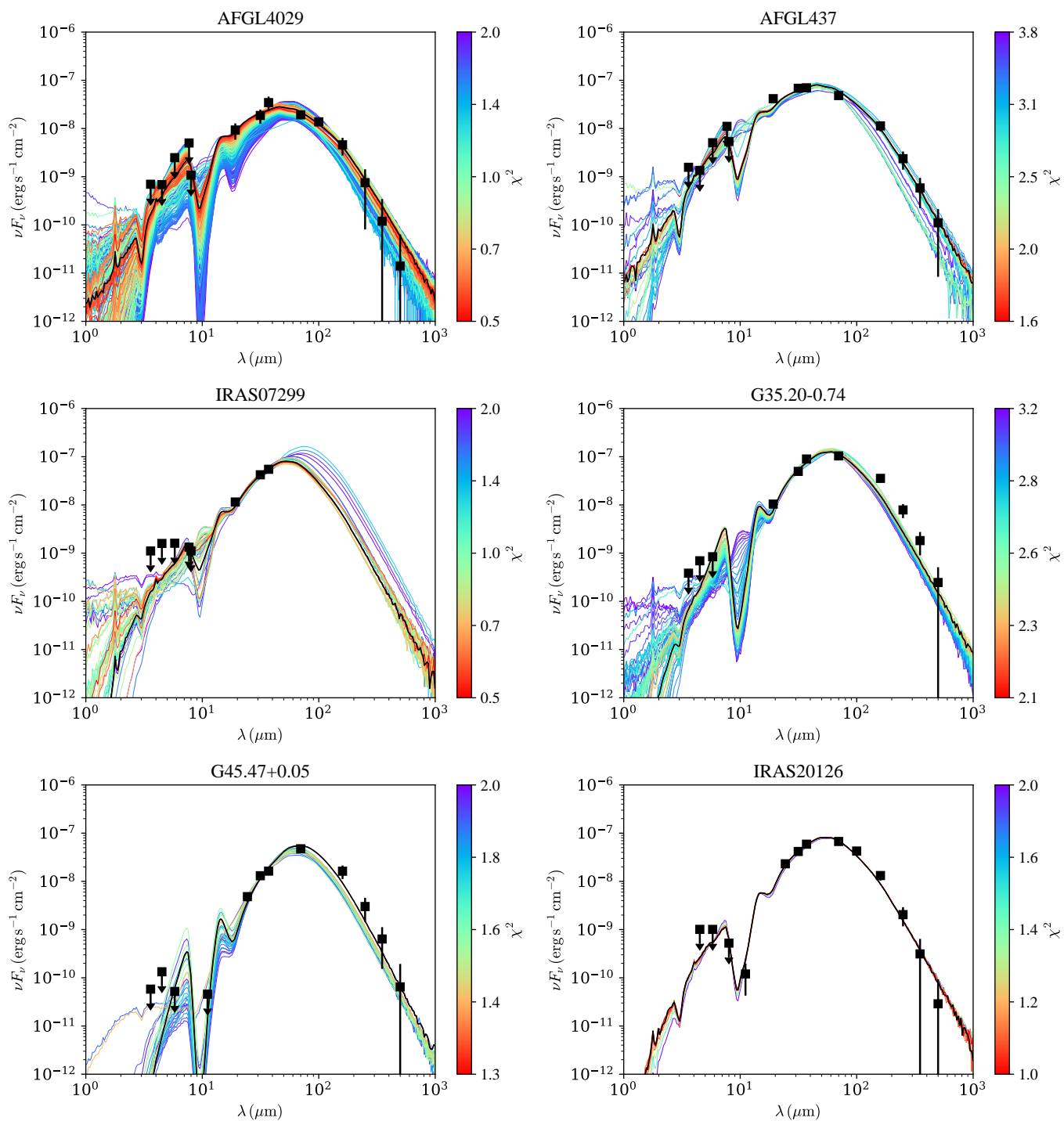


Figure C1. SOMA I-IV sources reanalyzed with *sedcreator* and the new definition of "good" model. The resulting model parameters are listed in Table ??.

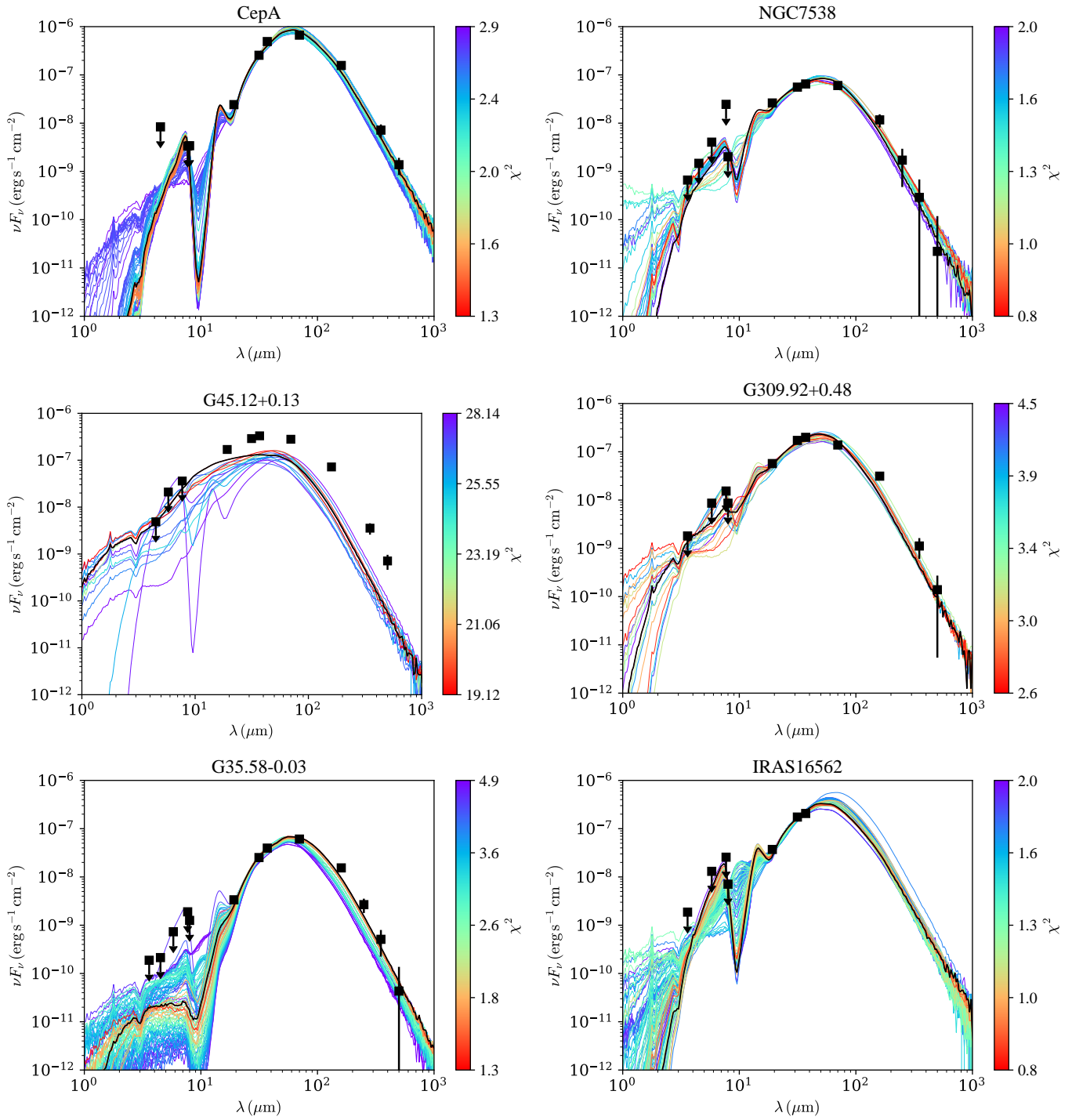


Figure C1. (Continued.)

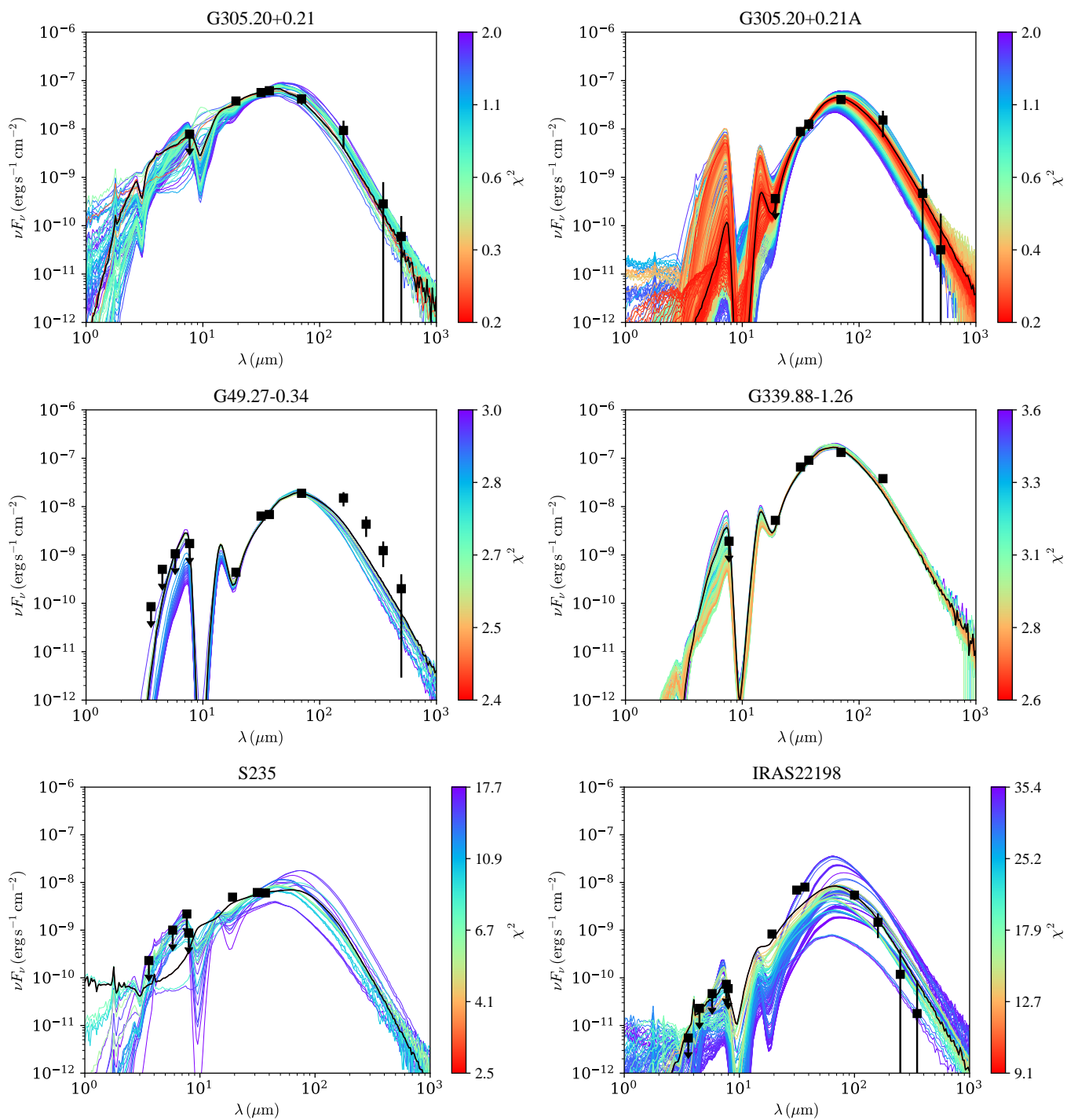


Figure C1. (Continued.)

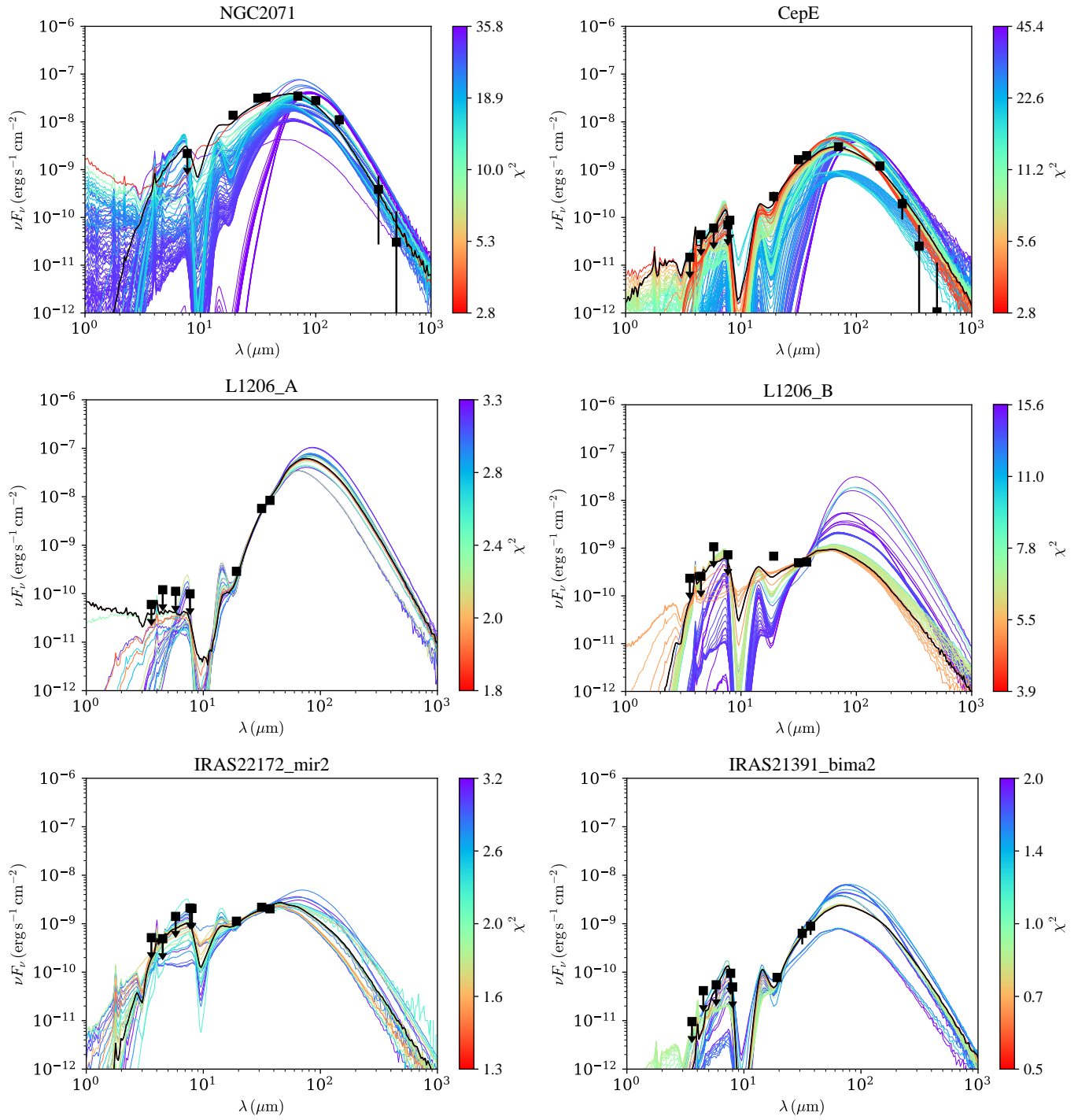


Figure C1. (Continued.)

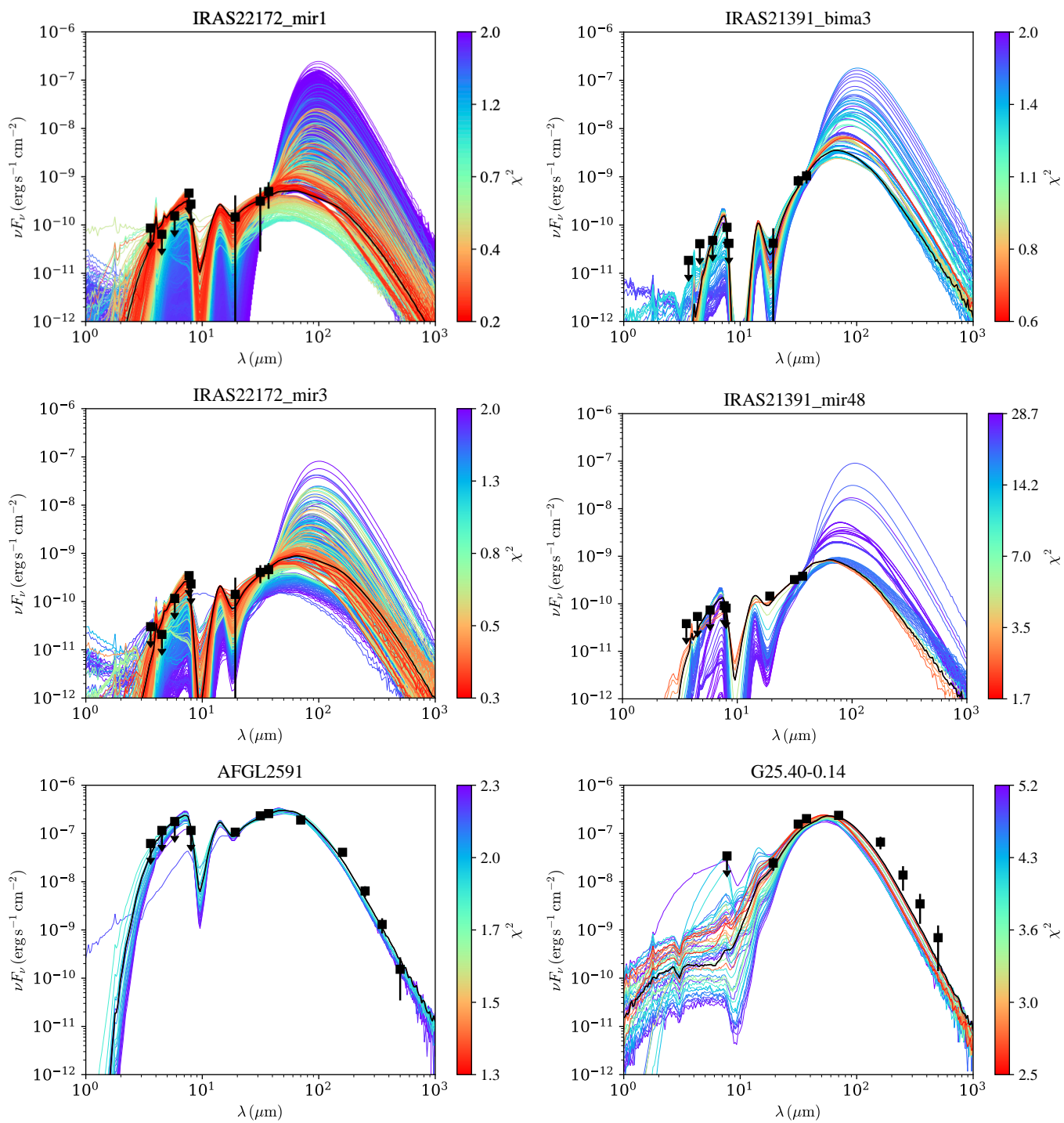


Figure C1. (Continued.)

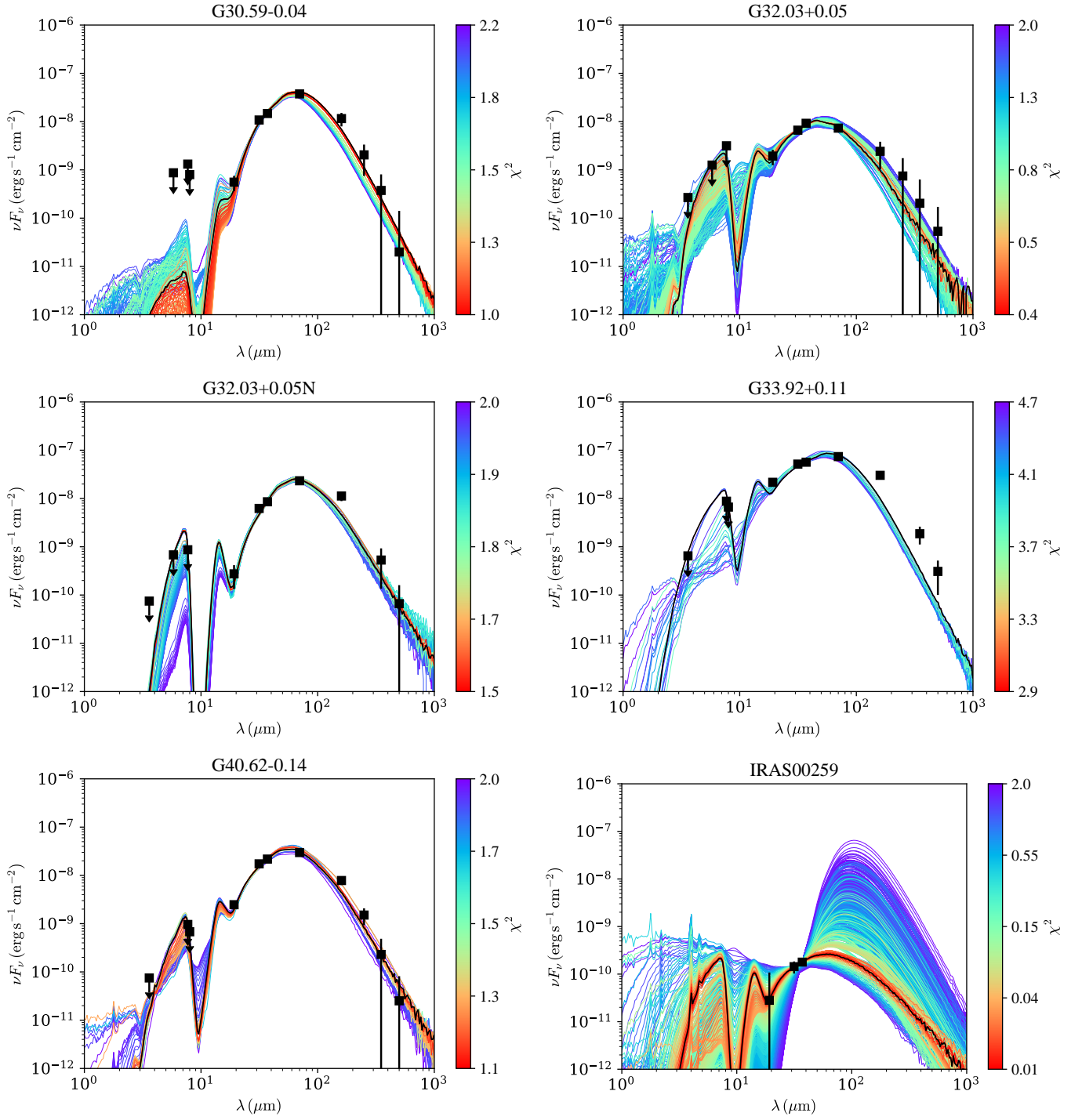


Figure C1. (Continued.)

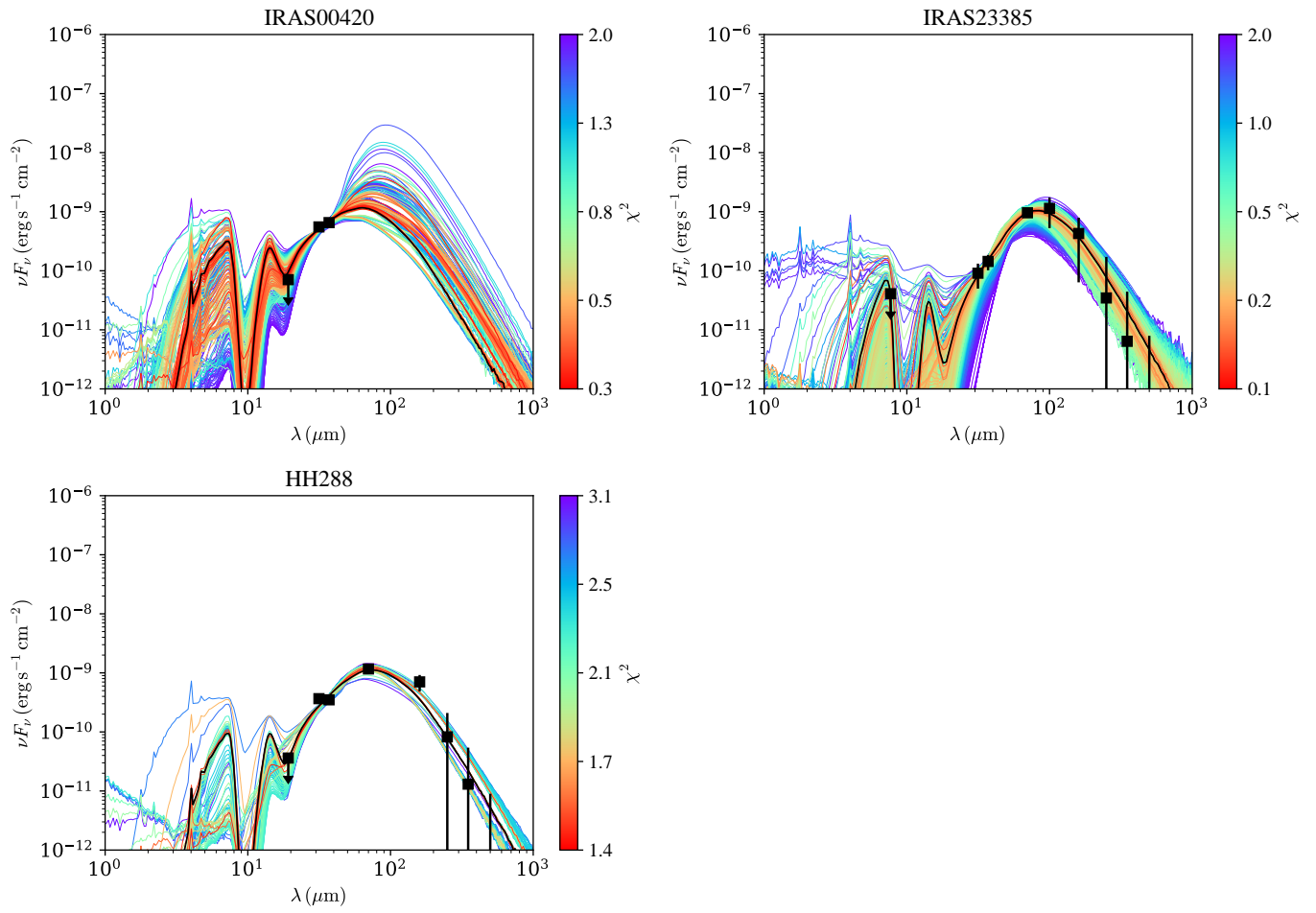


Figure C1. (Continued.)

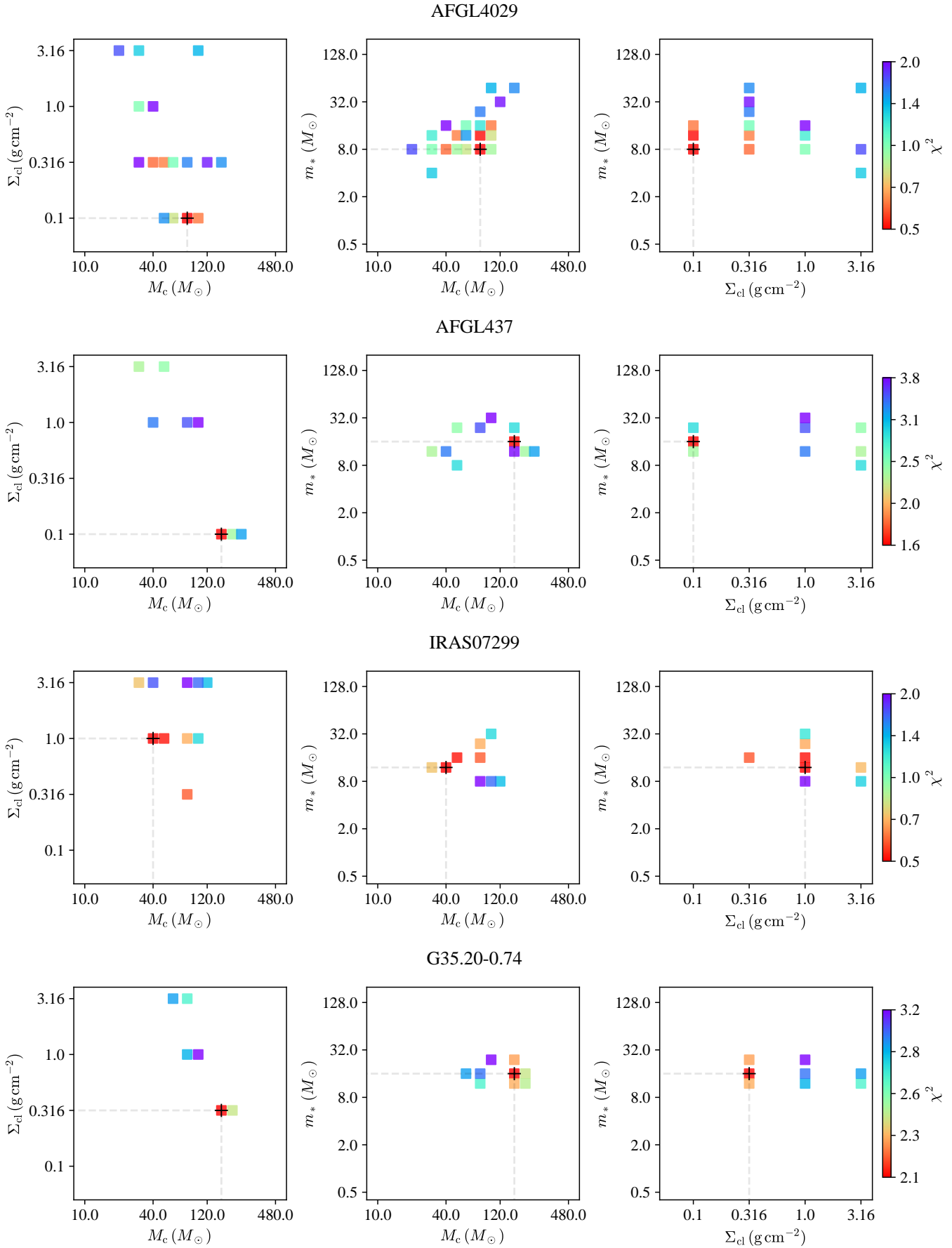
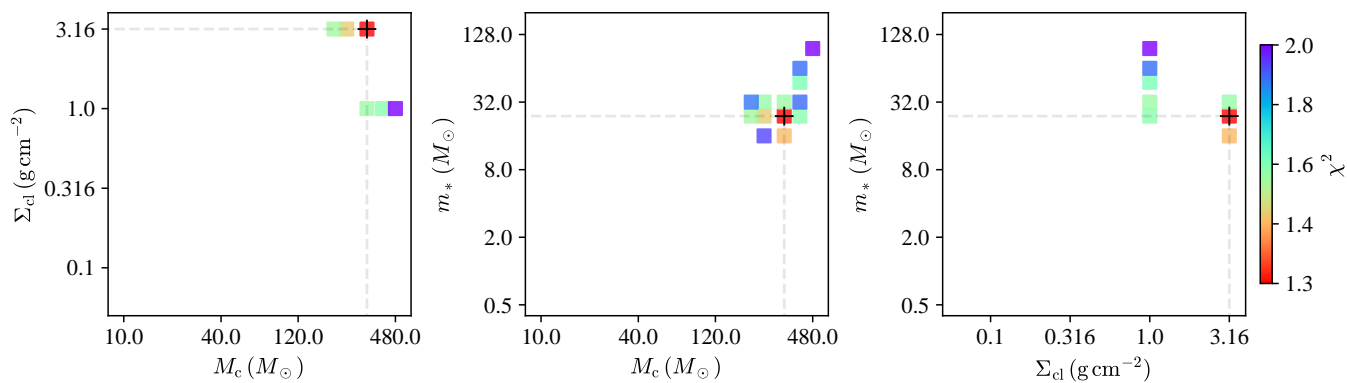
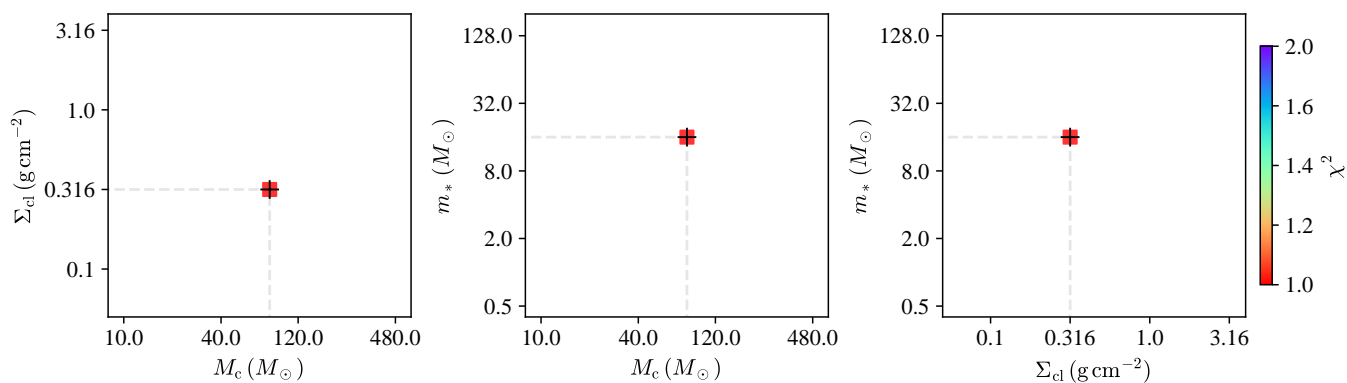


Figure C2. Diagrams of χ^2 distribution in $\Sigma_{\text{cl}} - M_c$ space (left), $m_* - M_c$ space (center) and $m_* - \Sigma_{\text{cl}}$ space (right) for each source noted on top of each plot. The black cross is the best model.

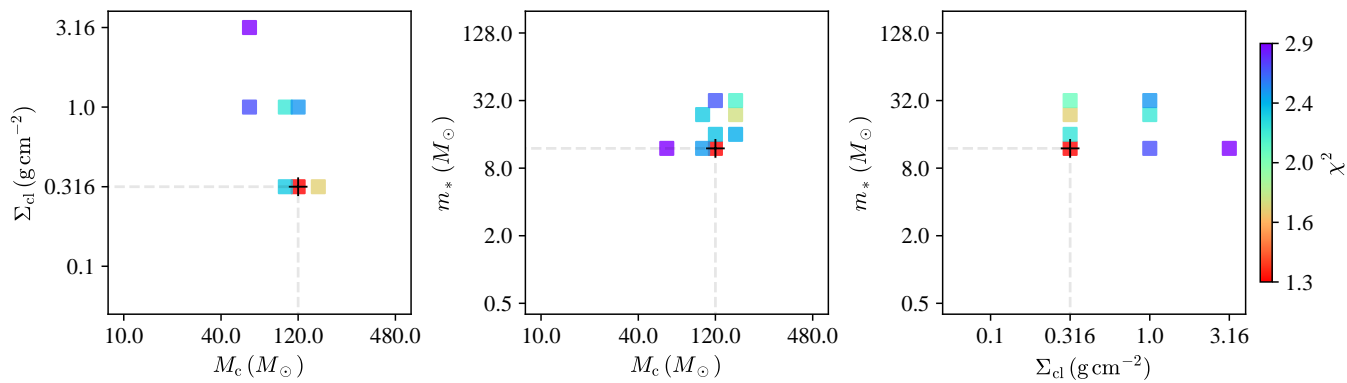
G45.47+0.05



IRAS20126



CepA



NGC7538

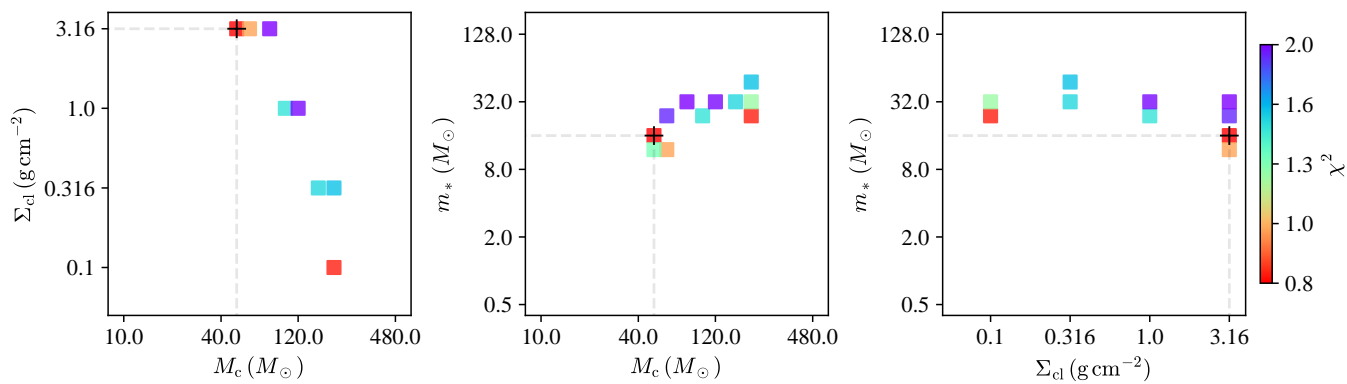
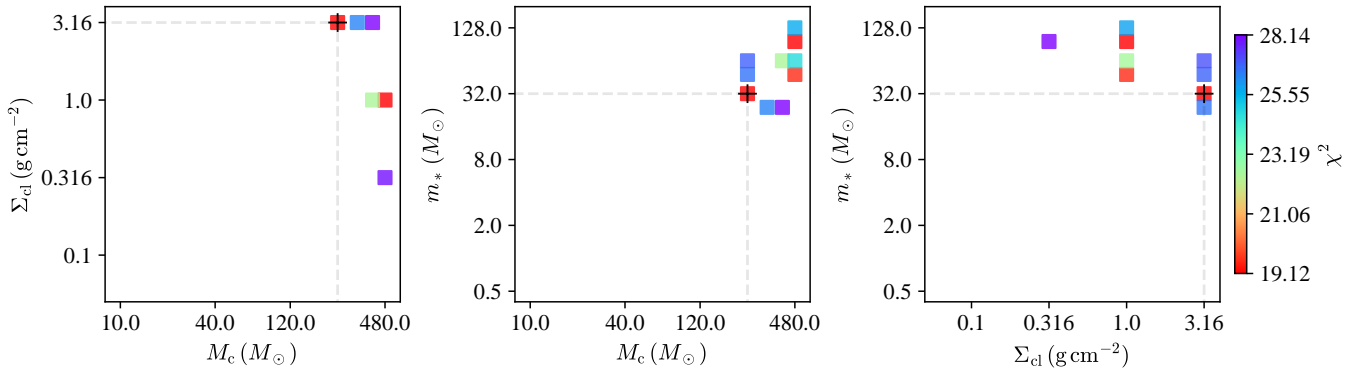
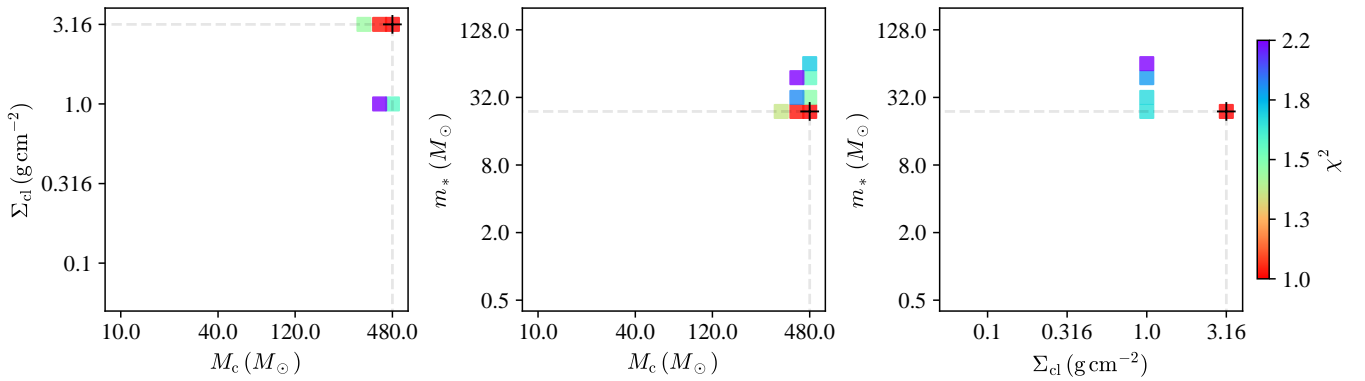


Figure C2. (Continued.)

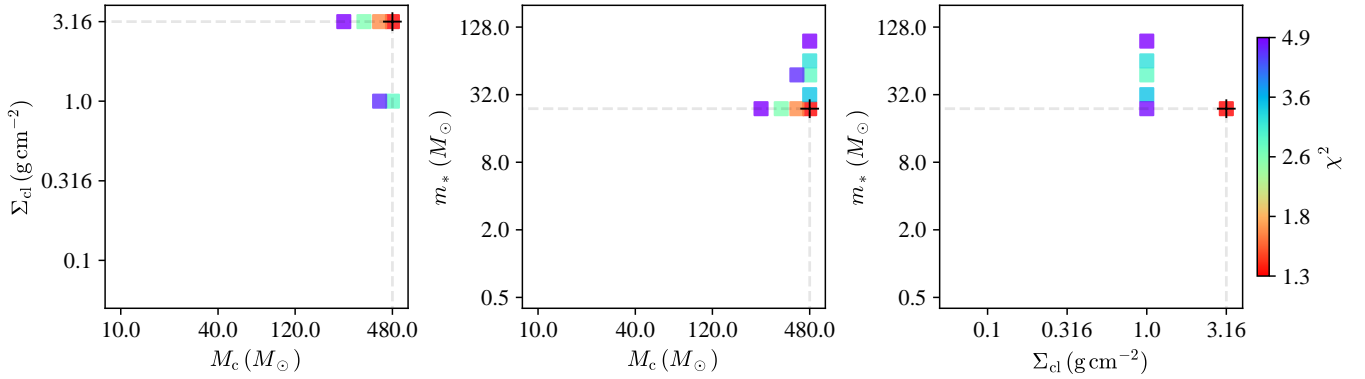
G45.12+0.13



G30.59-0.04



G35.58-0.03



IRAS16562

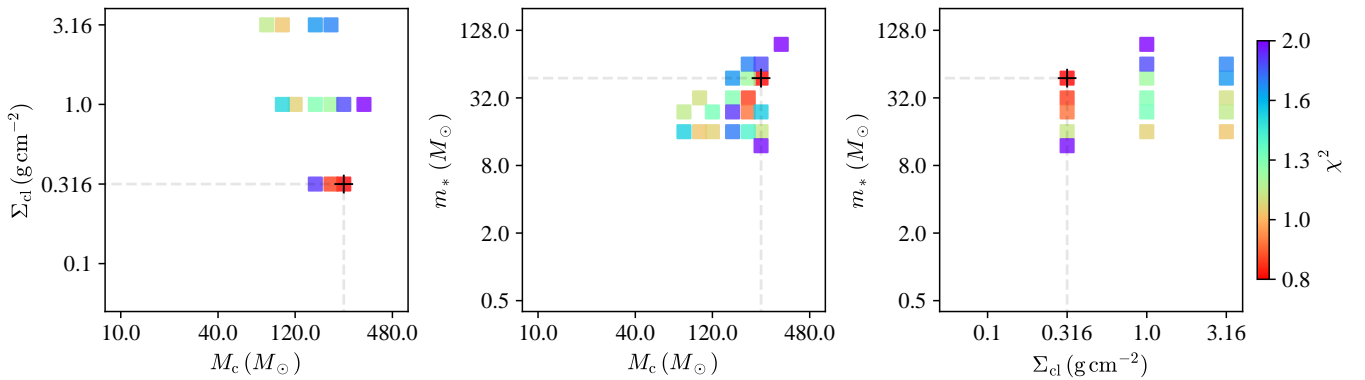
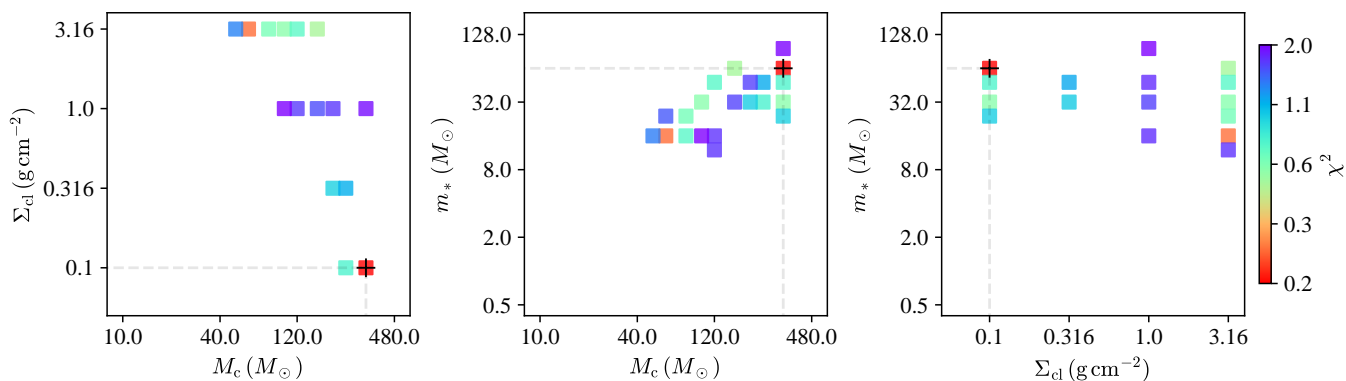
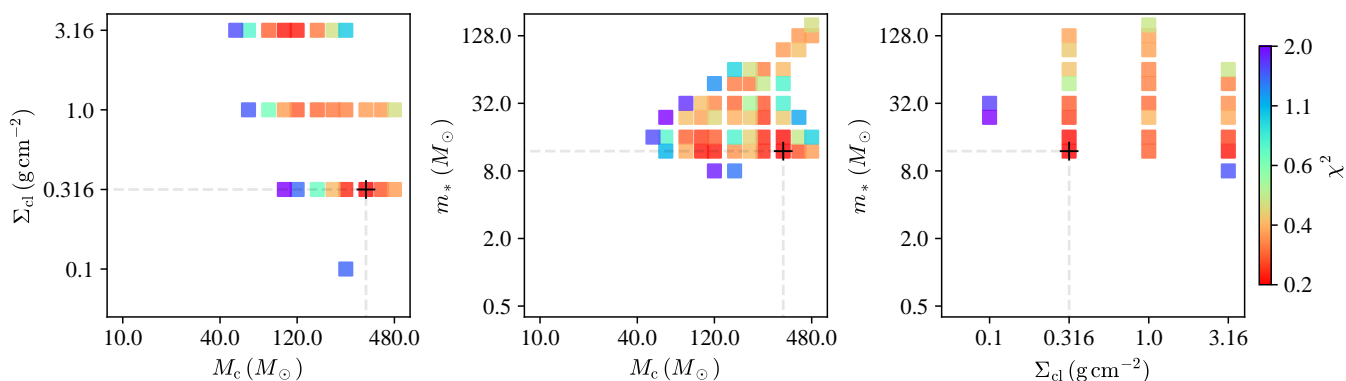


Figure C2. (Continued.)

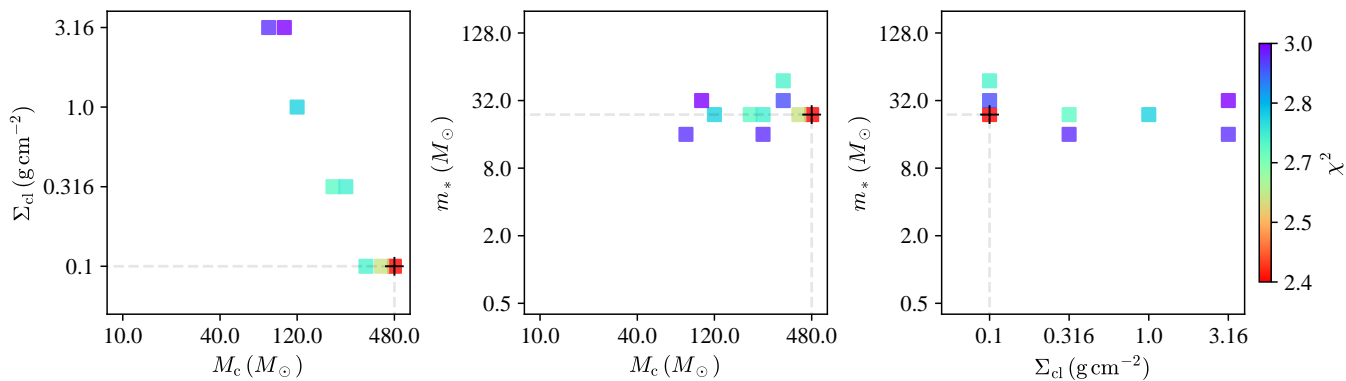
G305.20+0.21



G305.20+0.21A



G49.27-0.34



G339.88-1.26

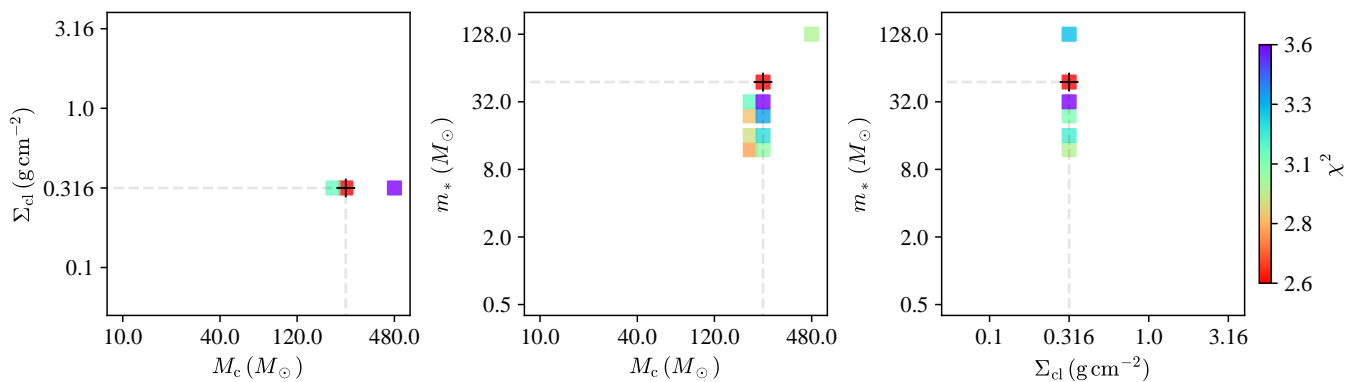
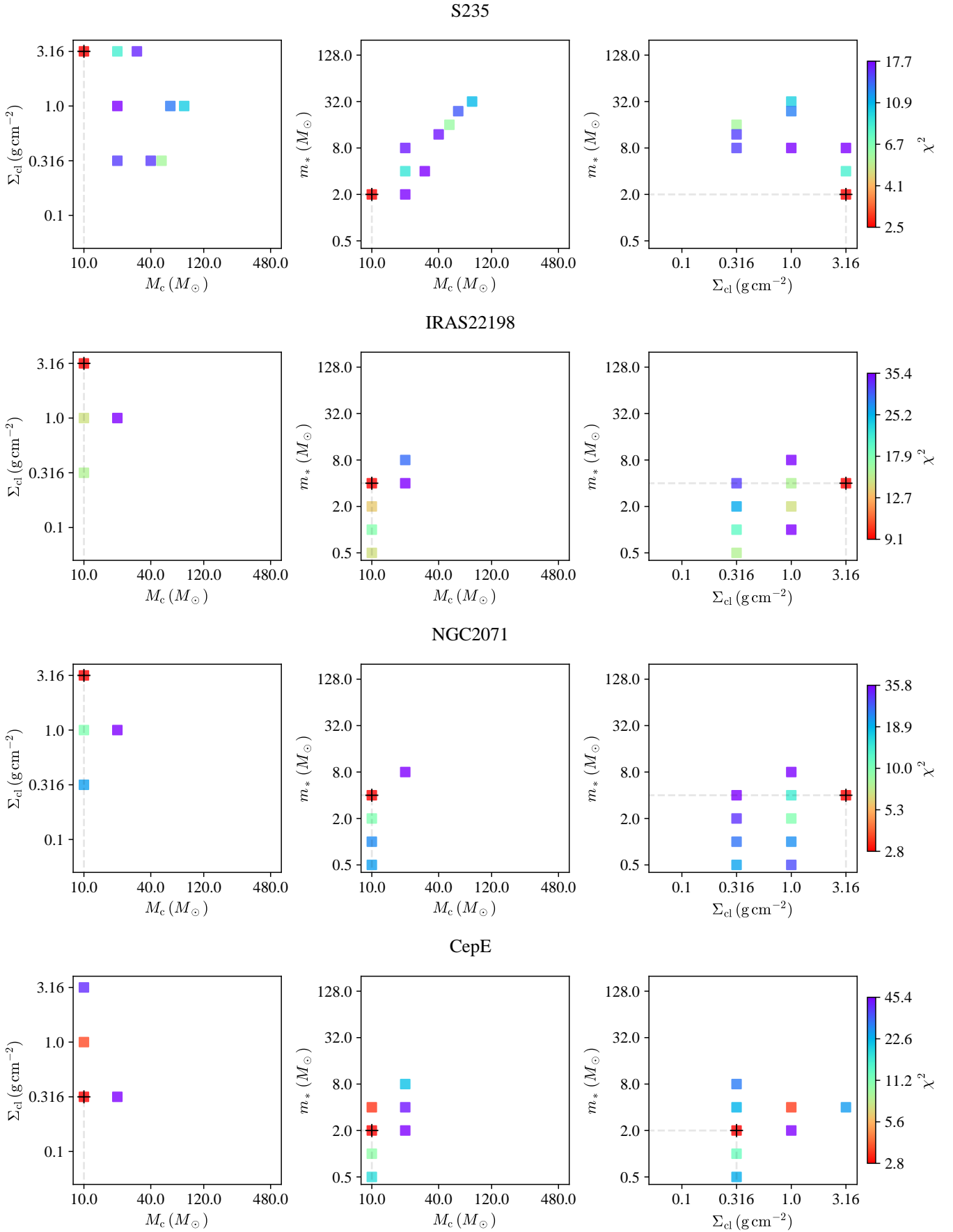


Figure C2. (Continued.)

**Figure C2.** (Continued.)

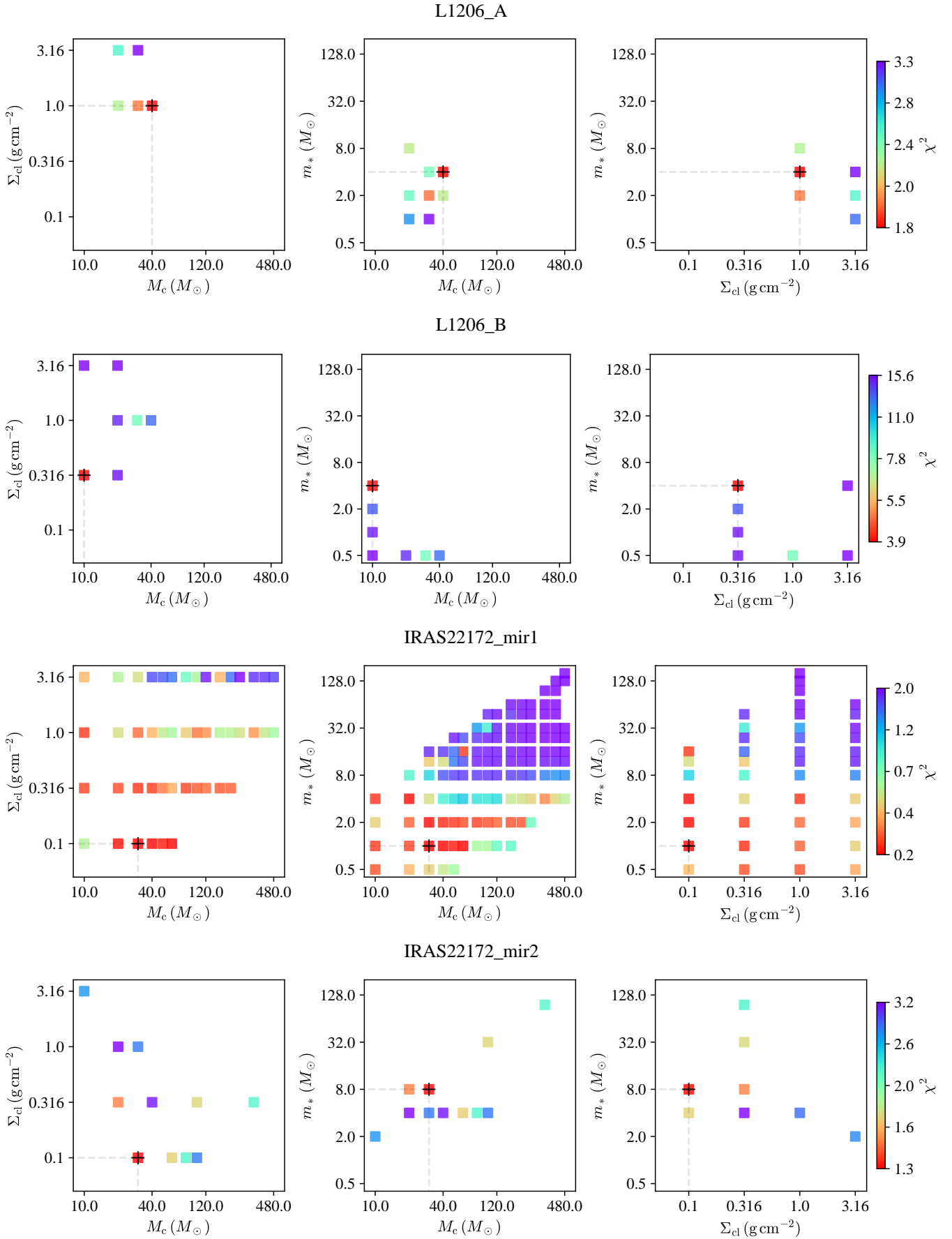
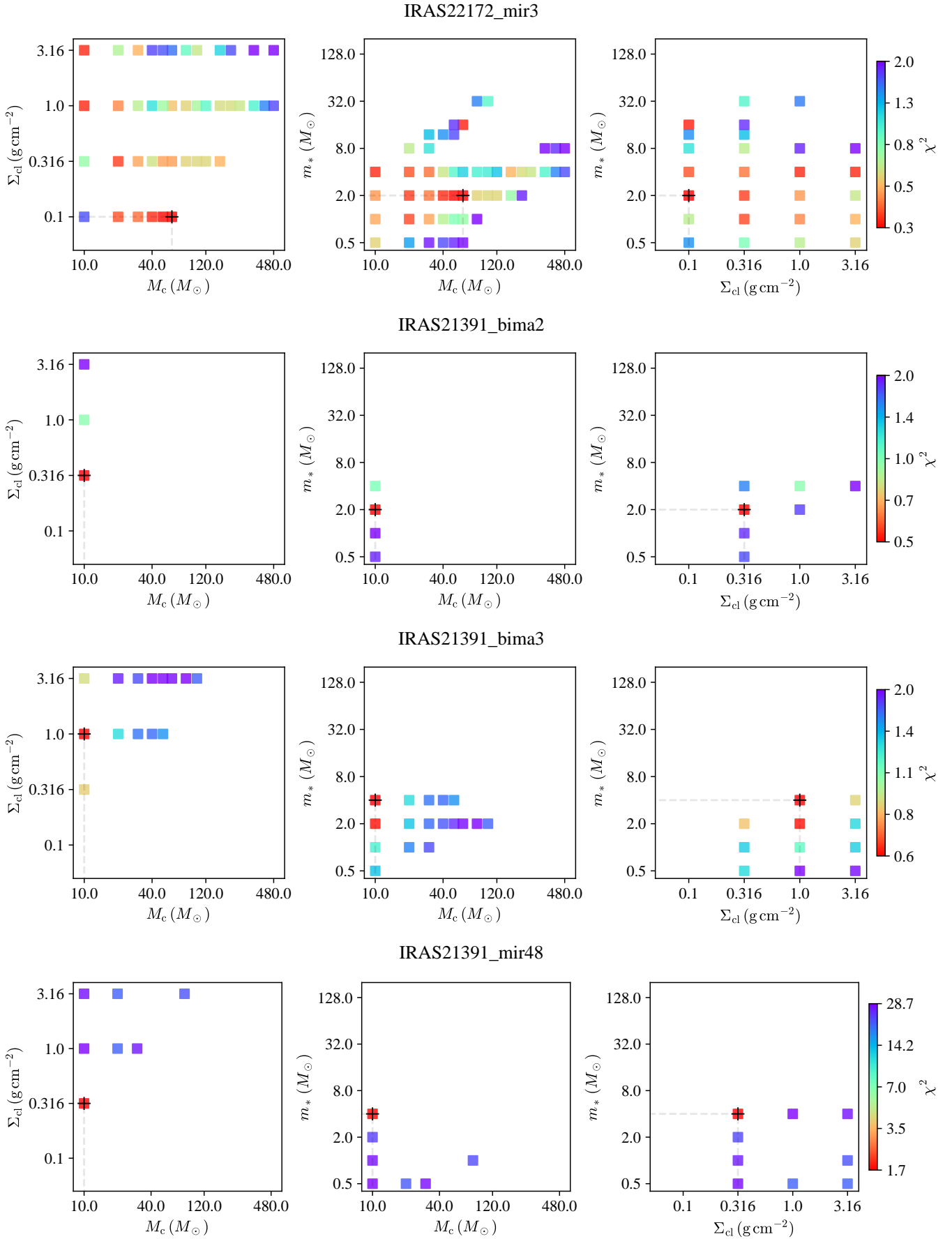


Figure C2. (Continued.)

**Figure C2.** (Continued.)

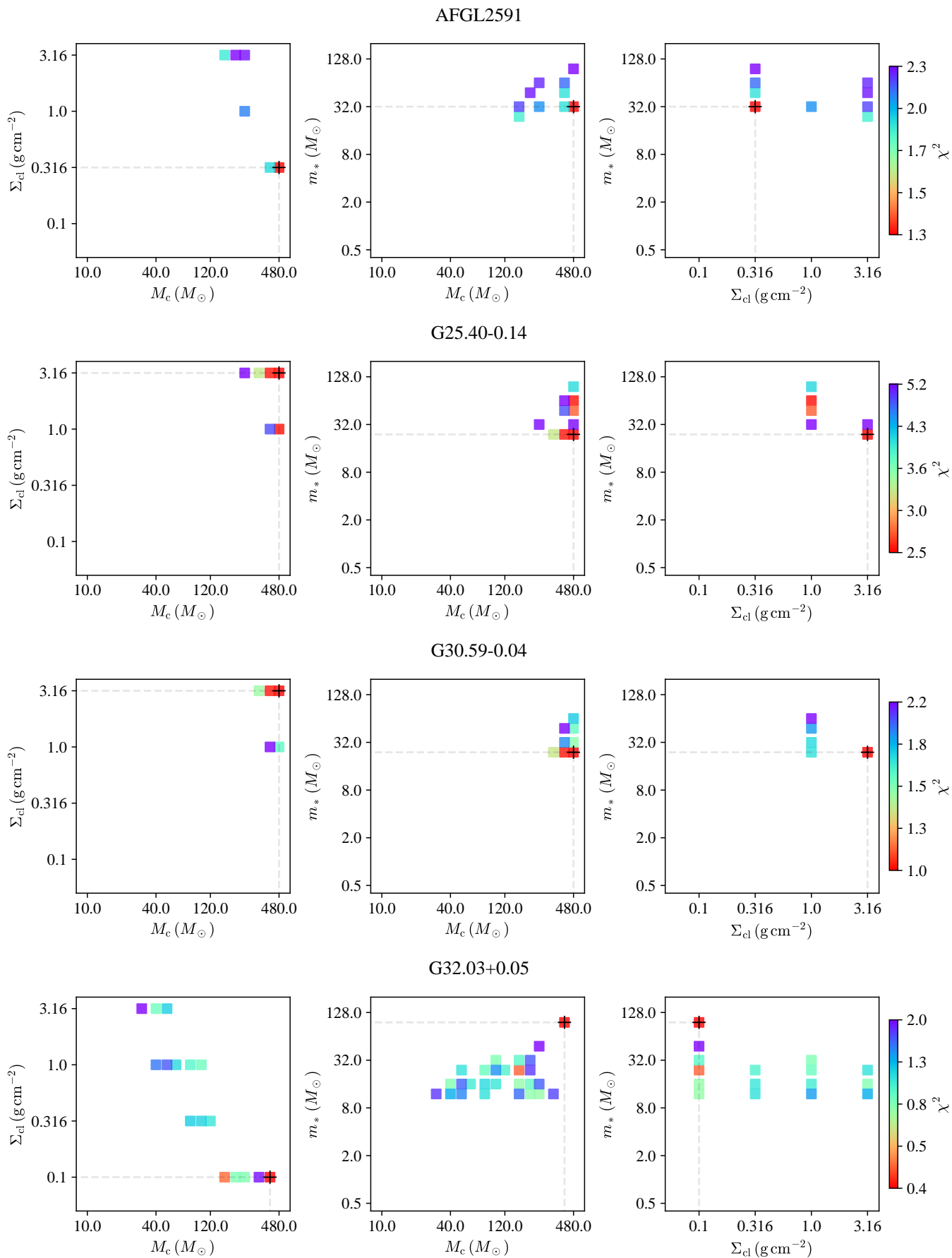


Figure C2. (Continued.)

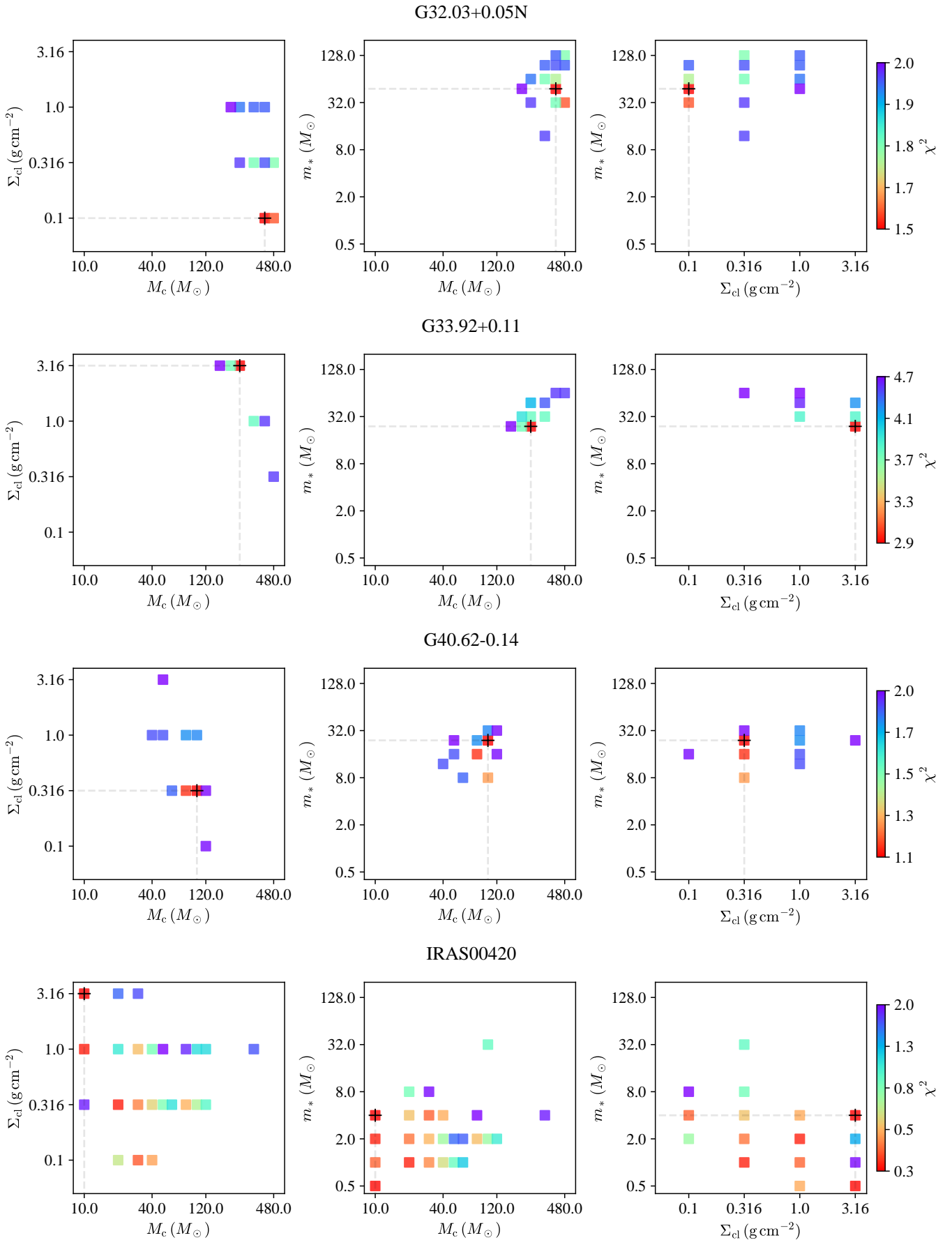
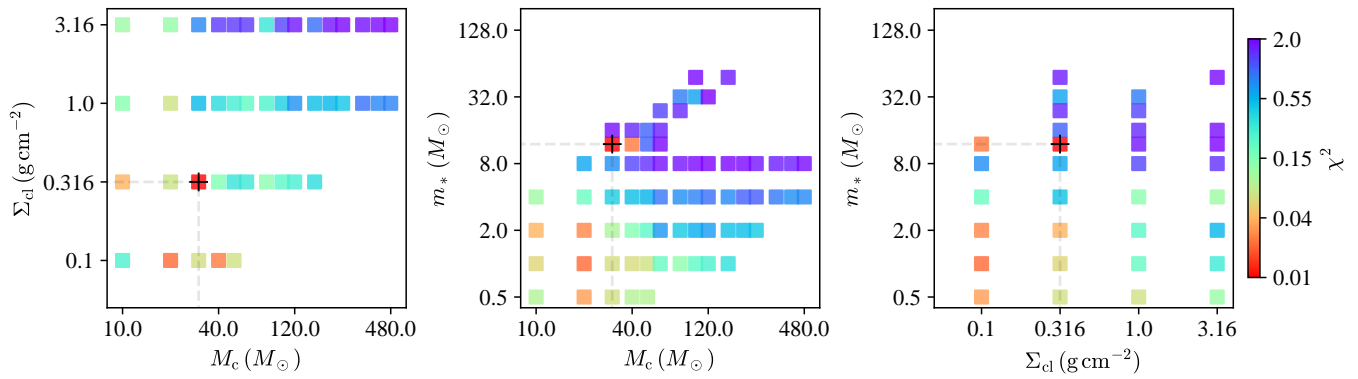
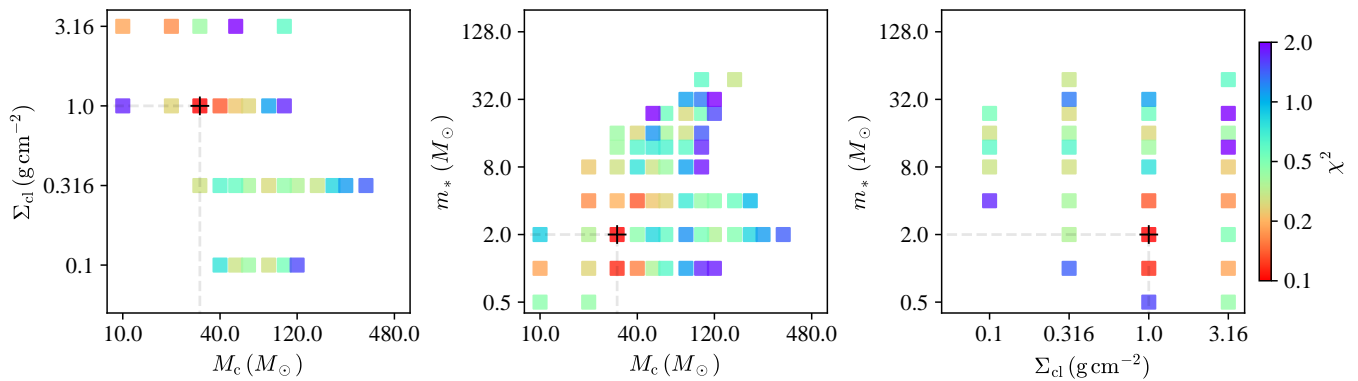


Figure C2. (Continued.)

IRAS00259



IRAS23385



HH288

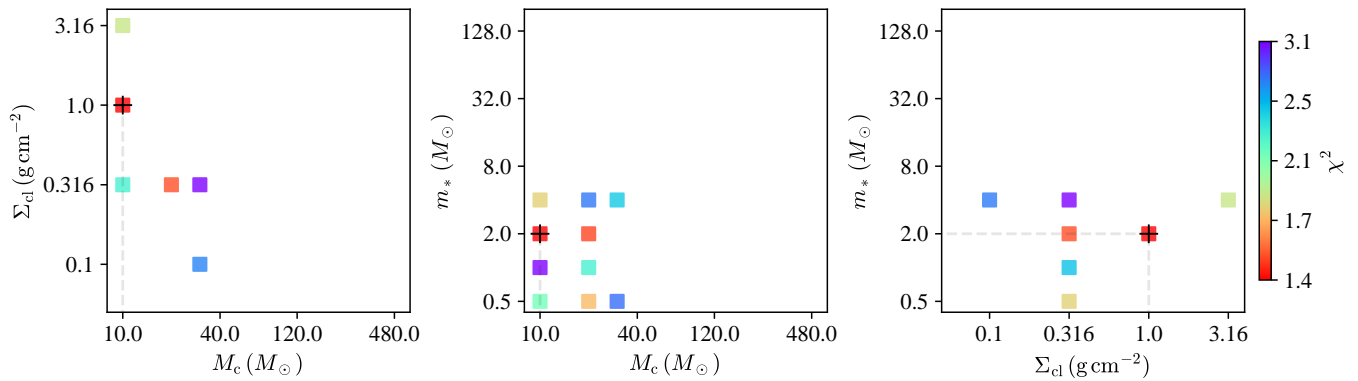


Figure C2. (Continued.)

Table C3. Parameters of the Best Five Fitted Models and Average and Dispersion of Good Models for SOMA I-IV

Source	χ^2	M_c (M_\odot)	Σ_{cl} (g cm^{-2})	R_c (pc)	m_* (M_\odot)	θ_{view} ($^\circ$)	A_V (mag)	M_{env} (M_\odot)	$\theta_{w, \text{esc}}$ (deg)	\dot{M}_{disk} (M_\odot/yr)	$L_{\text{bol, iso}}$ (L_\odot)	L_{bol} (L_\odot)
SOMA I												
AFGL4029	0.46	80	0.100	0.21	8.0	64.8	1	61.5	26.8	5.0×10^{-5}	5.4×10^3	9.7×10^3
$d = 2.0$ kpc	0.47	80	0.100	0.21	12.0	71.0	4	46.5	40.0	5.4×10^{-5}	5.0×10^3	1.6×10^4
$R_{\text{ap}} = 12.75''$	0.56	40	0.316	0.08	8.0	43.5	0	22.3	36.3	9.2×10^{-5}	5.0×10^3	1.2×10^4
$R_{\text{ap}} = 0.12$ pc	0.57	100	0.100	0.23	16.0	71.0	43	53.0	44.7	6.2×10^{-5}	7.8×10^3	3.0×10^4
Avg. model	0.58	50	0.316	0.09	12.0	58.3	0	21.6	46.3	1.0×10^{-4}	4.8×10^3	2.4×10^4
Avg. model $\Sigma_{\text{cl, GB}} = 0.38$	#270	64^{+22}_{-22}	$0.214^{+0.321}_{-0.129}$	$0.13^{+0.11}_{-0.06}$	$11.3^{+6.0}_{-3.9}$	58.9 ± 21.4	55 ± 69	$30.3^{+24.3}_{-16.1}$	40.7 ± 12.1	$8.4^{+3.7}_{-1.0} \times 10^{-5}$	$8.8^{+5.0}_{-2.5} \times 10^3$	$2.0^{+2.5}_{-1.5} \times 10^4$
Avg. model $\Sigma_{\text{cl, GB}} = 0.14$	#102	55^{+20}_{-15}	0.316	$0.10^{+0.02}_{-0.01}$	$12.0^{+7.0}_{-4.4}$	57.7 ± 22.8	61 ± 80	$23.4^{+7.6}_{-5.9}$	44.7 ± 12.4	$10.4^{+1.1}_{-1.0} \times 10^{-5}$	$9.6^{+22.5}_{-6.7} \times 10^3$	$2.4^{+3.1}_{-1.4} \times 10^4$
AFGL437	1.59	160	0.100	0.29	16.0	68.0	0	115.9	31.6	8.1×10^{-5}	1.5×10^4	3.3×10^4
$d = 2.0$ kpc	2.28	30	3.160	0.02	12.0	47.5	28	7.5	43.0	5.5×10^{-4}	2.0×10^4	4.9×10^4
$R_{\text{ap}} = 29.50''$	2.33	200	0.100	0.33	12.0	39.2	0	174.1	20.5	8.0×10^{-5}	1.5×10^4	2.0×10^4
$R_{\text{ap}} = 0.29$ pc	2.39	50	3.160	0.03	24.0	64.8	27	5.5	56.4	6.8×10^{-4}	2.0×10^4	1.9×10^5
Avg. model	2.85	160	0.100	0.29	24.0	85.7	26	86.6	44.7	8.5×10^{-5}	1.9×10^4	7.8×10^4
Avg. model	#39	115^{+96}_{-52}	$0.265^{+0.930}_{-0.206}$	$0.15^{+0.28}_{-0.10}$	$17.3^{+6.4}_{-4.7}$	63.5 ± 16.4	11 ± 13	$53.9^{+135.9}_{-38.6}$	38.0 ± 11.9	$1.5^{+2.1}_{-0.9} \times 10^{-4}$	$1.6^{+0.3}_{-0.2} \times 10^4$	$5.1^{+6.1}_{-2.8} \times 10^4$
Avg. model $\Sigma_{\text{cl, GB}} = 0.14$	#100	186^{+40}_{-33}	0.100	$0.32^{+0.03}_{-0.03}$	$15.3^{+5.9}_{-4.3}$	64.4 ± 16.4	12 ± 20	$136.5^{+61.6}_{-42.5}$	29.0 ± 11.1	$0.8^{+0.1}_{-0.1} \times 10^{-4}$	$1.6^{+0.4}_{-0.3} \times 10^4$	$3.2^{+2.9}_{-1.5} \times 10^4$
IRAS07299	0.53	40	1.000	0.05	12.0	51.3	37	15.6	42.4	2.5×10^{-4}	1.1×10^4	4.5×10^4
$d = 1.7$ kpc	0.54	50	1.000	0.05	16.0	61.6	16	16.2	48.3	2.8×10^{-4}	9.2×10^3	6.7×10^4
$R_{\text{ap}} = 7.50''$	0.61	80	0.316	0.12	16.0	68.0	14	41.6	41.5	1.5×10^{-4}	4.2×10^3	4.2×10^4
$R_{\text{ap}} = 0.06$ pc	0.72	80	1.000	0.07	24.0	68.0	20	25.1	52.0	3.5×10^{-4}	1.1×10^4	1.2×10^5
Avg. model	0.75	30	3.160	0.02	12.0	51.3	74	7.5	43.0	5.5×10^{-4}	1.5×10^4	4.9×10^4
Avg. model	#47	61^{+35}_{-22}	$1.103^{+1.415}_{-0.620}$	$0.05^{+0.04}_{-0.02}$	$16.0^{+7.7}_{-5.2}$	66.1 ± 17.1	19 ± 21	$22.3^{+22.9}_{-11.3}$	43.9 ± 10.1	$3.3^{+2.2}_{-1.3} \times 10^{-4}$	$1.0^{+0.2}_{-0.2} \times 10^4$	$6.1^{+5.7}_{-2.9} \times 10^4$
Avg. model $\Sigma_{\text{cl, GB}} = \dots$	\dots	\dots	\dots	\dots	\dots	\dots	\dots	\dots	\dots	\dots	\dots	\dots
SOMA II												
G35.20-0.74	2.06	160	0.316	0.17	16.0	34.4	48	124.7	25.9	2.0×10^{-4}	3.0×10^4	5.0×10^4
$d = 2.2$ kpc	2.26	160	0.316	0.17	24.0	51.3	58	97.6	37.2	2.2×10^{-4}	3.1×10^4	9.9×10^4
$R_{\text{ap}} = 18.75''$	2.29	160	0.316	0.17	12.0	29.0	29	135.3	19.8	1.8×10^{-4}	2.8×10^4	3.8×10^4
$R_{\text{ap}} = 0.20$ pc	2.41	200	0.316	0.19	16.0	29.0	64	162.5	22.5	2.2×10^{-4}	3.7×10^4	5.3×10^4
Avg. model	2.43	200	0.316	0.19	12.0	22.3	61	172.7	17.3	1.9×10^{-4}	3.5×10^4	4.0×10^4
Avg. model	#72	120^{+64}_{-42}	$0.639^{+1.122}_{-0.407}$	$0.10^{+0.11}_{-0.05}$	$16.0^{+4.4}_{-3.8}$	59.0 ± 17.2	28 ± 28	$80.9^{+63.9}_{-35.7}$	28.4 ± 6.5	$3.1^{+2.7}_{-1.4} \times 10^{-4}$	$2.8^{+0.5}_{-0.7} \times 10^4$	$6.6^{+3.7}_{-1.4} \times 10^4$
Avg. model $\Sigma_{\text{cl, GB}} = 0.77$	#54	108^{+34}_{-24}	1.000	$0.08^{+0.01}_{-0.01}$	$24.6^{+8.8}_{-8.8}$	62.0 ± 15.7	28 ± 29	$48.5^{+8.1}_{-8.1}$	42.5 ± 10.4	$4.4^{+0.6}_{-0.6} \times 10^{-4}$	$2.5^{+0.5}_{-0.5} \times 10^4$	$14.8^{+7.3}_{-4.3} \times 10^4$
G45.47+0.05	1.27	320	3.160	0.07	24.0	22.3	178	276.8	15.2	1.8×10^{-3}	3.3×10^5	3.1×10^5
$d = 8.4$ kpc	1.42	320	3.160	0.07	16.0	22.3	3	293.1	11.6	1.4×10^{-3}	1.0×10^5	1.1×10^5
$R_{\text{ap}} = 15.00''$	1.45	240	3.160	0.06	24.0	29.0	156	194.5	18.2	1.6×10^{-3}	2.6×10^5	3.1×10^5
$R_{\text{ap}} = 0.61$ pc	1.53	200	3.160	0.06	24.0	29.0	240	155.5	20.0	1.5×10^{-3}	2.6×10^5	3.1×10^5
Avg. model	1.54	320	1.000	0.13	32.0	29.0	125	252.3	24.3	8.2×10^{-4}	2.0×10^5	2.7×10^5
Avg. model	#31	269^{+74}_{-58}	$2.348^{+1.569}_{-0.941}$	$0.08^{+0.03}_{-0.02}$	$28.8^{+12.0}_{-8.5}$	37.3 ± 9.7	133 ± 47	$207.1^{+157.6}_{-57.1}$	21.6 ± 6.1	$1.4^{+0.5}_{-0.4} \times 10^{-3}$	$2.2^{+0.9}_{-1.4} \times 10^5$	$3.5^{+2.4}_{-1.4} \times 10^5$
Avg. model $\Sigma_{\text{cl, GB}} = 0.57$	#21	395^{+67}_{-58}	1.000	$0.15^{+0.01}_{-0.01}$	$43.9^{+29.3}_{-17.6}$	37.5 ± 9.9	134 ± 51	$276.9^{+57.6}_{-47.7}$	28.5 ± 9.6	$1.0^{+0.2}_{-0.2} \times 10^{-3}$	$2.3^{+1.0}_{-0.7} \times 10^5$	$4.7^{+5.4}_{-2.5} \times 10^5$
IRAS20126	1.00	80	0.316	0.12	16.0	82.8	17	41.6	41.5	1.5×10^{-4}	9.2×10^3	4.2×10^4
$d = 1.6$ kpc	2.16	40	3.160	0.03	16.0	54.9	130	10.3	43.6	6.8×10^{-4}	2.4×10^4	1.1×10^5
$R_{\text{ap}} = 12.75''$	2.19	120	0.316	0.14	24.0	77.0	66	57.1	46.8	1.8×10^{-4}	1.5×10^4	9.3×10^4
$R_{\text{ap}} = 0.10$ pc	2.57	100	0.316	0.13	16.0	58.3	55	61.1	35.9	1.6×10^{-4}	1.4×10^4	4.5×10^4
Avg. model	2.59	80	0.316	0.12	12.0	51.3	62	53.4	30.6	1.4×10^{-4}	1.5×10^4	3.4×10^4
Avg. model	#9	80^{+0}_{-0}	$0.316^{+0.000}_{-0.000}$	$0.12^{+0.00}_{-0.00}$	$16.0^{+0.0}_{-0.0}$	76.9 ± 7.6	23 ± 7	$41.6^{+0.0}_{-0.0}$	41.5 ± 0.0	$1.5^{+0.0}_{-0.0} \times 10^{-4}$	$9.4^{+0.2}_{-0.2} \times 10^3$	$4.2^{+0.0}_{-0.0} \times 10^4$
Avg. model $\Sigma_{\text{cl, GB}} = 0.47$	#9	80^{+0}_{-0}	0.316	$0.12^{+0.00}_{-0.00}$	$16.0^{+0.0}_{-0.0}$	76.9 ± 7.6	23 ± 7	$41.6^{+0.0}_{-0.0}$	41.5 ± 0.0	$1.5^{+0.0}_{-0.0} \times 10^{-4}$	$9.4^{+0.2}_{-0.2} \times 10^3$	$4.2^{+0.0}_{-0.0} \times 10^4$
CepA	1.32	120	0.316	0.14	12.0	51.3	71	93.5	24.4	1.6×10^{-4}	2.0×10^4	3.6×10^4

Table C3 continued

Table C3 (continued)

Source	χ^2	M_c (M_\odot)	Σ_{cl} ($g\text{ cm}^{-2}$)	R_c (pc)	m_* (M_\odot)	θ_{view} ($^\circ$)	AV (mag)	M_{env} (M_\odot)	$\theta_{w,esc}$ (deg)	\dot{M}_{disk} (M_\odot/yr)	$L_{bol,iso}$ (L_\odot)	L_{bol} (L_\odot)
$d = 0.7$ kpc	1.67	160	0.316	0.17	24.0	68.0	112	97.6	37.2	2.2×10^{-4}	2.8×10^4	9.9×10^4
$R_{ap} = 36.25''$	2.01	160	0.316	0.17	32.0	88.6	119	72.0	48.1	2.2×10^{-4}	2.5×10^4	1.7×10^5
$R_{ap} = 0.12$ pc	2.17	100	1.000	0.07	24.0	54.9	107	46.2	42.8	4.4×10^{-4}	2.5×10^4	1.3×10^5
	2.19	120	0.316	0.14	16.0	61.6	69	82.2	32.1	1.8×10^{-4}	1.7×10^4	4.6×10^4
Avg. model	#102	113_{-31}^{+42}	$0.464_{-0.207}^{+0.375}$	$0.11_{-0.04}^{+0.06}$	$16.6_{-4.8}^{+6.7}$	71.0 ± 11.6	70 ± 30	$71.2_{-23.9}^{+36.0}$	32.7 ± 7.7	$2.3_{-0.4}^{+1.2} \times 10^{-4}$	$2.0_{-0.4}^{+0.4} \times 10^4$	$6.2_{-2.7}^{+4.7} \times 10^4$
Avg. model $\Sigma_{cl,GB} = 0.39$	#112	129_{-27}^{+34}	0.316	$0.15_{-0.02}^{+0.02}$	$15.1_{-3.9}^{+5.3}$	68.4 ± 14.5	79 ± 22	$91.1_{-22.9}^{+30.5}$	29.1 ± 7.4	$1.8_{-0.2}^{+0.3} \times 10^{-4}$	$2.0_{-0.4}^{+0.5} \times 10^4$	$4.9_{-1.8}^{+2.7} \times 10^4$
NGC7538	0.79	50	3.160	0.03	16.0	43.5	61	20.5	36.6	7.7×10^{-5}	4.7×10^4	1.1×10^5
$d = 2.6$ kpc	0.82	200	0.100	0.33	24.0	88.6	21	128.4	37.3	9.9×10^{-5}	2.7×10^4	8.1×10^4
$R_{ap} = 13.75''$	0.97	60	3.160	0.03	12.0	34.4	25	37.8	26.7	7.6×10^{-4}	3.3×10^4	5.0×10^4
$R_{ap} = 0.18$ pc	1.19	200	0.100	0.33	32.0	88.6	35	101.2	47.7	9.9×10^{-5}	3.0×10^4	1.5×10^5
	1.26	50	3.160	0.03	12.0	39.2	0	27.7	30.2	7.1×10^{-4}	2.2×10^4	5.1×10^4
Avg. model	#34	121_{-53}^{+95}	$0.525_{-0.399}^{+1.653}$	$0.11_{-0.07}^{+0.19}$	$25.8_{-8.6}^{+12.9}$	66.8 ± 16.4	25 ± 17	$53.0_{-27.0}^{+55.1}$	44.0 ± 8.8	$2.8_{-1.6}^{+3.8} \times 10^{-4}$	$3.0_{-0.4}^{+0.5} \times 10^4$	$1.4_{-0.6}^{+1.1} \times 10^5$
Avg. model $\Sigma_{cl,GB} = 0.56$	#47	164_{-37}^{+30}	0.316	$0.17_{-0.02}^{+0.02}$	$29.2_{-10.4}^{+16.2}$	67.2 ± 17.1	14 ± 19	$76.3_{-16.2}^{+20.5}$	45.0 ± 11.5	$2.1_{-0.2}^{+0.2} \times 10^{-4}$	$2.8_{-0.4}^{+0.5} \times 10^4$	$1.5_{-0.8}^{+1.8} \times 10^5$
SOMA II												
G45.12+0.13	19.12	240	3.160	0.06	32.0	29.0	0	175.3	23.4	1.9×10^{-3}	4.5×10^5	5.0×10^5
$d = 7.4$ kpc	19.12	480	1.000	0.16	96.0	47.5	0	237.8	43.1	1.3×10^{-3}	4.4×10^5	1.6×10^6
$R_{ap} = 47.00''$	19.52	480	1.000	0.16	48.0	29.0	1	367.0	25.4	1.1×10^{-3}	4.5×10^5	5.4×10^5
$R_{ap} = 1.69$ pc	22.43	400	1.000	0.15	64.0	39.2	4	246.4	36.1	1.1×10^{-3}	4.2×10^5	8.2×10^5
	24.75	480	1.000	0.16	64.0	39.2	0	324.6	31.7	1.2×10^{-3}	3.6×10^5	8.4×10^5
Avg. model	#15	379_{-100}^{+96}	$1.467_{-0.746}^{+1.518}$	$0.12_{-0.05}^{+0.07}$	$56.0_{-22.6}^{+38.0}$	37.4 ± 12.6	17 ± 47	$227.9_{-72.8}^{+107.0}$	33.2 ± 11.6	$1.4_{-0.6}^{+0.6} \times 10^{-3}$	$4.4_{-2.2}^{+2.2} \times 10^5$	$8.0_{-3.6}^{+4.4} \times 10^5$
Avg. model $\Sigma_{cl,GB} = 0.10$	#83	449_{-47}^{+53}	0.100	$0.49_{-0.03}^{+0.03}$	$58.5_{-15.2}^{+20.5}$	49.1 ± 21.5	56 ± 54	$244.4_{-66.3}^{+91.0}$	43.5 ± 9.8	$0.2_{-0.0}^{+0.0} \times 10^{-3}$	$4.0_{-2.7}^{+8.2} \times 10^5$	$5.1_{-2.1}^{+3.7} \times 10^5$
G309.92+0.48	2.61	480	1.000	0.16	96.0	51.3	20	237.8	43.1	1.3×10^{-3}	3.3×10^5	1.6×10^6
$d = 5.5$ kpc	2.67	240	3.160	0.06	32.0	39.2	6	175.3	23.4	1.9×10^{-3}	2.7×10^5	5.0×10^5
$R_{ap} = 17.75''$	2.95	240	3.160	0.06	24.0	29.0	1	194.5	18.2	1.6×10^{-3}	2.6×10^5	3.1×10^5
$R_{ap} = 0.47$ pc	2.97	400	1.000	0.15	64.0	43.5	3	246.4	36.1	1.1×10^{-3}	2.7×10^5	8.2×10^5
	3.16	400	1.000	0.15	48.0	34.4	11	288.7	29.1	1.0×10^{-3}	3.0×10^5	5.3×10^5
Avg. model	#19	363_{-102}^{+142}	$1.274_{-0.713}^{+1.622}$	$0.12_{-0.05}^{+0.09}$	$49.3_{-19.3}^{+31.6}$	39.4 ± 9.5	19 ± 20	$240.3_{-55.0}^{+71.3}$	30.6 ± 8.9	$1.2_{-0.4}^{+0.7} \times 10^{-3}$	$3.1_{-0.6}^{+0.6} \times 10^5$	$6.6_{-2.8}^{+4.8} \times 10^5$
Avg. model $\Sigma_{cl,GB} = 0.43$	#64	453_{-44}^{+48}	0.316	$0.28_{-0.01}^{+0.01}$	$63.4_{-15.7}^{+20.8}$	63.5 ± 14.9	4 ± 14	$259.6_{-68.6}^{+93.3}$	39.5 ± 9.0	$0.5_{-0.0}^{+0.0} \times 10^{-3}$	$1.8_{-0.3}^{+0.4} \times 10^5$	$6.5_{-2.5}^{+4.0} \times 10^5$
G35.58-0.03	1.33	480	3.160	0.09	24.0	29.0	11	440.5	11.5	2.0×10^{-3}	2.7×10^5	2.9×10^5
$d = 10.2$ kpc	1.69	400	3.160	0.08	24.0	39.2	8	361.7	12.8	1.9×10^{-3}	2.6×10^5	3.0×10^5
$R_{ap} = 16.00''$	2.55	320	3.160	0.07	24.0	51.3	3	276.8	15.2	1.8×10^{-3}	2.3×10^5	3.1×10^5
$R_{ap} = 0.79$ pc	2.76	480	1.000	0.16	48.0	47.5	7	367.0	25.4	1.1×10^{-3}	2.4×10^5	5.4×10^5
	3.13	480	1.000	0.16	64.0	54.9	24	324.6	31.7	1.2×10^{-3}	2.6×10^5	8.4×10^5
Avg. model	#90	418_{-69}^{+82}	$1.994_{-0.863}^{+1.521}$	$0.11_{-0.03}^{+0.04}$	$34.1_{-12.8}^{+20.6}$	58.8 ± 18.2	10 ± 21	$335.4_{-59.3}^{+72.1}$	20.2 ± 9.3	$1.5_{-0.3}^{+0.4} \times 10^{-3}$	$2.4_{-0.3}^{+0.3} \times 10^5$	$4.3_{-1.7}^{+2.9} \times 10^5$
Avg. model $\Sigma_{cl,GB} = 0.31$	#118	432_{-53}^{+61}	0.316	$0.27_{-0.02}^{+0.02}$	$50.6_{-14.8}^{+20.9}$	64.6 ± 16.0	26 ± 27	$278.8_{-68.4}^{+90.6}$	34.9 ± 9.1	$0.4_{-0.0}^{+0.0} \times 10^{-3}$	$1.5_{-0.4}^{+0.5} \times 10^5$	$4.4_{-2.0}^{+3.6} \times 10^5$
IRAS16562	0.83	240	0.316	0.20	48.0	58.3	86	104.2	49.7	2.9×10^{-4}	6.7×10^4	3.8×10^5
$d = 1.7$ kpc	0.89	200	0.316	0.19	32.0	47.5	67	114.7	40.5	2.6×10^{-4}	5.5×10^4	1.8×10^5
$R_{ap} = 17.50''$	0.95	200	0.316	0.19	24.0	39.2	48	139.7	31.9	2.5×10^{-4}	4.8×10^4	1.0×10^5
$R_{ap} = 0.14$ pc	1.06	100	3.160	0.04	16.0	29.0	119	68.6	23.4	1.1×10^{-3}	1.0×10^5	1.2×10^5
	1.08	120	1.000	0.08	16.0	29.0	90	88.3	25.2	4.5×10^{-4}	7.8×10^4	9.7×10^4
Avg. model	#109	145_{-49}^{+73}	$1.087_{-0.723}^{+2.158}$	$0.08_{-0.04}^{+0.09}$	$29.0_{-9.7}^{+14.6}$	62.6 ± 17.4	41 ± 35	$73.3_{-30.7}^{+52.7}$	37.9 ± 8.3	$5.9_{-3.2}^{+6.8} \times 10^{-4}$	$4.9_{-1.3}^{+1.9} \times 10^4$	$2.2_{-1.2}^{+2.5} \times 10^5$
Avg. model $\Sigma_{cl,GB} = \dots$	\dots	\dots	\dots	\dots	\dots	\dots	\dots	\dots	\dots	\dots	\dots	\dots
G305.20+0.21	0.17	320	0.100	0.42	64.0	85.7	13	102.1	59.8	1.2×10^{-4}	6.2×10^4	6.0×10^5
$d = 4.1$ kpc	0.24	60	3.160	0.03	16.0	39.2	2	31.1	32.0	8.4×10^{-4}	5.8×10^4	1.1×10^5
$R_{ap} = 11.25''$	0.47	160	3.160	0.05	64.0	64.8	22	22.9	60.8	1.3×10^{-3}	8.1×10^4	8.6×10^5
$R_{ap} = 0.22$ pc	0.54	320	0.100	0.42	32.0	64.8	14	228.4	33.5	1.3×10^{-4}	6.8×10^4	1.6×10^5
	0.55	100	3.160	0.04	32.0	47.5	48	36.9	42.4	1.2×10^{-3}	1.1×10^5	3.5×10^5

Table C3 continued

Table C3 (continued)

Source	χ^2	M_c (M_\odot)	Σ_{cl} ($g\text{ cm}^{-2}$)	R_c (pc)	m_* (M_\odot)	θ_{view} ($^\circ$)	AV (mag)	M_{env} (M_\odot)	$\theta_{w,esc}$ (deg)	\dot{M}_{disk} (M_\odot/yr)	$L_{bol,iso}$ (L_\odot)	L_{bol} (L_\odot)
Avg. model	#88	214^{+149}_{-84}	$0.281^{+0.880}_{-0.213}$	$0.20^{+0.33}_{-0.11}$	$33.1^{+16.3}_{-48.2}$	62.3 ± 15.9	13 ± 16	$111.7^{+129.6}_{-166.5}$	40.3 ± 10.5	$2.4^{+3.4}_{-1.8} \times 10^{-4}$	$6.2^{+1.7}_{-2.6} \times 10^4$	$2.1^{+2.0}_{-1.0} \times 10^5$
Avg. model $\Sigma_{cl,GB} = 0.71$	#23	229^{+108}_{-73}	1.000	$0.11^{+0.02}_{-0.02}$	$58.8^{+48.2}_{-26.5}$	62.5 ± 15.5	17 ± 23	$71.0^{+16.5}_{-13.4}$	52.6 ± 11.3	$6.9^{+1.8}_{-1.4} \times 10^{-4}$	$7.2^{+2.6}_{-1.9} \times 10^4$	$6.4^{+3.9}_{-3.9} \times 10^5$
G305.20+0.21A	0.20	320	0.316	0.23	12.0	22.3	98	293.0	12.7	2.2×10^{-4}	3.6×10^4	4.0×10^4
$d = 4.1$ kpc	0.21	320	0.316	0.23	16.0	12.8	237	283.1	16.3	2.5×10^{-4}	3.6×10^5	6.1×10^4
$R_{ap} = 10.00''$	0.22	100	3.160	0.04	12.0	47.5	58	76.7	20.2	9.4×10^{-4}	2.9×10^4	5.2×10^4
$R_{ap} = 0.20$ pc	0.22	120	3.160	0.05	12.0	29.0	120	98.5	17.8	9.6×10^{-4}	4.0×10^4	5.2×10^4
Avg. model	#1447	169^{+123}_{-71}	$0.828^{+1.391}_{-0.519}$	$0.11^{+0.11}_{-0.05}$	$24.9^{+24.4}_{-12.3}$	56.8 ± 21.7	165 ± 100	$92.1^{+91.9}_{-46.0}$	34.2 ± 15.3	$4.6^{+2.3}_{-2.3} \times 10^{-4}$	$8.1^{+25.6}_{-6.1} \times 10^4$	$1.5^{+3.3}_{-1.0} \times 10^5$
Avg. model $\Sigma_{cl,GB} = 1.44$	#469	159^{+103}_{-63}	1.000	$0.09^{+0.03}_{-0.02}$	$28.8^{+34.6}_{-15.7}$	56.7 ± 21.8	167 ± 111	$75.3^{+41.4}_{-26.7}$	38.9 ± 15.9	$5.3^{+2.0}_{-1.4} \times 10^{-4}$	$9.3^{+37.6}_{-7.4} \times 10^4$	$2.0^{+5.1}_{-1.4} \times 10^5$
G49.27-0.34	2.35	480	0.100	0.51	24.0	12.8	255	417.7	21.0	1.4×10^{-4}	4.8×10^5	8.7×10^4
$d = 5.5$ kpc	2.56	400	0.100	0.47	24.0	12.8	245	331.0	23.7	1.3×10^{-4}	4.5×10^5	8.6×10^4
$R_{ap} = 24.75''$	2.69	200	3.160	0.19	24.0	22.3	244	139.7	31.9	2.5×10^{-4}	4.7×10^5	1.0×10^5
$R_{ap} = 0.67$ pc	2.72	320	0.100	0.42	48.0	43.5	268	170.1	46.2	1.4×10^{-4}	6.2×10^5	3.5×10^5
Avg. model	2.72	240	0.316	0.20	24.0	22.3	259	183.1	28.2	2.7×10^{-4}	5.1×10^5	1.1×10^5
Avg. model	#39	320^{+200}_{-123}	$0.160^{+0.266}_{-0.117}$	$0.33^{+0.35}_{-0.17}$	$24.8^{+4.8}_{-4.0}$	39.4 ± 18.9	209 ± 40	$243.8^{+220.6}_{-115.8}$	26.8 ± 6.6	$1.8^{+1.4}_{-0.8} \times 10^{-4}$	$1.4^{+2.8}_{-0.9} \times 10^5$	$1.0^{+0.5}_{-0.3} \times 10^5$
Avg. model $\Sigma_{cl,GB} = 0.34$	#33	217^{+36}_{-31}	0.100	$0.19^{+0.02}_{-0.01}$	$18.8^{+10.2}_{-6.6}$	31.8 ± 13.1	169 ± 80	$161.6^{+50.4}_{-38.4}$	26.2 ± 10.4	$2.3^{+0.3}_{-0.3} \times 10^{-4}$	$1.2^{+3.4}_{-0.9} \times 10^5$	$0.8^{+0.7}_{-0.4} \times 10^5$
G339.88-1.26	2.63	240	0.316	0.20	48.0	61.6	149	104.2	49.7	2.9×10^{-4}	6.2×10^4	3.8×10^5
$d = 2.1$ kpc	2.81	200	0.316	0.19	12.0	79.9	20	172.7	17.3	1.9×10^{-4}	2.8×10^4	4.0×10^4
$R_{ap} = 20.25''$	2.86	200	0.316	0.19	24.0	85.7	73	139.7	31.9	2.5×10^{-4}	1.0×10^5	1.0×10^5
$R_{ap} = 0.21$ pc	2.92	200	0.316	0.19	16.0	82.8	36	162.5	22.5	2.2×10^{-4}	3.0×10^4	5.3×10^4
Avg. model	2.98	480	0.316	0.29	128.0	88.6	195	91.2	66.6	3.8×10^{-4}	1.0×10^5	2.0×10^6
Avg. model	#121	226^{+48}_{-40}	$0.316^{+0.000}_{-0.000}$	$0.20^{+0.02}_{-0.02}$	$20.9^{+17.6}_{-9.6}$	64.8 ± 16.9	71 ± 51	$156.1^{+48.4}_{-37.0}$	28.6 ± 14.0	$2.4^{+0.4}_{-0.4} \times 10^{-4}$	$3.8^{+1.6}_{-1.1} \times 10^4$	$9.1^{+16.0}_{-5.8} \times 10^4$
Avg. model $\Sigma_{cl,GB} = 0.13$	#150	220^{+25}_{-23}	0.100	$0.34^{+0.02}_{-0.02}$	$24.9^{+11.8}_{-8.0}$	57.9 ± 20.0	134 ± 46	$133.0^{+49.3}_{-35.9}$	38.3 ± 12.0	$1.0^{+0.1}_{-0.1} \times 10^{-4}$	$5.0^{+10.4}_{-3.4} \times 10^4$	$8.8^{+11.0}_{-4.9} \times 10^4$
S235	2.55	10	3.160	0.01	2.0	39.2	0	5.7	35.4	1.8×10^{-4}	1.4×10^3	2.6×10^3
$d = 1.8$ kpc	5.77	50	0.316	0.09	16.0	77.0	10	7.8	67.6	7.1×10^{-5}	1.5×10^3	3.1×10^4
$R_{ap} = 7.00''$	8.27	20	3.160	0.02	4.0	39.2	0	11.6	33.6	3.1×10^{-4}	1.6×10^3	3.3×10^3
$R_{ap} = 0.06$ pc	9.80	80	1.000	0.07	32.0	82.8	56	2.7	78.7	1.4×10^{-4}	2.1×10^3	1.6×10^5
Avg. model	12.76	60	1.000	0.06	24.0	74.0	84	4.9	70.9	1.9×10^{-4}	3.7×10^3	9.3×10^4
Avg. model	#27	38^{+30}_{-17}	$0.808^{+1.189}_{-0.481}$	$0.05^{+0.04}_{-0.02}$	$12.1^{+15.2}_{-6.7}$	68.9 ± 19.7	48 ± 51	$5.5^{+5.3}_{-2.7}$	60.5 ± 16.3	$1.3^{+1.2}_{-0.6} \times 10^{-4}$	$2.3^{+2.3}_{-1.1} \times 10^3$	$2.6^{+6.9}_{-1.9} \times 10^4$
Avg. model $\Sigma_{cl,GB} = \dots$
IRAS22198	9.07	10	3.160	0.01	4.0	61.6	69	1.6	56.1	1.9×10^{-4}	2.9×10^2	1.9×10^3
$d = 0.8$ kpc	13.57	10	1.000	0.02	2.0	43.5	51	5.3	39.2	7.5×10^{-5}	2.6×10^2	7.6×10^2
$R_{ap} = 6.25''$	14.43	10	0.316	0.04	0.5	22.3	38	8.7	18.0	1.9×10^{-5}	1.7×10^2	1.9×10^2
$R_{ap} = 0.02$ pc	14.54	10	1.000	0.02	4.0	74.0	47	1.3	59.0	7.7×10^{-5}	1.3×10^2	1.1×10^3
Avg. model	17.53	10	0.316	0.04	1.0	34.4	24	7.5	28.1	2.5×10^{-5}	1.4×10^2	2.6×10^2
Avg. model	#145	11^{+3}_{-2}	$0.705^{+0.874}_{-0.390}$	$0.03^{+0.01}_{-0.01}$	$2.2^{+2.9}_{-1.3}$	57.1 ± 22.2	141 ± 165	$3.8^{+4.2}_{-2.0}$	42.4 ± 14.4	$5.6^{+7.4}_{-3.2} \times 10^{-5}$	$3.9^{+17.8}_{-3.2} \times 10^2$	$8.0^{+20.2}_{-5.7} \times 10^2$
Avg. model $\Sigma_{cl,GB} = 0.63$	#172	15^{+7}_{-8}	1.000	$0.03^{+0.01}_{-0.01}$	$1.7^{+2.8}_{-1.1}$	58.6 ± 21.3	699 ± 392	$7.8^{+10.5}_{-4.3}$	31.1 ± 16.4	$7.9^{+3.9}_{-2.6} \times 10^{-5}$	$6.4^{+15.9}_{-4.6} \times 10^2$	$11.2^{+19.3}_{-7.1} \times 10^2$
NGC2071	2.78	10	3.160	0.01	4.0	58.3	53	1.6	56.1	1.9×10^{-4}	5.0×10^2	1.9×10^3
$d = 0.4$ kpc	9.70	10	1.000	0.02	2.0	43.5	0	5.3	39.2	7.5×10^{-5}	2.6×10^2	7.6×10^2
$R_{ap} = 11.50''$	13.50	10	1.000	0.02	4.0	64.8	0	1.3	59.0	7.7×10^{-5}	1.7×10^2	1.1×10^3
$R_{ap} = 0.02$ pc	20.21	10	0.316	0.04	0.5	22.3	0	8.7	18.0	1.9×10^{-5}	1.7×10^2	1.9×10^2
Avg. model	21.73	10	1.000	0.02	1.0	29.0	26	7.8	25.4	6.0×10^{-5}	5.6×10^2	7.7×10^2
Avg. model	#138	10^{+2}_{-1}	$0.778^{+0.926}_{-0.423}$	$0.03^{+0.01}_{-0.01}$	$1.7^{+2.2}_{-1.0}$	57.0 ± 21.9	125 ± 190	$4.2^{+4.7}_{-2.0}$	38.7 ± 15.0	$5.6^{+6.6}_{-3.8} \times 10^{-5}$	$3.6^{+9.1}_{-4.2} \times 10^2$	$6.9^{+12.0}_{-4.9} \times 10^2$
Avg. model $\Sigma_{cl,GB} = 0.88$	#182	15^{+4}_{-4}	1.000	$0.03^{+0.01}_{-0.00}$	$1.8^{+2.7}_{-1.1}$	57.7 ± 21.5	531 ± 349	$7.8^{+10.8}_{-4.4}$	30.9 ± 15.8	$8.0^{+2.6}_{-2.6} \times 10^{-5}$	$6.8^{+16.3}_{-4.8} \times 10^2$	$11.9^{+19.9}_{-7.4} \times 10^2$
CepE	2.78	10	0.316	0.04	2.0	54.9	4	5.0	43.3	3.0×10^{-5}	7.2×10^1	2.8×10^2

Table C3 continued

Table C3 (continued)

Source	χ^2	M_c (M_\odot)	Σ_{cl} ($g\text{ cm}^{-2}$)	R_c (pc)	m_* (M_\odot)	θ_{view} ($^\circ$)	AV (mag)	M_{env} (M_\odot)	$\theta_{w,esc}$ (deg)	\dot{M}_{disk} (M_\odot/yr)	$L_{bol,iso}$ (L_\odot)	L_{bol} (L_\odot)
$d = 0.7$ kpc	3.38	10	1.000	0.02	4.0	71.0	82	1.3	59.0	7.7×10^{-5}	1.4×10^2	1.1×10^3
$R_{ap} = 8.50''$	10.20	10	0.316	0.04	1.0	34.4	53	7.5	28.1	2.5×10^{-5}	1.4×10^2	2.6×10^2
$R_{ap} = 0.03$ pc	17.11	10	0.316	0.04	4.0	82.8	49	0.6	68.4	2.4×10^{-5}	3.4×10^1	6.7×10^2
	17.58	10	0.316	0.04	0.5	12.8	321	8.7	18.0	1.9×10^{-5}	1.4×10^3	1.9×10^2
Avg. model	#168	11_{-3}^{+3}	$0.547_{-0.303}^{+0.678}$	$0.03_{-0.01}^{+0.02}$	$2.4_{-1.3}^{+2.9}$	59.5 ± 20.8	287 ± 260	$3.2_{-2.0}^{+5.1}$	45.7 ± 16.4	$4.5_{-2.3}^{+4.8} \times 10^{-5}$	$3.3_{-2.5}^{+10.1} \times 10^2$	$7.4_{-4.9}^{+14.3} \times 10^2$
Avg. model $\Sigma_{cl,GB} = 0.19$	#180	15_{-4}^{+6}	$0.316_{-0.01}^{+0.01}$	$0.05_{-0.01}^{+0.01}$	$1.7_{-1.0}^{+1.0}$	57.3 ± 21.4	471 ± 364	$6.4_{-4.3}^{+12.7}$	35.3 ± 19.4	$3.1_{-0.9}^{+1.2} \times 10^{-5}$	$3.3_{-2.5}^{+10.2} \times 10^2$	$5.4_{-3.7}^{+11.8} \times 10^2$
L1206 A	1.75	40	1.000	0.05	4.0	39.2	0	31.5	23.3	1.7×10^{-4}	1.2×10^3	2.2×10^3
$d = 0.8$ kpc	1.90	30	1.000	0.04	2.0	29.0	17	25.9	18.8	1.2×10^{-4}	1.7×10^3	1.7×10^3
$R_{ap} = 6.50''$	2.17	20	1.000	0.03	8.0	58.3	239	4.0	50.7	1.5×10^{-4}	2.2×10^3	1.1×10^4
$R_{ap} = 0.02$ pc	2.18	40	1.000	0.05	2.0	22.3	67	35.8	15.6	1.3×10^{-4}	1.6×10^3	2.0×10^3
	2.35	30	1.000	0.04	4.0	43.5	4	21.6	27.7	1.5×10^{-4}	9.2×10^2	2.0×10^3
Avg. model	#23	27_{-6}^{+8}	$1.73_{-0.770}^{+1.387}$	$0.03_{-0.01}^{+0.01}$	$3.2_{-1.5}^{+2.7}$	39.5 ± 12.9	116 ± 82	$16.8_{-8.6}^{+17.4}$	27.1 ± 11.7	$2.0_{-0.6}^{+0.9} \times 10^{-4}$	$1.7_{-0.5}^{+0.7} \times 10^3$	$3.7_{-1.7}^{+3.3} \times 10^3$
Avg. model $\Sigma_{cl,GB} = \dots$
L1206 B	3.87	10	0.316	0.04	4.0	74.0	52	0.6	68.4	2.4×10^{-5}	6.8×10^1	6.7×10^2
$d = 0.8$ kpc	8.05	30	1.000	0.04	0.5	12.8	134	29.1	7.6	6.0×10^{-5}	1.0×10^3	4.2×10^2
$R_{ap} = 8.00''$	12.80	40	1.000	0.05	0.5	12.8	103	38.9	6.2	6.5×10^{-5}	4.0×10^2	4.0×10^2
$R_{ap} = 0.03$ pc	13.22	10	0.316	0.04	2.0	43.5	186	5.0	43.3	3.0×10^{-5}	3.3×10^2	2.8×10^2
	14.41	20	1.000	0.03	0.5	12.8	237	19.2	10.0	5.4×10^{-5}	1.7×10^3	4.5×10^2
Avg. model	#52	11_{-3}^{+4}	$0.403_{-0.194}^{+0.376}$	$0.04_{-0.01}^{+0.01}$	$2.2_{-1.1}^{+2.2}$	52.2 ± 25.5	130 ± 78	$2.5_{-1.8}^{+6.3}$	49.0 ± 18.9	$3.2_{-1.3}^{+2.3} \times 10^{-5}$	$2.6_{-2.0}^{+8.1} \times 10^2$	$4.5_{-1.9}^{+3.4} \times 10^2$
Avg. model $\Sigma_{cl,GB} = \dots$
IRAS22172 mir1	0.24	30	0.100	0.13	1.0	12.8	73	27.3	15.2	1.5×10^{-5}	8.7×10^2	1.7×10^2
$d = 2.4$ kpc	0.24	60	0.100	0.18	1.0	12.8	57	57.5	9.5	1.8×10^{-5}	6.1×10^2	2.0×10^2
$R_{ap} = 8.00''$	0.25	40	0.100	0.15	1.0	12.8	63	38.0	12.5	1.6×10^{-5}	6.8×10^2	1.7×10^2
$R_{ap} = 0.09$ pc	0.25	30	0.100	0.13	2.0	22.3	67	24.6	23.2	2.0×10^{-5}	8.0×10^2	2.4×10^2
	0.25	20	0.100	0.10	4.0	47.5	47	9.9	43.3	2.1×10^{-5}	3.4×10^2	6.8×10^2
Avg. model	#5038	88_{-52}^{+125}	$0.890_{-0.594}^{+1.786}$	$0.07_{-0.03}^{+0.06}$	$8.9_{-6.0}^{+18.3}$	56.5 ± 21.8	407 ± 289	$50.6_{-36.8}^{+22.1}$	28.9 ± 18.1	$2.6_{-1.1}^{+6.2} \times 10^{-4}$	$1.2_{-1.1}^{+8.1} \times 10^4$	$2.0_{-1.6}^{+16.7} \times 10^4$
Avg. model $\Sigma_{cl,GB} = \dots$
IRAS22172 mir2	1.31	30	0.100	0.13	8.0	64.8	28	8.9	56.6	2.6×10^{-5}	1.2×10^3	6.3×10^3
$d = 2.4$ kpc	1.52	20	0.316	0.06	8.0	77.0	11	1.6	65.5	4.4×10^{-5}	8.6×10^2	9.9×10^3
$R_{ap} = 26.75''$	1.72	60	0.100	0.18	4.0	22.3	37	51.2	21.1	3.4×10^{-5}	2.1×10^3	8.9×10^2
$R_{ap} = 0.31$ pc	1.74	100	0.316	0.13	32.0	85.7	27	4.5	81.4	5.0×10^{-5}	1.3×10^3	1.4×10^5
	2.20	320	0.316	0.23	96.0	85.7	138	6.5	85.4	6.6×10^{-5}	8.5×10^3	1.2×10^6
Avg. model	#28	37_{-19}^{+39}	$0.201_{-0.120}^{+0.296}$	$0.10_{-0.05}^{+0.09}$	$7.5_{-4.0}^{+8.6}$	60.9 ± 27.6	34 ± 37	$8.9_{-6.3}^{+21.7}$	50.8 ± 20.4	$4.2_{-1.8}^{+3.1} \times 10^{-5}$	$1.5_{-0.8}^{+1.9} \times 10^3$	$6.2_{-5.0}^{+26.1} \times 10^3$
Avg. model $\Sigma_{cl,GB} = \dots$
IRAS22172 mir3	0.34	60	0.100	0.18	2.0	12.8	134	55.4	14.9	2.5×10^{-5}	1.7×10^3	3.5×10^2
$d = 2.4$ kpc	0.34	50	0.100	0.16	2.0	12.8	128	45.5	16.5	2.4×10^{-5}	1.6×10^3	3.1×10^2
$R_{ap} = 7.75''$	0.36	60	0.100	0.18	16.0	82.8	110	6.5	76.4	2.0×10^{-5}	6.5×10^2	2.5×10^4
$R_{ap} = 0.09$ pc	0.37	10	3.160	0.01	4.0	54.9	161	1.6	56.1	1.9×10^{-4}	1.5×10^3	1.9×10^3
	0.37	10	1.000	0.02	4.0	61.6	31	1.3	59.0	7.7×10^{-5}	2.4×10^2	1.1×10^3
Avg. model	#605	35_{-17}^{+35}	$0.282_{-0.193}^{+0.615}$	$0.08_{-0.04}^{+0.09}$	$4.0_{-2.5}^{+6.3}$	45.5 ± 23.9	143 ± 118	$13.6_{-9.9}^{+35.8}$	38.2 ± 23.7	$4.6_{-2.7}^{+6.7} \times 10^{-5}$	$1.8_{-1.6}^{+11.5} \times 10^3$	$1.9_{-1.6}^{+10.0} \times 10^3$
Avg. model $\Sigma_{cl,GB} = \dots$
IRAS21391 bima2	0.50	10	0.316	0.04	2.0	47.5	103	5.0	43.3	3.0×10^{-5}	9.0×10^1	2.8×10^2
$d = 0.8$ kpc	0.89	10	1.000	0.02	4.0	61.6	204	1.3	59.0	7.7×10^{-5}	2.4×10^2	1.1×10^3
$R_{ap} = 7.00''$	1.35	10	0.316	0.04	4.0	79.9	93	0.6	68.4	2.4×10^{-5}	4.0×10^1	6.7×10^2
$R_{ap} = 0.03$ pc	1.46	10	0.316	0.04	0.5	12.8	117	8.7	18.0	1.9×10^{-5}	1.7×10^2	1.9×10^2
	1.50	10	1.000	0.02	2.0	39.2	286	5.3	39.2	7.5×10^{-5}	1.0×10^3	7.6×10^2
Avg. model	#35	10_{-0}^{+0}	$0.610_{-0.371}^{+0.949}$	$0.03_{-0.01}^{+0.02}$	$2.5_{-1.0}^{+1.7}$	67.7 ± 16.7	85 ± 62	$2.7_{-1.5}^{+3.5}$	48.8 ± 12.1	$4.8_{-2.7}^{+4.9} \times 10^{-5}$	$9.9_{-4.9}^{+9.8} \times 10^1$	$5.6_{-3.1}^{+7.0} \times 10^2$

Table C3 continued

Table C3 (continued)

Source	χ^2	M_c (M_\odot)	Σ_{cl} ($g\ cm^{-2}$)	R_c (pc)	m_* (M_\odot)	θ_{view} ($^\circ$)	AV (mag)	M_{env} (M_\odot)	$\theta_{w,esc}$ (deg)	\dot{M}_{disk} (M_\odot/yr)	$L_{bol,iso}$ (L_\odot)	L_{bol} (L_\odot)
Avg. model $\Sigma_{cl,GB} = \dots$
IRAS21391 bim3	0.56	10	1.000	0.02	4.0	61.6	212	1.3	59.0	7.7×10^{-5}	2.4×10^2	1.1×10^3
$d = 0.8\ kpc$	0.57	10	1.000	0.02	2.0	39.2	295	5.3	39.2	7.5×10^{-5}	1.0×10^3	7.6×10^2
$R_{ap} = 7.75''$	0.79	10	0.316	0.04	2.0	47.5	103	5.0	43.3	3.0×10^{-5}	9.0×10^1	2.8×10^2
$R_{ap} = 0.03\ pc$	0.83	10	3.160	0.01	4.0	47.5	373	1.6	56.1	1.9×10^{-4}	2.3×10^3	1.9×10^3
	1.13	10	1.000	0.02	1.0	12.8	403	7.8	25.4	6.0×10^{-5}	5.3×10^3	7.7×10^2
Avg. model	#143	12^{+8}_{-5}	$0.824^{+1.131}_{-0.477}$	$0.03^{+0.01}_{-0.01}$	$1.7^{+0.8}_{-0.9}$	47.8 ± 25.1	217 ± 189	$5.9^{+9.9}_{-3.7}$	35.3 ± 15.5	$6.3^{+37.7}_{-3.3} \times 10^{-5}$	$6.3^{+37.7}_{-3.3} \times 10^2$	$7.2^{+11.9}_{-4.5} \times 10^2$
Avg. model $\Sigma_{cl,GB} = \dots$
IRAS21391 mir48	1.73	10	0.316	0.04	4.0	79.9	77	0.6	68.4	2.4×10^{-5}	4.0×10^1	6.7×10^2
$d = 0.8\ kpc$	20.06	20	3.160	0.02	0.5	12.8	334	19.2	8.7	1.3×10^{-4}	2.8×10^3	8.6×10^2
$R_{ap} = 7.75''$	20.10	20	1.000	0.03	0.5	12.8	313	19.2	10.0	5.4×10^{-5}	1.7×10^3	4.5×10^2
$R_{ap} = 0.03\ pc$	21.10	80	3.160	0.04	1.0	12.8	286	79.0	5.5	2.6×10^{-4}	3.6×10^3	2.1×10^3
	22.00	10	0.316	0.04	2.0	43.5	235	5.0	43.3	3.0×10^{-5}	3.3×10^2	2.8×10^2
Avg. model	#60	11^{+4}_{-3}	$0.455^{+0.565}_{-0.252}$	$0.04^{+0.02}_{-0.01}$	$2.2^{+2.1}_{-1.1}$	52.6 ± 24.8	209 ± 84	$2.6^{+6.2}_{-1.8}$	48.2 ± 18.4	$3.6^{+3.6}_{-1.8} \times 10^{-5}$	$2.6^{+7.7}_{-1.9} \times 10^2$	$4.9^{+4.6}_{-2.4} \times 10^2$
Avg. model $\Sigma_{cl,GB} = \dots$
SOMA IV												
AFGL2591	1.27	480	0.316	0.29	32.0	12.8	76	405.7	22.3	3.9×10^{-4}	1.3×10^6	2.0×10^5
$d = 3.3\ kpc$	1.82	160	3.160	0.05	24.0	22.3	90	114.6	22.9	1.4×10^{-3}	1.3×10^6	3.0×10^5
$R_{ap} = 18.75''$	1.86	400	0.316	0.26	32.0	22.3	60	317.0	25.5	3.6×10^{-4}	9.1×10^5	2.0×10^5
$R_{ap} = 0.30\ pc$	1.87	400	0.316	0.26	48.0	29.0	86	272.6	34.2	4.1×10^{-4}	1.5×10^6	4.1×10^5
	2.04	240	1.000	0.11	32.0	12.8	81	169.8	29.6	7.2×10^{-4}	1.5×10^6	2.6×10^5
Avg. model	#24	329^{+139}_{-98}	$0.649^{+1.231}_{-0.425}$	$0.17^{+0.17}_{-0.08}$	$47.5^{+20.1}_{-14.1}$	27.5 ± 10.4	88 ± 26	$199.0^{+121.4}_{-75.4}$	35.3 ± 8.0	$6.5^{+6.6}_{-3.3} \times 10^{-4}$	$1.4^{+1.3}_{-0.7} \times 10^6$	$4.8^{+4.0}_{-2.2} \times 10^5$
Avg. model $\Sigma_{cl,GB} = 0.31$	#41	422^{+57}_{-50}	0.316	$0.27^{+0.02}_{-0.02}$	$55.9^{+28.3}_{-18.8}$	31.5 ± 14.4	74 ± 38	$250.1^{+68.2}_{-53.6}$	38.3 ± 9.7	$4.2^{+0.5}_{-0.5} \times 10^{-4}$	$0.9^{+1.8}_{-0.6} \times 10^6$	$5.2^{+5.4}_{-2.7} \times 10^5$
G333.92+0.11	2.89	240	3.160	0.06	24.0	22.3	84	194.5	18.2	1.6×10^{-3}	4.4×10^5	3.1×10^5
$d = 7.1\ kpc$	3.71	200	3.160	0.06	24.0	29.0	46	155.5	20.0	1.5×10^{-3}	2.6×10^5	3.1×10^5
$R_{ap} = 25.25''$	3.75	240	3.160	0.06	32.0	29.0	92	175.3	23.4	1.9×10^{-3}	4.5×10^5	5.0×10^5
$R_{ap} = 0.87\ pc$	3.75	320	1.000	0.13	32.0	29.0	17	252.3	24.3	8.2×10^{-4}	2.0×10^5	2.7×10^5
	3.94	200	3.160	0.06	32.0	34.4	58	140.1	25.5	1.7×10^{-3}	2.8×10^5	4.6×10^5
Avg. model	#22	237^{+72}_{-55}	$2.433^{+2.037}_{-1.109}$	$0.07^{+0.04}_{-0.03}$	$35.2^{+13.6}_{-9.8}$	37.6 ± 8.0	46 ± 30	$161.5^{+47.0}_{-36.4}$	27.0 ± 5.9	$1.5^{+0.7}_{-0.5} \times 10^{-3}$	$2.7^{+1.1}_{-0.8} \times 10^5$	$4.7^{+2.2}_{-1.5} \times 10^5$
Avg. model $\Sigma_{cl,GB} = 0.43$	#71	447^{+48}_{-44}	0.316	$0.28^{+0.01}_{-0.01}$	$61.1^{+18.7}_{-14.3}$	64.0 ± 15.6	12 ± 16	$265.8^{+76.5}_{-59.4}$	38.5 ± 7.9	$0.4^{+0.0}_{-0.0} \times 10^{-3}$	$1.7^{+0.4}_{-0.3} \times 10^5$	$6.2^{+3.5}_{-2.2} \times 10^5$
G30.59-0.04	1.04	480	3.160	0.09	24.0	29.0	81	440.5	11.5	2.0×10^{-3}	2.7×10^5	2.9×10^5
$d = 11.8\ kpc$	1.06	400	3.160	0.08	24.0	39.2	80	361.7	12.8	1.9×10^{-3}	2.6×10^5	3.0×10^5
$R_{ap} = 13.50''$	1.36	320	3.160	0.07	24.0	71.0	57	276.8	15.2	1.8×10^{-3}	2.1×10^5	3.1×10^5
$R_{ap} = 0.77\ pc$	1.47	480	1.000	0.16	24.0	34.4	3	433.4	14.5	8.2×10^{-4}	1.7×10^5	2.1×10^5
	1.48	480	1.000	0.16	32.0	39.2	36	414.3	18.5	9.3×10^{-4}	2.0×10^5	3.0×10^5
Avg. model	#137	432^{+66}_{-57}	$1.600^{+1.223}_{-0.693}$	$0.12^{+0.05}_{-0.03}$	$31.5^{+12.9}_{-9.2}$	61.5 ± 17.6	48 ± 33	$361.8^{+59.3}_{-50.9}$	18.6 ± 6.4	$1.3^{+0.5}_{-0.4} \times 10^{-3}$	$2.1^{+0.4}_{-0.4} \times 10^5$	$3.5^{+1.7}_{-1.1} \times 10^5$
Avg. model $\Sigma_{cl,GB} = 0.77$	#152	442^{+45}_{-41}	1.000	$0.15^{+0.01}_{-0.01}$	$41.1^{+22.7}_{-14.6}$	63.5 ± 16.9	42 ± 42	$332.4^{+70.1}_{-57.9}$	25.1 ± 8.7	$1.0^{+0.2}_{-0.2} \times 10^{-3}$	$1.9^{+0.5}_{-0.4} \times 10^5$	$4.3^{+3.9}_{-2.1} \times 10^5$
G25.40-0.14	2.52	480	3.160	0.09	24.0	22.3	0	440.5	11.5	2.0×10^{-3}	2.9×10^5	2.9×10^5
$d = 5.7\ kpc$	2.55	480	1.000	0.16	64.0	47.5	0	324.6	31.7	1.2×10^{-3}	2.8×10^5	8.4×10^5
$R_{ap} = 48.50''$	2.57	400	3.160	0.08	24.0	22.3	1	361.7	12.8	1.9×10^{-3}	3.0×10^5	3.1×10^5
$R_{ap} = 1.34\ pc$	2.75	480	1.000	0.16	48.0	34.4	7	367.0	25.4	1.1×10^{-3}	3.0×10^5	5.4×10^5
	3.28	320	3.160	0.07	24.0	29.0	0	276.8	15.2	1.8×10^{-3}	2.7×10^5	3.1×10^5
Avg. model	#48	433^{+78}_{-66}	$1.654^{+1.291}_{-0.725}$	$0.12^{+0.05}_{-0.03}$	$42.0^{+29.7}_{-17.4}$	45.4 ± 13.3	6 ± 16	$321.5^{+75.6}_{-58.2}$	24.4 ± 11.0	$1.4^{+0.4}_{-0.3} \times 10^{-3}$	$2.7^{+0.6}_{-0.3} \times 10^5$	$5.4^{+4.6}_{-2.5} \times 10^5$
Avg. model $\Sigma_{cl,GB} = 0.21$	#122	435^{+48}_{-48}	0.316	$0.27^{+0.02}_{-0.02}$	$60.2^{+16.0}_{-12.8}$	52.0 ± 23.0	36 ± 46	$251.9^{+65.7}_{-57.9}$	39.2 ± 9.2	$0.4^{+0.0}_{-0.0} \times 10^{-3}$	$3.9^{+2.8}_{-2.8} \times 10^5$	$6.0^{+2.4}_{-2.4} \times 10^5$
G32.03+0.05	0.35	400	0.100	0.47	96.0	82.8	115	45.8	76.2	8.3×10^{-5}	4.6×10^4	1.2×10^6
$d = 5.5\ kpc$	0.44	160	0.100	0.29	24.0	51.3	71	86.6	44.7	8.5×10^{-5}	2.8×10^4	7.8×10^4

Table C3 continued

Table C3 (continued)

Source	χ^2	M_c (M_\odot)	Σ_{cl} ($g\text{ cm}^{-2}$)	R_c (pc)	m_* (M_\odot)	θ_{view} ($^\circ$)	A_V (mag)	M_{env} (M_\odot)	$\theta_{w,esc}$ (deg)	\dot{M}_{disk} (M_\odot/yr)	$L_{bol,iso}$ (L_\odot)	L_{bol} (L_\odot)
$R_{ap} = 22.75''$	0.77	240	0.100	0.36	12.0	29.0	21	210.9	18.9	8.5×10^{-5}	1.7×10^4	2.0×10^4
$R_{ap} = 0.61\text{ pc}$	0.78	160	0.100	0.29	16.0	61.6	21	115.9	31.6	8.1×10^{-5}	1.5×10^4	3.3×10^4
	0.79	200	0.100	0.33	12.0	61.6	1	174.1	20.5	8.0×10^{-5}	1.3×10^4	2.0×10^4
Avg. model	#278	135^{+118}_{-63}	$0.227^{+0.521}_{-0.111}$	$0.18^{+0.26}_{-0.158}$	$17.3^{+8.7}_{-5.8}$	63.0 ± 16.5	33 ± 36	$73.1^{+134.8}_{-47.4}$	35.6 ± 14.0	$1.4^{+1.4}_{-0.7} \times 10^{-4}$	$1.8^{+1.1}_{-0.7} \times 10^4$	$5.2^{+7.0}_{-3.0} \times 10^4$
Avg. model $\Sigma_{cl,GB} = 0.36$	#57	96^{+17}_{-14}	0.316	$0.13^{+0.01}_{-0.01}$	$16.8^{+5.4}_{-4.1}$	64.5 ± 14.3	13 ± 21	$53.2^{+9.4}_{-8.0}$	39.1 ± 7.7	$1.6^{+0.2}_{-0.1} \times 10^{-4}$	$1.5^{+0.5}_{-0.3} \times 10^4$	$5.2^{+2.7}_{-1.8} \times 10^4$
C32.09+0.05N	1.55	400	0.100	0.47	48.0	39.2	298	248.4	39.3	1.6×10^{-4}	5.6×10^5	3.6×10^5
$d = 5.5\text{ kpc}$	1.59	480	0.100	0.51	32.0	12.8	303	390.9	25.8	1.6×10^{-4}	8.0×10^5	1.6×10^5
$R_{ap} = 13.50''$	1.71	400	0.100	0.47	64.0	51.3	287	186.6	49.9	1.6×10^{-4}	3.4×10^5	6.0×10^5
$R_{ap} = 0.36\text{ pc}$	1.76	480	0.316	0.29	128.0	64.8	325	91.2	66.6	3.8×10^{-4}	1.2×10^6	2.0×10^6
	1.77	320	0.316	0.23	64.0	47.5	317	138.3	50.1	3.6×10^{-4}	8.4×10^5	6.5×10^5
Avg. model	#89	390^{+92}_{-14}	$0.214^{+0.287}_{-0.123}$	$0.31^{+0.20}_{-0.12}$	$42.5^{+48.4}_{-22.6}$	46.8 ± 18.5	250 ± 97	$201.3^{+181.6}_{-95.5}$	38.2 ± 18.6	$2.5^{+2.1}_{-1.1} \times 10^{-4}$	$3.2^{+14.3}_{-2.6} \times 10^5$	$3.0^{+8.2}_{-2.2} \times 10^5$
Avg. model $\Sigma_{cl,GB} = 0.76$	#119	217^{+53}_{-90}	1.000	$0.11^{+0.03}_{-0.03}$	$46.0^{+28.5}_{-28.5}$	53.5 ± 19.2	208 ± 139	$78.3^{+8.7}_{-8.7}$	46.1 ± 17.7	$6.5^{+1.9}_{-1.9} \times 10^{-4}$	$2.3^{+2.0}_{-2.0} \times 10^5$	$4.3^{+3.4}_{-3.4} \times 10^5$
G40.62-0.14	1.10	100	0.316	0.13	24.0	64.8	93	35.5	53.9	1.5×10^{-4}	1.2×10^4	8.8×10^4
$d = 2.2\text{ kpc}$	1.15	80	0.316	0.12	16.0	51.3	89	41.6	41.5	1.5×10^{-4}	1.2×10^4	4.2×10^4
$R_{ap} = 13.50''$	1.25	100	0.316	0.13	8.0	29.0	12	83.1	19.6	1.3×10^{-4}	7.5×10^3	1.0×10^4
$R_{ap} = 0.14\text{ pc}$	1.79	80	1.000	0.07	24.0	54.9	149	25.1	52.0	3.5×10^{-4}	2.2×10^4	1.2×10^5
	1.80	100	1.000	0.07	32.0	61.6	149	23.9	58.3	3.8×10^{-4}	2.2×10^4	2.0×10^5
Avg. model	#52	71^{+27}_{-20}	$0.471^{+0.432}_{-0.223}$	$0.09^{+0.05}_{-0.03}$	$15.9^{+7.2}_{-4.5}$	65.5 ± 13.9	62 ± 38	$30.3^{+22.1}_{-12.8}$	44.0 ± 10.0	$1.8^{+0.9}_{-0.2} \times 10^{-4}$	$9.5^{+2.5}_{-1.5} \times 10^3$	$4.8^{+2.6}_{-1.6} \times 10^4$
Avg. model $\Sigma_{cl,GB} = 0.41$	#88	80^{+25}_{-19}	0.316	$0.12^{+0.02}_{-0.02}$	$12.3^{+7.5}_{-4.7}$	62.7 ± 17.3	38 ± 38	$45.1^{+22.0}_{-14.8}$	36.1 ± 13.6	$1.3^{+0.2}_{-0.2} \times 10^{-4}$	$7.7^{+2.6}_{-1.9} \times 10^3$	$2.5^{+3.8}_{-1.5} \times 10^4$
IRAS23385	0.12	30	1.000	0.04	2.0	12.8	294	25.9	18.8	1.2×10^{-4}	1.3×10^4	1.7×10^5
$d = 4.9\text{ kpc}$	0.14	30	1.000	0.04	1.0	12.8	145	28.0	12.0	8.4×10^{-5}	5.1×10^3	1.0×10^3
$R_{ap} = 5.75''$	0.17	40	1.000	0.05	4.0	22.3	297	31.5	23.3	1.7×10^{-4}	8.3×10^3	2.2×10^3
$R_{ap} = 0.14\text{ pc}$	0.20	40	1.000	0.05	1.0	12.8	95	38.5	9.8	9.1×10^{-5}	3.6×10^3	1.0×10^3
	0.21	20	3.160	0.02	4.0	12.8	347	11.6	33.6	3.1×10^{-4}	1.9×10^4	3.3×10^3
Avg. model	#1450	50^{+53}_{-26}	$0.505^{+1.033}_{-0.339}$	$0.07^{+0.10}_{-0.04}$	$4.8^{+9.4}_{-3.2}$	57.0 ± 21.7	224 ± 212	$25.5^{+51.9}_{-17.1}$	31.9 ± 20.6	$1.0^{+0.9}_{-0.5} \times 10^{-4}$	$3.2^{+14.9}_{-2.6} \times 10^3$	$5.1^{+23.8}_{-4.2} \times 10^3$
Avg. model $\Sigma_{cl,GB} = 0.28$	#558	75^{+62}_{-34}	0.316	$0.11^{+0.04}_{-0.03}$	$4.9^{+7.0}_{-2.9}$	56.7 ± 21.7	173 ± 195	$44.7^{+79.0}_{-28.5}$	27.7 ± 21.8	$0.8^{+0.2}_{-0.2} \times 10^{-4}$	$2.4^{+10.6}_{-2.0} \times 10^3$	$3.4^{+15.8}_{-2.8} \times 10^3$
HH288	1.44	10	1.000	0.02	2.0	39.2	183	5.3	39.2	7.5×10^{-5}	1.0×10^3	7.6×10^2
$d = 2.0\text{ kpc}$	1.53	20	0.316	0.06	2.0	29.0	149	15.1	27.2	4.2×10^{-5}	7.3×10^2	4.8×10^2
$R_{ap} = 7.50''$	1.74	20	0.316	0.06	0.5	12.8	86	19.2	11.3	2.3×10^{-5}	8.3×10^2	2.0×10^2
$R_{ap} = 0.07\text{ pc}$	1.80	10	3.160	0.01	4.0	64.8	69	1.6	56.1	1.9×10^{-4}	2.4×10^2	1.9×10^3
	2.10	10	0.316	0.04	0.5	22.3	14	8.7	18.0	1.9×10^{-5}	1.7×10^2	1.9×10^2
Avg. model	#78	17^{+10}_{-6}	$0.478^{+1.273}_{-0.347}$	$0.04^{+0.06}_{-0.03}$	$2.7^{+1.9}_{-1.1}$	51.0 ± 22.9	128 ± 95	$8.1^{+14.4}_{-5.2}$	37.0 ± 12.6	$5.6^{+6.8}_{-3.1} \times 10^{-5}$	$5.7^{+12.2}_{-3.9} \times 10^2$	$7.9^{+6.8}_{-3.7} \times 10^2$
Avg. model $\Sigma_{cl,GB} = 0.25$	#74	20^{+8}_{-6}	0.316	$0.06^{+0.01}_{-0.01}$	$3.0^{+4.5}_{-1.8}$	52.6 ± 24.1	150 ± 109	$7.5^{+11.6}_{-4.6}$	39.6 ± 18.4	$4.2^{+1.3}_{-1.0} \times 10^{-5}$	$7.6^{+23.2}_{-5.7} \times 10^2$	$12.9^{+48.0}_{-10.2} \times 10^2$
IRAS00420	0.33	10	3.160	0.01	4.0	51.3	160	1.6	56.1	1.9×10^{-4}	1.9×10^3	1.9×10^3
$d = 2.2\text{ kpc}$	0.33	10	3.160	0.01	0.5	12.8	170	9.1	13.9	1.1×10^{-4}	6.8×10^3	9.1×10^2
$R_{ap} = 7.00''$	0.35	10	1.000	0.02	2.0	22.3	153	5.3	39.2	7.5×10^{-5}	3.2×10^3	7.6×10^2
$R_{ap} = 0.07\text{ pc}$	0.35	20	0.316	0.06	1.0	22.3	10	17.5	17.9	3.2×10^{-5}	3.3×10^2	3.9×10^2
	0.40	30	0.100	0.13	4.0	51.3	80	20.5	32.6	2.7×10^{-5}	4.1×10^2	7.7×10^2
Avg. model	#253	25^{+20}_{-11}	$0.310^{+0.635}_{-0.209}$	$0.07^{+0.07}_{-0.03}$	$3.4^{+3.1}_{-1.6}$	47.3 ± 23.3	103 ± 79	$11.4^{+24.1}_{-7.7}$	36.8 ± 17.4	$4.8^{+4.6}_{-2.4} \times 10^{-5}$	$1.1^{+2.8}_{-0.8} \times 10^3$	$1.3^{+2.8}_{-0.9} \times 10^3$
Avg. model $\Sigma_{cl,GB} = \dots$	\dots	\dots	\dots	\dots	\dots	\dots	\dots	\dots	\dots	\dots	\dots	\dots
IRAS00259	0.01	30	0.316	0.07	12.0	39.2	169	0.8	81.5	2.2×10^{-5}	2.2×10^4	1.2×10^4
$d = 2.5\text{ kpc}$	0.02	20	0.100	0.10	1.0	19.0	49	17.3	19.9	1.3×10^{-5}	1.2×10^2	1.5×10^2
$R_{ap} = 7.00''$	0.03	40	0.100	0.15	12.0	12.8	162	2.1	81.9	9.5×10^{-6}	2.1×10^4	1.1×10^4
$R_{ap} = 0.08\text{ pc}$	0.03	20	0.100	0.10	2.0	47.5	35	14.6	30.2	1.7×10^{-5}	1.1×10^2	1.9×10^2
	0.03	20	0.100	0.10	0.5	22.3	0	18.8	12.8	9.6×10^{-6}	8.6×10^1	9.0×10^1
Avg. model	#2427	45^{+57}_{-25}	$0.517^{+1.012}_{-0.342}$	$0.07^{+0.07}_{-0.03}$	$3.3^{+6.0}_{-2.1}$	55.3 ± 22.2	230 ± 206	$25.2^{+64.8}_{-18.2}$	27.4 ± 20.3	$8.6^{+15.0}_{-5.4} \times 10^{-5}$	$1.7^{+9.5}_{-1.5} \times 10^3$	$2.5^{+12.5}_{-2.0} \times 10^3$

Table C3 continued

Table C3 (continued)

Source	χ^2	M_c	Σ_{cl}	R_c	m_*	θ_{view}	A_V	M_{env}	$\theta_{w,esc}$	\dot{M}_{disk}	$L_{bol,iso}$	L_{bol}
		(M_{\odot})	($g\text{ cm}^{-2}$)	(pc)	(M_{\odot})	($^{\circ}$)	(mag)	(M_{\odot})	(deg)	(M_{\odot}/yr)	(L_{\odot})	(L_{\odot})
Avg. model $\Sigma_{cl,GB} \equiv \dots$	\dots	\dots	\dots	\dots	\dots	\dots	\dots	\dots	\dots	\dots	\dots	\dots

NOTE—For each source, the first five rows refer to the best five models taken from the 432 physical models for the non-restricted Σ_{cl} case. The sixth row shows the average and dispersion of good model fits (see the text) for the non-restricted Σ_{cl} case. The seventh row shows the average and dispersion of good models for the restricted $\Sigma_{cl,GB}$ case. The number next to the symbol # represents the number of models considered in the average of the good models. Upper and lower scripts in the average model rows refer to the upper and lower range of the dispersion of the good models.

REFERENCES

- Beltrán, M. T., Padovani, M., Galli, D., et al. 2024, *A&A*, 686, A281, doi: [10.1051/0004-6361/202348927](https://doi.org/10.1051/0004-6361/202348927)
- Beuther, H., Schilke, P., Sridharan, T. K., et al. 2002, *A&A*, 383, 892, doi: [10.1051/0004-6361:20011808](https://doi.org/10.1051/0004-6361:20011808)
- Bonnell, I. A., Bate, M. R., & Zinnecker, H. 1998, *MNRAS*, 298, 93, doi: [10.1046/j.1365-8711.1998.01590.x](https://doi.org/10.1046/j.1365-8711.1998.01590.x)
- Bradley, L., Sipőcz, B., Robitaille, T., et al. 2020, *astropy/photutils*: 1.0.0, 1.0.0, Zenodo, doi: [10.5281/zenodo.4044744](https://doi.org/10.5281/zenodo.4044744)
- Butler, M. J., & Tan, J. C. 2009, *ApJ*, 696, 484, doi: [10.1088/0004-637X/696/1/484](https://doi.org/10.1088/0004-637X/696/1/484)
- . 2012, *ApJ*, 754, 5, doi: [10.1088/0004-637X/754/1/5](https://doi.org/10.1088/0004-637X/754/1/5)
- Campbell, M. F., Butner, H. M., Harvey, P. M., et al. 1995, *ApJ*, 454, 831, doi: [10.1086/176536](https://doi.org/10.1086/176536)
- Campbell, M. F., T. K., S., Beuther, H., et al. 2008, *The Astrophysical Journal*, 673, 954, doi: [10.1086/524768](https://doi.org/10.1086/524768)
- Crowe, S., Fedriani, R., Tan, J. C., et al. 2024, *A&A*, 682, A2, doi: [10.1051/0004-6361/202348094](https://doi.org/10.1051/0004-6361/202348094)
- Cyganowski, C. J., Brogan, C. L., Hunter, T. R., & Churchwell, E. 2009, *The Astrophysical Journal*, 702, 1615, doi: [10.1088/0004-637X/702/2/1615](https://doi.org/10.1088/0004-637X/702/2/1615)
- Cyganowski, C. J., Brogan, C. L., Hunter, T. R., et al. 2012, *The Astrophysical Journal Letters*, 760, L20, doi: [10.1088/2041-8205/760/2/L20](https://doi.org/10.1088/2041-8205/760/2/L20)
- Cyganowski, C. J., Whitney, B. A., Holden, E., et al. 2008, *The Astronomical Journal*, 136, 2391, doi: [10.1088/0004-6256/136/6/2391](https://doi.org/10.1088/0004-6256/136/6/2391)
- De Buizer, J. M., Liu, M., Tan, J. C., et al. 2017, *ApJ*, 843, 33, doi: [10.3847/1538-4357/aa74c8](https://doi.org/10.3847/1538-4357/aa74c8)
- Fazio, G. G., Hora, J. L., Allen, L. E., et al. 2004, *ApJS*, 154, 10, doi: [10.1086/422843](https://doi.org/10.1086/422843)
- Fedriani, R., Tan, J. C., Telkamp, Z., et al. 2023, *ApJ*, 942, 7, doi: [10.3847/1538-4357/aca4cf](https://doi.org/10.3847/1538-4357/aca4cf)
- Gibb, A. G., Davis, C. J., & Moore, T. 2007, *Monthly Notices of the Royal Astronomical Society*, 382, 1213
- Goedhart, S., Maswanganye, J. P., Gaylard, M. J., & van der Walt, D. J. 2014, *MNRAS*, 437, 1808, doi: [10.1093/mnras/stt2009](https://doi.org/10.1093/mnras/stt2009)
- Griffin, M. J., Abergel, A., Abreu, A., et al. 2010, *A&A*, 518, L3, doi: [10.1051/0004-6361/201014519](https://doi.org/10.1051/0004-6361/201014519)
- Grudić, M. Y., Guszejnov, D., Offner, S. S. R., et al. 2022, *MNRAS*, 512, 216, doi: [10.1093/mnras/stac526](https://doi.org/10.1093/mnras/stac526)
- Guzmán, A. E., Sanhueza, P., Contreras, Y., et al. 2015, *ApJ*, 815, 130, doi: [10.1088/0004-637X/815/2/130](https://doi.org/10.1088/0004-637X/815/2/130)
- Herter, T. L., Adams, J. D., Gull, G. E., et al. 2018, *Journal of Astronomical Instrumentation*, 7, 1840005, doi: [10.1142/S2251171718400056](https://doi.org/10.1142/S2251171718400056)
- Imai, H., Kameya, O., Sasao, T., et al. 2000, *ApJ*, 538, 751, doi: [10.1086/309165](https://doi.org/10.1086/309165)
- Kainulainen, J., & Tan, J. C. 2013, *A&A*, 549, A53, doi: [10.1051/0004-6361/201219526](https://doi.org/10.1051/0004-6361/201219526)
- Kalcheva, I. E., Hoare, M. G., Urquhart, J. S., et al. 2018, *A&A*, 615, A103, doi: [10.1051/0004-6361/201832734](https://doi.org/10.1051/0004-6361/201832734)
- Krumholz, M. R., & McKee, C. F. 2008, *Nature*, 451, 1082, doi: [10.1038/nature06620](https://doi.org/10.1038/nature06620)
- Kumar, M. S. N., Bachiller, R., & Davis, C. J. 2002, *ApJ*, 576, 313, doi: [10.1086/341739](https://doi.org/10.1086/341739)
- Law, C.-Y., Tan, J. C., Skalidis, R., et al. 2024, *ApJ*, 967, 157, doi: [10.3847/1538-4357/ad39e0](https://doi.org/10.3847/1538-4357/ad39e0)
- Lim, W., & Tan, J. C. 2014, *ApJL*, 780, L29, doi: [10.1088/2041-8205/780/2/L29](https://doi.org/10.1088/2041-8205/780/2/L29)
- Lim, W., Tan, J. C., Kainulainen, J., Ma, B., & Butler, M. J. 2016, *ApJL*, 829, L19, doi: [10.3847/2041-8205/829/1/L19](https://doi.org/10.3847/2041-8205/829/1/L19)
- Liu, M., Tan, J. C., Marvil, J., et al. 2021, *ApJ*, 921, 96, doi: [10.3847/1538-4357/ac0829](https://doi.org/10.3847/1538-4357/ac0829)
- Liu, M., Tan, J. C., De Buizer, J. M., et al. 2019, *ApJ*, 874, 16, doi: [10.3847/1538-4357/ab07b7](https://doi.org/10.3847/1538-4357/ab07b7)
- . 2020, *ApJ*, 904, 75, doi: [10.3847/1538-4357/abbebf](https://doi.org/10.3847/1538-4357/abbebf)
- McKee, C. F., & Tan, J. C. 2002, *Nature*, 416, 59, doi: [10.1038/416059a](https://doi.org/10.1038/416059a)
- . 2003, *ApJ*, 585, 850, doi: [10.1086/346149](https://doi.org/10.1086/346149)
- Mège, P., Russeil, D., Zavagno, A., et al. 2021, *A&A*, 646, A74, doi: [10.1051/0004-6361/202038956](https://doi.org/10.1051/0004-6361/202038956)
- Megeath, S. T., Townsley, L. K., Oey, M. S., & Tieftrunk, A. R. 2008, in *Handbook of Star Forming Regions*, Volume I, ed. B. Reipurth, Vol. 4, 264
- Megeath, S. T., Wilson, T. L., & Corbin, M. R. 2005, *ApJL*, 622, L141, doi: [10.1086/429720](https://doi.org/10.1086/429720)
- Menten, K. M. 1991, *ApJL*, 380, L75, doi: [10.1086/186177](https://doi.org/10.1086/186177)
- Mitchell, G. F., Hasegawa, T. I., & Schella, J. 1992, *ApJ*, 386, 604, doi: [10.1086/171042](https://doi.org/10.1086/171042)
- Molinari, S., Schisano, E., Elia, D., et al. 2016, *A&A*, 591, A149, doi: [10.1051/0004-6361/201526380](https://doi.org/10.1051/0004-6361/201526380)
- Moser, E., Liu, M., Tan, J. C., et al. 2020, *ApJ*, 897, 136, doi: [10.3847/1538-4357/ab96c1](https://doi.org/10.3847/1538-4357/ab96c1)
- Mutic, M. M., Chibueze, J. O., El Bouchefry, K., et al. 2021, *MNRAS*, 506, 4175, doi: [10.1093/mnras/stab1946](https://doi.org/10.1093/mnras/stab1946)
- Oh, C. S., Kobayashi, H., Honma, M., et al. 2010, *PASJ*, 62, 101, doi: [10.1093/pasj/62.1.101](https://doi.org/10.1093/pasj/62.1.101)
- Ossenkopf, V., & Henning, T. 1994, *A&A*, 291, 943
- Palau, A., Estalella, R., Ho, P. T. P., Beuther, H., & Beltrán, M. T. 2007, *A&A*, 474, 911, doi: [10.1051/0004-6361:20077692](https://doi.org/10.1051/0004-6361:20077692)
- Ridge, N. A., & Moore, T. J. T. 2001, *A&A*, 378, 495, doi: [10.1051/0004-6361:20011180](https://doi.org/10.1051/0004-6361:20011180)

- Robitaille, T., Rice, T., Beaumont, C., et al. 2019, *astrodendro*: Astronomical data dendrogram creator, *Astrophysics Source Code Library*, record ascl:1907.016, <http://ascl.net/1907.016>
- Rodón, J. A., Beuther, H., Megeath, S. T., & van der Tak, F. F. S. 2008, *A&A*, 490, 213, doi: [10.1051/0004-6361:200810158](https://doi.org/10.1051/0004-6361:200810158)
- Rosolowsky, E. W., Pineda, J. E., Kauffmann, J., & Goodman, A. A. 2008, *ApJ*, 679, 1338, doi: [10.1086/587685](https://doi.org/10.1086/587685)
- Simon, R., Jackson, J. M., Rathborne, J. M., & Chambers, E. T. 2006, *ApJ*, 639, 227, doi: [10.1086/499342](https://doi.org/10.1086/499342)
- Sridharan, T. K., Beuther, H., Schilke, P., Menten, K. M., & Wyrowski, F. 2002, *ApJ*, 566, 931, doi: [10.1086/338332](https://doi.org/10.1086/338332)
- Tanaka, K. E. I., Tan, J. C., & Zhang, Y. 2017, *ApJ*, 835, 32, doi: [10.3847/1538-4357/835/1/32](https://doi.org/10.3847/1538-4357/835/1/32)
- van der Tak, F. F. S., Tuthill, P. G., & Danchi, W. C. 2005, *A&A*, 431, 993, doi: [10.1051/0004-6361:20041595](https://doi.org/10.1051/0004-6361:20041595)
- Veneziani, M., Elia, D., Noriega-Crespo, A., et al. 2013, *A&A*, 549, A130, doi: [10.1051/0004-6361/201219570](https://doi.org/10.1051/0004-6361/201219570)
- Wang, K., Zhang, Q., Testi, L., et al. 2014, *MNRAS*, 439, 3275, doi: [10.1093/mnras/stu127](https://doi.org/10.1093/mnras/stu127)
- Wang, P., Li, Z.-Y., Abel, T., & Nakamura, F. 2010, *ApJ*, 709, 27, doi: [10.1088/0004-637X/709/1/27](https://doi.org/10.1088/0004-637X/709/1/27)
- Wang, K.-S., Bourke, T. L., Hogerheijde, M. R., et al. 2013, *A&A*, 558, A69, doi: [10.1051/0004-6361/201322087](https://doi.org/10.1051/0004-6361/201322087)
- Werner, M. W., Roellig, T. L., Low, F. J., et al. 2004, *ApJS*, 154, 1, doi: [10.1086/422992](https://doi.org/10.1086/422992)
- Whitney, B. A., Wood, K., Bjorkman, J. E., & Wolff, M. J. 2003, *ApJ*, 591, 1049, doi: [10.1086/375415](https://doi.org/10.1086/375415)
- Zhang, Y., & Tan, J. C. 2018, *ApJ*, 853, 18, doi: [10.3847/1538-4357/aaa24a](https://doi.org/10.3847/1538-4357/aaa24a)
- Zucker, C., Speagle, Joshua S., Schlafly, Edward F., et al. 2020, *A&A*, 633, A51, doi: [10.1051/0004-6361/201936145](https://doi.org/10.1051/0004-6361/201936145)